Technische Universität München

Max-Planck-Institut für Physik
(Werner-Heisenberg-Institut)

Automation of higher order corrections and their applications Beyond the Standard Model

Johann Felix Graf von Soden-Fraunhofen

This thesis is based on the author's work conducted at the Max Planck Institute for Physics (Werner-Heisenberg-Institut) in Munich. Parts of this work have already been published or are in preparation for publication:

Articles

[1] J. Bellm, S. Gieseke, N. Greiner, G. Heinrich, S. Platzer, C. Reuschle, J. F. von Soden-Fraunhofen. 'Anomalous coupling, top-mass and parton-shower effects in W^+W^- production'. *JHEP* 2016.5 (2016), pp. 1–29. ISSN: 1029-8479. DOI: 10.1007/JHEP05(2016)106. arXiv: 1602.05141 [hep-ph].

[2] G. Cullen, H. van Deurzen, N. Greiner, G. Heinrich, G. Luisoni, P. Mastrolia, E. Mirabella, G. Ossola, T. Peraro, J. Schlenk, J. F. von Soden-Fraunhofen, F. Tramontano. 'GoSam-2.0: a tool for automated one-loop calculations within the Standard Model and beyond'. *EPJC* 74.8, 3001 (2014). DOI: 10.1140/epjc/s10052-014-3001-5. arXiv: 1404.7096.

[3] J. P. Guillet, G. Heinrich, J. F. von Soden-Fraunhofen. 'Tools for NLO automation: extension of the golem95C integral library'. *Comput.Phys.Commun.* 185.6 (Dec. 2014), pp. 1828–1834. ISSN: 0010-4655. DOI: 10.1016/j.cpc.2014.03.009. arXiv: 1312.3887.

[4] N. Greiner, G. Heinrich, J. Reichel, J. F. von Soden-Fraunhofen. 'NLO QCD corrections to diphoton plus jet production through graviton exchange'. *JHEP* 1311 (Aug. 2013), p. 028. DOI: 10.1007/JHEP11(2013)028. arXiv: 1308.2194.

[5] H. van Deurzen, N. Greiner, G. Luisoni, P. Mastrolia, E. Mirabella, G. Ossola, T. Peraro, J. F. von Soden-Fraunhofen, F. Tramontano. 'NLO QCD corrections to the production of Higgs plus two jets at the LHC'. *Phys.Lett.* B721 (Jan. 2013), pp. 74–81. DOI: 10.1016/j.physletb.2013.02.051. arXiv: 1301.0493.

Proceedings and reports

[6] J. Bellm, S. Gieseke, N. Greiner, G. Heinrich, S. Plätzer, C. Reuschle, J. F. von Soden-Fraunhofen. 'GoSam plus Herwig++/Matchbox'. In: *Les Houches 2013: Physics at TeV Colliders Standard Model Working Group Report*. 2014. arXiv: 1405.1067.

[7] J. F. von Soden-Fraunhofen. 'GoSam 2.0: a tool for automated one-loop calculations'. *J. Phys. Conf. Ser.* 608.1 (2015), p. 012061. DOI: 10.1088/1742-6596/608/1/012061. arXiv: 1409.8526 [hep-ph].

[8] S. Alioli, S. Badger, J. Bellm, B. Biedermann, F. Boudjema, G. Cullen, A. Denner, H. van Deurzen, S. Dittmaier, R. Frederix, S. Frixione, M. V. Garzelli, S. Gieseke, E. W. N. Glover, N. Greiner, G. Heinrich, V. Hirschi, S. Hoeche, J. Huston, H. Ita, N. Kauer, F. Krauss, G. Luisoni, D. Maitre, F. Maltoni, P. Nason, C. Oleari, R. Pittau, S. Plaetzer, S. Pozzorini, L. Reina, C. Reuschle, T. Robens, J. Schlenk, M. Schoenherr, F. Siegert, J. F. von Soden-Fraunhofen, F. Tackmann, F. Tramontano, P. Uwer, G. Salam, P. Skands, S. Weinzierl, J. Winter, V. Yundin, G. Zanderighi, M. Zaro. 'Update of the Binoth Les Houches Accord for a standard interface between Monte Carlo tools and one-loop programs'. *Comput.Phys.Commun.* 185 (2014), pp. 560–571. DOI: 10.1016/j.cpc.2013.10.020. arXiv: 1308.3462 [hep-ph].

[9] G. Cullen, H. van Deurzen, N. Greiner, G. Heinrich, G. Luisoni, P. Mastrolia, E. Mirabella, G. Ossola, T. Peraro, J. Reichel, J. Schlenk, J. F. von Soden-Fraunhofen, F. Tramontano. 'GoSam applications for automated NLO calculations'. *J. Phys. Conf. Ser.* 523 (2014), p. 012056. DOI: 10.1088/1742-6596/523/1/012056. arXiv: 1309.3741 [hep-ph].

[10] G. Cullen, H. van Deurzen, N. Greiner, G. Heinrich, G. Luisoni, P. Mastrolia, E. Mirabella, G. Ossola, T. Peraro, J. Reichel, J. Schlenk, J. F. von Soden-Fraunhofen, F. Tramontano. 'NLO QCD Production of Higgs plus jets with GoSam'. *PoS* EPS-HEP2013 (2013), p. 446. arXiv: 1311.5191 [hep-ph].

[11] G. Cullen, H. van Deurzen, N. Greiner, G. Heinrich, G. Luisoni, P. Mastrolia, E. Mirabella, G. Ossola, T. Peraro, J. Reichel, J. Schlenk, J. F. von Soden-Fraunhofen, F. Tramontano. 'GoSam @ LHC: algorithms and applications to Higgs production'. *PoS* RADCOR2013 (2013), p. 029. arXiv: 1312.1761 [hep-ph].

[12] J. R. Andersen et al. 'Handbook of LHC Higgs Cross Sections: 3. Higgs Properties' (2013). Ed. by S. Heinemeyer, C. Mariotti, G. Passarino, R. Tanaka. DOI: 10.5170/CERN-2013-004. arXiv: 1307.1347 [hep-ph].

Abstract

After the discovery of the Higgs particle, which filled the last gap in the Standard Model (SM) of particle physics, and first measurements of its properties, further measurements and especially the search for Physics Beyond the Standard Model (BSM) have been intensified. Both require precise theoretical predictions at next-to-leading order in Quantum Chromodynamics (QCD) perturbation theory and beyond.

In this thesis, several developments on GoSam, a framework for the automated calculation of QCD and electroweak corrections at next-to-leading order, are presented. In particular, its updated interface to Monte Carlo event generators defined in the second version of the Binoth Les Houches Accord (BLHA2) is presented and discussed.

Furthermore, an extension of the tensor integral library Golem95C to higher ranks in the pentagon and hexagon cases is worked out.

These various developments extend the usability and applicability of GoSam, especially for BSM calculations.

The process $pp\,(\to W^+W^-) \to e^+ \nu_e\, \mu^- \bar{\nu}_\mu$ is calculated at NLO QCD with Herwig and GoSam. The analysis is focused on anomalous ggW^+W^- couplings, which stem from higher-dimensional effective field operators that modify the gluon-gluon-channel, which is loop-induced in the Standard Model. In addition, parton shower effects and dependencies on massive quarks are analyzed. The calculation is performed at LHC energies and at 100 TeV for a future proton-proton collider.

Zusammenfassung

Nach der Entdeckung des Higgs-Teilchens, mit dem die letzte Lücke im Standardmodell der Elementarteilchenphysik gefüllt werden konnte, schreitet die Messung seiner Eigenschaften voran. Auch die Suche nach möglicher Physik jenseits des Standardmodells wird verstärkt fortgesetzt. Beides erfordert präzise theoretische Vorhersagen in nächst-führender Ordnung (NLO) in der Störungstheorie der Quantenchromodynamik (QCD) und darüber hinaus.

In dieser Arbeit werden mehrere Entwicklungen am Programm-Paket GoSam dargelegt, die in dessen Version 2.0 aufgenommen worden sind. GoSam ermöglicht die automatisierte Berechnung von Ein-Schleifen-Korrekturen in starker und elektroschwacher Wechselwirkung. Insbesondere wird in dieser Arbeit eine Erweiterung der Schnittstelle von GoSam zu Monte-Carlo-Eventgeneratoren vorgestellt, die der zweiten Version des Binoth-Les-Houches-Accords (BLHA2) folgt.

Zudem wird eine Erweiterung der Golem95C-Tensorbibliothek zu höheren Tensorrängen bei Pentagon- und Hexagon-Schleifen-Integralen ausgearbeitet.

All diese Erweiterungen steigern die Benutzbarkeit und Anwendungsmöglichkeiten von GoSam, gerade auch für Physik jenseits des Standard-Modells.

Die Arbeit beinhaltet die NLO-QCD-Berechnung von $pp \ (\to W^+W^-) \to e^+\nu_e\, \mu^-\bar{\nu}_\mu$. Im Mittelpunkt stehen anormale ggW^+W^- Kopplungen, die effektiven, höher-dimensionalen Operatoren entsprechen und den Gluon-Gluon-Kanal beeinflussen, der im Standardmodell schleifen-unterdrückt ist. Darüber hinaus werden der Einfluss von Partonschauern und schweren Quarks analysiert. Der untersuchte Prozess wird sowohl bei LHC-Energien, als auch bei einer Schwerpunktsenergie von 100 TeV für ein zukünftigen Proton-Proton-Collider berechnet.

Contents

IV   Summary and Outlook 113

10 Summary and Outlook 115

Appendices 121

A Analytic reduction formulae for rank-6 pentagons 121

B Feynman rules for the effective $ggWW$ vertices 125

C Feynman diagrams 127

D Input files 133

E Further plots 135

Acronyms 135

List of Figures 141

List of Tables 145

Bibliography 147

Part I

Introduction and theoretical framework

1 Introduction

Currently, the second run of the Large Hadron Collider (LHC) [13] at CERN[1] is ongoing. Its aim is to consolidate the measurement results of the first run and to extend the search for Physics Beyond the Standard Model (BSM).

With the discovery of the Higgs boson by the LHC-experiments ATLAS [14] and CMS [15] published in Refs. [16–18], one of the main LHC goals had been achieved. Whilst some of the properties of the Higgs boson could be determined, e.g. its mass [19, 20], spin and parity [21, 22], others, like the Higgs boson self-coupling seems to be beyond the reach of the current luminosity. With the found Higgs boson, the Standard Model (SM) seems to be now completed.

The SM describes all interaction known between fundamental particles, except gravity. One part of the SM is Quantum Chromodynamics (QCD) [23–27] that describes the strong interaction between quarks and gluons. The electroweak sector of the SM is described by the model of Glashow, Weinberg and Salam (GWS) [28–30] and by the Glashow–Iliopoulos–Maiani mechanism (GIM) [31]. The Brout-Englert-Higgs mechanism [32–37] breaks the electroweak symmetry spontaneously, such that weak bosons become massive. Yukawa interactions to the Higgs boson enable also mass terms for quarks and leptons.

The SM was validated very successfully by a great number of measurements and experiments in the last decades, mainly at particle colliders. These experiments yielded the discovery of the W-bosons [38, 39], the Z-boson [40, 41] and the top quark [42, 43], which have been also predicted by the SM.

Still, there are hints that there must be BSM physics. Phenomena such as dark matter [e.g. 44–46] or the matter/anti-matter asymmetry in the universe are not explained by the SM. Few measurements are also deviating from theoretical predictions, such as the anomalous magnetic dipole moment of the muon (cf. [47, 48]).

---

[1]Conseil Européen pour la Recherche Nucléaire or European Organization for Nuclear Research – an international particle physics laboratory near Geneva, Switzerland.

Chapter 2 gives a brief overview of the Standard Model and its field content, laying the theoretical framework for further chapters. Reasons why it might need to be extended are also discussed.

Chapter 3 concerns effective (quantum-)field theories and describes possible means of calculating effects of known or unknown theories at lower scales. Contact interactions between (light) particles that are described by higher-dimensional operators emulate and simplify effects, which occur by interactions with (virtual) heavy particles in the possibly unknown full theory. Therefore, an effective field theory can be valid only up to a certain energy scale, where the effects of heavy particles of an associated full theory can be resolved.

For the BSM search, precise predictions for the measured observables within the SM are needed as well as calculations how they are modified by BSM effects, especially since no real signal for BSM physics was found yet, beside some later mentioned possible deviations or fluctuations, which still need to be confirmed by further measurements.

In Chapter 4, a short overview of the involved collider physics is given, together with a description, how precise predictions can be calculated at next-to-leading-order (NLO), which is the first order that describes many processes in sufficient accuracy and therefore allows direct comparison with measured data.

After introducing the theoretical framework, the following parts of this thesis focus on improvements to the automation of next-to-leading-order (NLO) calculations and one application.

In Chapter 5, GoSam [2, 49, 50] will be introduced, a framework for the automated calculation of one-loop amplitudes, which are needed in NLO calculations. Several developments and improvements, partially developed by the author of this thesis and published in the GoSam 2.0 release [2], are described in Chapter 5 and, especially, an improved interface for Monte Carlo event generators in Chapter 6 following the Binoth Les Houches Accord 2 (BLHA2) [8] standard.

The scattering amplitudes, which GoSam can provide at tree- and one-loop virtual level are only one ingredient in the prediction of collider experiments. The outcome of these experiments is measured in the total scattering cross section of an analyzed process, corresponding differential distributions, such as angular dependencies, and other observables (e.g. the number of jets in the final state). To determine these observables, the squared scattering amplitudes need to be integrated over the phase-space volume of momenta of final state particles (i.e. basically all allowed kinematic possibilities). This is performed by Monte Carlo event generators, which sample over the phase space by generating individual events, whose probability are determined by

the corresponding scattering amplitude. For NLO calculations, these programs provide usually also the real-radiation part. The used Monte Carlo integration techniques allows to apply cuts to the phase space, which are needed to model experimentally directly measurable observables and help to enhance signal-to-background ratios. In the case of composite particles in the initial state, such as in proton-proton collisions, all possible partonic sub-processes (channels) need to be calculated and the corresponding parton distributions need to be taken into account.

GoSam depends on reduction programs that calculate loop integrals. Examples for such integral libraries are Golem95C [3, 51, 52] and Samurai [53, 54]. In GoSam 2.0, Ninja [55, 56] is also supported.

Chapter 7 and Chapter 8 of this thesis will present further developments of the author on the integral library Golem95C, mainly its extension to higher-rank numerators for the pentagon and hexagon case. These are needed in loop-calculations with effective field theories, such as calculations with an effective gluon-gluon-Higgs vertex (cf. Section 3.3.2). These are applied, for example, in [5]. Higher-rank numerators also occur in calculations with spin-2 particles (gravitons/Kaluza-Klein-modes), such as NLO corrections to diphoton plus jet production through graviton exchange [4] in the ADD model [57].

In Chapter 9, the previously discussed tools are employed in a calculation of W^+W^- production including leptonic decays at NLO with anomalous couplings for the LHC.

This process is especially interesting in Higgs physics, as it is a background to the $H \to WW$ decay, as well as in BSM search due to the missing energy, which results from the neutrinos in the final state.

The main focus of the calculation is on anomalous couplings that modify the gluon-gluon channel, which is loop-induced in the SM. The anomalous couplings analyzed stem from dimension-eight operators and mediate directly between two gluons and two W-bosons at tree-level.

Previous calculations of higher-order corrections to diboson production were mostly focused on the SM [e.g. 58–81]. Effective dimension-six operators, which are not included here, have been studied in vector-boson-fusion calculations and are highly restricted by measurements [82–88]. Section 9.1.2 of this thesis will give a closer overview of the existing calculations.

The calculation includes a discussion of top-mass and parton-shower effects. Thereby, several differential observables are examined. Subsequently, the calculation is extended for a future hadron collider with center-of-mass energy of 100 TeV.

Finally, Chapter 10 summarizes the collected results and developments and provides an outlook to the future.

2 The Standard Model and its challenges

The Standard Model (SM) is described by a renormalizable relativistic quantum field theory which is a gauge theory, invariant under local $\mathsf{SU}_C(3) \times \mathsf{SU}_L(2) \times \mathsf{U}_Y(1)$ transformations.

Globally, the Standard Model is symmetric under proper Poincaré transformations such as translations, rotations and Lorentz boosts in the Minkowski space and has further accidental $\mathsf{U}(1)$ symmetries conserving baryon family numbers.[1] Because of the Poincaré invariance, each irreducible representation, i.e. particle type, can be described by an arbitrary mass m and the spin s. For $m = 0$, there exists two eigenstates. For massive ones, there are $(2s + 1)$ eigenstates in the irreducible representation.

The SM is commonly described in the Lagrangian formalism, where the action of the theory can be calculated by integrating over a Langrangian $\mathcal{L}_{\mathrm{SM}}$ which contains all physical information about the theory, i.e. all fields, their masses, kinematic and interactions. It can be split up into different terms:

$$\mathcal{L}_{\mathrm{SM}} = \mathcal{L}_{\mathrm{gauge}} + \mathcal{L}_{\mathrm{fermion}} + \mathcal{L}_{\mathrm{Higgs}} + \mathcal{L}_{\mathrm{Yukawa}} + \mathcal{L}_{\mathrm{gauge\ fix.}} + \mathcal{L}_{\mathrm{ghost}} \tag{2.1}$$

The gauge term is described by the Yang-Mills theories of the strong and electroweak interaction, whose properties are described in the following sections.

To keep local gauge invariance, for each gauge group a corresponding gauge field needs to be introduced:

$$\mathcal{L}_{\mathrm{gauge}} = -\frac{1}{4} G^a_{\mu\nu} G_a^{\mu\nu} - \frac{1}{4} W^i_{\mu\nu} W_i^{\mu\nu} - \frac{1}{4} B_{\mu\nu} B^{\mu\nu} \tag{2.2}$$

where $G^a_{\mu\nu}$, $W^i_{\mu\nu}$ and $B_{\mu\nu}$ are the field strength tensors belonging to the gauge fields

---

[1] The leptonic family numbers are slightly violated due to neutrino masses, which are not included in the SM by default.

G_μ^a of $\mathsf{SU}_C(3)$, W_μ^i of $\mathsf{SU}(2)_L$, and B_μ of $\mathsf{U}(1)_Y$:

$$G_{\mu\nu}^a = \partial_\mu G_\nu^a - \partial_\nu G_\mu^a - g_s f^{abc} G_\mu^b G_\nu^c \tag{2.3}$$

$$W_{\mu\nu}^i = \partial_\mu W_\nu^i - \partial_\nu W_\mu^i - g_w \epsilon^{ijk} W_\mu^j W_\nu^k \tag{2.4}$$

$$B_{\mu\nu} = \partial_\mu B_\nu - \partial_\nu B_\mu \tag{2.5}$$

with i, j, k = 1, 2, 3 and a, b, c = 1, ..., 8, the strong coupling g_s, the electroweak coupling g_w, and the structure constants f^{abc} of $\mathsf{SU}_C(3)$ and ϵ^{ijk} of $\mathsf{SU}(2)_L$.

The fermion term $\mathcal{L}_{\text{fermion}}$ contains the interaction between the fermion fields and gauge bosons.

$$\mathcal{L}_{\text{fermion}} = \sum_{f=1}^3 \left(\bar{\Psi}_L^{Q(f)} i \not{D} \Psi_L^{Q(f)} + \bar{\Psi}_L^{l(f)} i \not{D} \Psi_L^{l(f)} + \bar{\psi}_R^{u(f)} i \not{D} \psi_R^{u(f)} \right.$$
$$\left. + \bar{\psi}_R^{d(f)} i \not{D} \psi_R^{d(f)} + \bar{\psi}_R^{e(f)} i \not{D} \psi_R^{e(f)} \right) \tag{2.6}$$

with $\not{D} = \gamma^\mu D_\mu$, D_μ the covariant derivative, γ^μ the gamma matrices. The fermion and scalar content of the SM are summarized in Table 2.1 with the corresponding quantum numbers and charges.

The covariant derivative D_μ is defined as

$$D_\mu = \partial_\mu - \mathrm{i} g_s \mathsf{T}^a G_\mu^a - \mathrm{i} g_w \mathsf{I}_\mathsf{w}^i W_\mu^i - \mathrm{i} g_1 q_Y B_\mu \tag{2.7}$$

with the generators T^a and I_w^i of $\mathsf{SU}_C(3)$ and $\mathsf{SU}_L(2)$, respectively. q_Y denotes the hypercharge of the field to which the covariant derivative is applied. g_1 is the $\mathsf{U}_Y(1)$ coupling constant. In Table 2.1, the hypercharge is the index in the 'representation' column.

The fermions occur under $SU(2)_L$ as left-handed doublets Ψ_L and right-handed singlets ψ_R. The left-handed doublets are in the fundamental representation of $\mathsf{SU}(2)_L$ and the corresponding generator $\mathsf{I}_\mathsf{w}^i = \frac{\sigma^i}{2}$, where σ^i are the Pauli matrices. For the right-handed singlets, which carry no weak iso-spin, $\mathsf{I}_\mathsf{w}^i = 0$.

The electric charge Q, the third component of the weak iso-spin I_3 and the weak hypercharge q_Y are connected with $Q = I_3 + q_Y$.[2]

The scalar Higgs boson field is described in Section 2.2, p. 22.

---

[2]The weak hypercharge can also be defined as $Y := 2q_Y$ and, accordingly, $Q = I_3 + \frac{1}{2}Y$. See Ref. [89] for a list of different notations and signs.

fields	$f = 1$	$f = 2$	$f = 3$	representation	Q
$\Psi_L^{l(f)}$	$\begin{pmatrix} \nu_e \\ e \end{pmatrix}_L$	$\begin{pmatrix} \nu_\mu \\ \mu \end{pmatrix}_L$	$\begin{pmatrix} \nu_\tau \\ \tau \end{pmatrix}_L$	$(\mathbf{1}, \mathbf{2})_{-1/2}$	0 -1
$\psi_R^{e(f)}$	e_R	μ_R	τ_R	$(\mathbf{1}, \mathbf{1})_{-1}$	-1
$\Psi_L^{Q(f)}$	$\begin{pmatrix} u \\ d' \end{pmatrix}_L$	$\begin{pmatrix} c \\ s' \end{pmatrix}_L$	$\begin{pmatrix} t \\ b' \end{pmatrix}_L$	$(\mathbf{3}, \mathbf{2})_{1/6}$	$\frac{2}{3}$ $-\frac{1}{3}$
$\psi_R^{u(f)}$	u_R	c_R	t_R	$(\mathbf{3}, \mathbf{1})_{2/3}$	$+\frac{2}{3}$
$\psi_R^{d(f)}$	d_R	s_R	b_R	$(\mathbf{3}, \mathbf{1})_{-1/3}$	$-\frac{1}{3}$
$\Phi = \begin{pmatrix} \phi^+ \\ \phi^0 \end{pmatrix}$				$(\mathbf{1}, \mathbf{2})_{1/2}$	1 0

Table 2.1: Fermion and Higgs field content of the SM. The quark and lepton exists in three generations ($f = 1, 2, 3$) where the right-handed part is a singlet under $\mathsf{SU}_L(2)$ and the left-handed particles doublets under $\mathsf{SU}_L(2)$. The quantum numbers under $\mathsf{SU}_C(3)$ and $\mathsf{SU}_L(2)$ are listed in the representation column, the weak hypercharges q_Y of $\mathsf{U}_Y(1)$ as indices.

2.1 Quantum Chromodynamics

Quantum Chromodynamics (QCD) is the theory which describes the strong interaction between quarks and gluons, i.e. particles which transform non-trivially under the $\mathsf{SU}_C(3)$ colour group.

The eight gluon fields G_μ^a are in the adjoint representation, whereas the fermion fields transform as triplets in the fundamental representation.

The strong interaction is characterized by the strong coupling constant g_s, the structure constants f^{abc} of $\mathsf{SU}_C(3)$ and the generators T^a of the fundamental representation (cf. Eq. (2.3), p. 20). The latter are connected with the identity

$$[\mathsf{T}^a, \mathsf{T}^b] = \mathrm{i}f^{abc}\mathsf{T}^c. \tag{2.8}$$

In contrast to the later discussed Quantum Electrodynamics (QED), QCD is a non-abelian gauge theory where both the fermions and the gauge bosons (gluons) carry the corresponding charge, which is called *colour*. Therefore, the gauge bosons interact with each other and the renormalized coupling constant has an inverted behaviour,

i.e. it becomes low at small distances (corresponding to high energies) and high at high distances (or low energies).

This leads to two effects: *asymptotic freedom* [26, 27] and *confinement.*

Asymptotic freedom allows perturbative calculations to be made for high energies as the interaction becomes weak. Quark and gluons can be considered like free particles. For low energies, on the other hand, the interaction becomes strong and bound, colourless states, hadrons, are formed. They can be divided further into mesons (consisting of one quark and one anti-quark) and baryons, which have three valence quarks. Typical representatives of baryons are protons and neutrons, which form the nucleon of atoms and are therefore also called nucleons. Whereas only bound states of nucleons were known with at least one proton, there are now also first hints for a tetra-neutron state [90]. Recently, also the long predicted existence of pentaquarks (five quark states) has been experimentally proven at the LHCb, where an exotic pentaquark charmonium state was observed [91]. The fact that quarks and gluons can be observed only in bound states, is called confinement.

2.2 Electroweak sector and Higgs sector

The electromagnetic force described in Quantum Electrodynamics (QED) can be unified with the weak-force to the electroweak interaction accomplished under the $\mathsf{SU}_L(2) \times \mathsf{U}_Y(1)$ gauge group in the SM which is broken spontaneously by the Brout-Englert-Higgs mechanism which allows the underlying electroweak boson fields to gain mass. The corresponding massless gauge fields are called W^1, W^2, W^3 for the $\mathsf{SU}_L(2)$ and B^0 for the $\mathsf{U}_Y(1)$. They are broken spontaneously to $\mathsf{U}(1)_{\mathrm{em}}$ so that three massive bosons W^+, W^-, Z^0 and the massless photon γ emerge.

The Brout-Englert-Higgs mechanism introduces a new complex scalar doublet $\Phi = \begin{pmatrix} \phi^+ & \phi^0 \end{pmatrix}^{\mathsf{T}}$ of $\mathsf{SU}_L(2)$ into the Lagrangian

$$\mathcal{L}_{\mathrm{Higgs}} = \left(D_\mu \Phi\right)^\dagger \left(D^\mu \Phi\right) - V(\Phi) \tag{2.9}$$

with the covariant derivative

$$D_\mu \Phi = \left(\partial_\mu - i\, g_w W_\mu^i \frac{\sigma^i}{2} - \frac{\mathrm{i}}{2} g_1 B_\mu\right)\Phi \tag{2.10}$$

and the Higgs potential $V(\Phi)$

$$V(\Phi) = -\mu^2(\Phi^\dagger \Phi) + \lambda(\Phi^\dagger \Phi)^2 \tag{2.11}$$

containing a mass term with opposite sign and a quartic term.

A corresponding, uncharged vacuum expectation value (VEV) can be chosen as

$$\langle 0| \, \Phi \, |0 \rangle = \frac{1}{\sqrt{2}} \begin{pmatrix} 0 \\ v \end{pmatrix} \tag{2.12}$$

where $v = \sqrt{\frac{\mu^2}{\lambda}}$, such that the VEV is at the minimum of the Higgs potential. This breaks the gauge symmetry spontaneously. A positive VEV requires that $\mu^2 \geq 0$. Now, the Higgs field Φ can be developed around its VEV:

$$\Phi = \begin{pmatrix} \phi^+ \\ \left(v + h(x) + i\chi^0\right)/\sqrt{2} \end{pmatrix}, \tag{2.13}$$

which introduces the real Higgs field $h(x)$ and two unphysical Goldstone fields ϕ^+ and χ^0. These Goldstone fields can be chosen as zero in the unitary gauge.

Reinserting this into the kinetic term of $\mathcal{L}_{\text{Higgs}}$, yields the following gauge boson mass terms:

$$\mathcal{L}_{\text{gauge masses}} = \frac{v^2}{8} \left(g_w^2 (W^1)^2 + g_w^2 (W^2)^2 + (g_w W^3 - g_1 B)^2 \right). \tag{2.14}$$

These terms can be diagonalized into mass eigenstates of four fields $W^\pm$, Z^0 and A:

$$W_\mu^\pm = \frac{1}{\sqrt{2}} (W_\mu^1 \mp iW_\mu^2) \tag{2.15}$$

$$Z_\mu^0 = \frac{1}{\sqrt{g_1^2 + g_w^2}} (g_w W_\mu^3 - g_1 B_\mu) \tag{2.16}$$

$$A_\mu = \frac{1}{\sqrt{g_1^2 + g_w^2}} (g_1 W_\mu^3 + g_w B_\mu) \tag{2.17}$$

with masses

$$m_{W^\pm} = \frac{g_w v}{2} \tag{2.18}$$

$$m_{Z^0} = \sqrt{g_1^2 + g_w^2}\,\frac{v}{2}. \tag{2.19}$$

The field A turns out to be massless and can therefore be identified by the electromagnetic field from QED.

The diagonalization can be parametrized by the electroweak mixing angle θ_W:

$$\begin{pmatrix} Z_\mu \\ A_\mu \end{pmatrix} = \begin{pmatrix} \cos\theta_W & -\sin\theta_W \\ \sin\theta_W & \cos\theta_W \end{pmatrix} \begin{pmatrix} W_\mu^3 \\ B_\mu \end{pmatrix}. \tag{2.20}$$

Additionally, the electroweak mixing angle θ_W relates the masses of the massive gauge bosons,

$$\frac{m_W}{m_Z} = \frac{g_w}{\sqrt{g_1^2 + g_w^2}} = \cos\theta_W, \tag{2.21}$$

and the elementary charge e to the electroweak coupling constants g_w and g_1:

$$e = g_w \sin\theta_W = g_1 \cos\theta_W. \tag{2.22}$$

The particle described by the Higgs field $h(x)$ itself has the mass $m_h = \sqrt{2\mu^2} = \sqrt{2\lambda}v$.

The Higgs particle was discovered in 2012 [16, 17]. Its mass is currently measured as $m_h = 125.09^{\pm 0.21_{\text{stat.}}}_{\pm 0.11_{\text{sys.}}}$ GeV [92].

2.2.1 Yukawa couplings

Mass terms for fermions, i.e. quarks and leptons, of the form $-m\bar{\Psi}_f\Psi_f$ would break the $\mathsf{SU}(2)_L$ gauge invariance. This can be avoided by using Yukawa-interactions to the Higgs field.

The corresponding Lagrangian is

$$\mathcal{L}_{\text{Yukawa}} = -\sum_{f,g=1}^{3} \bar{\Psi}_L^{l(f)}(Y_e)_{fg}\psi_R^{e(g)}\Phi + \Psi_L^{Q(f)}(Y_u)_{fg}\text{i}\sigma^2\Phi^*\psi_R^{u(g)}$$
$$+ \bar{\Psi}_L^{Q(f)}(Y_d)_{fg}\psi_R^{d(g)}\Phi + \text{h.c.} \quad (2.23)$$

with three 3×3 matrices Y_e, Y_u, Y_d and $\text{i}\sigma^2\Phi^*$ the charge-conjugated Higgs doublet Φ.

To switch from fermionic weak-interaction states to quark mass eigenstates, the Y_u and Y_d matrices can be diagonalized via field transformations:

$$(U_L^{(u)})^\dagger Y_u U_R^{(u)} = \text{diag}(y_u, y_c, y_t) \quad (2.24)$$
$$(U_L^{(d)})^\dagger Y_d U_R^{(d)} = \text{diag}(y_d, y_s, y_b)$$

For quarks, this transformation is described by the Cabibbo-Kobayashi-Maskawa (CKM) matrix $V_{CKM} = (U_L^{(u)})^\dagger U_L^{(d)}$ [93]. Conventionally, the left-handed down-quark sector is rotated,

$$\Psi_L^{Q(f),D} \rightarrow V_{CKM}\Psi_L^{Q(f),D} = \begin{pmatrix} V_{\text{ud}} & V_{\text{us}} & V_{\text{ub}} \\ V_{\text{cd}} & V_{\text{cs}} & V_{\text{cb}} \\ V_{\text{td}} & V_{\text{ts}} & V_{\text{tb}} \end{pmatrix}\begin{pmatrix} d'_L \\ s'_L \\ b'_L \end{pmatrix}. \quad (2.25)$$

Inserting the VEV from Eq. (2.12), p. 23 into Eq. (2.23) and applying field transformations, yields the usual mass terms for the fermions due to the Yukawa coupling to the Higgs field.

2.2.2 Gauge fixing and ghosts

The Lagrangian described in the previous sections is gauge-invariant and has therefore physical equivalent field configurations. These additional degrees of freedoms (d.o.f.) are obstructive in the path-integral formalism. To get well-defined propagators, it is necessary to remove this degeneracy, which can be done by adding gauge fixing terms. A possible set of gauge fixing terms can be set by the R_ξ gauges:

$$\mathcal{L}_{\text{gauge fix}} = -\frac{1}{2\xi}(F_G^2) - \frac{1}{2\xi}(F_A^2) - \frac{1}{2\xi}(F_Z^2) - \frac{1}{\xi}(F_+ F_-), \tag{2.26}$$

where $\xi \in \mathbb{R}$ is an arbitrary gauge parameter [3] and

$$
\begin{aligned}
F_G &= \partial^\mu G_\mu^a, & F_A &= \partial^\mu A_\mu, & F_Z &= \partial^\mu Z_\mu - \xi M_Z \chi^0 \\
F_+ &= \partial^\mu W_\mu^+ - \mathrm{i}\xi M_W \phi^+, & F_- &= \partial^\mu W_\mu^- + \mathrm{i}\xi M_W \phi^-.
\end{aligned}
\tag{2.27}
$$

Common choices for ξ are the Feynman-'t Hooft gauge choice $\xi = 1$, the unitary choice $\xi \to \infty$ and the Landau gauge $\xi \to 0$.

Using the R_ξ gauges, time-like and longitudinal polarization states, which are unphysical, appear in loop calculations with gauge fields that can be compensated by introducing anti-commuting ghost fields.

For the case of QCD corrections, which is relevant in this thesis, this yields with the anti-commuting c, $\bar{c}$ ghost fields:

$$\mathcal{L}_{\text{ghost,QCD}} = (\partial_\mu \bar{c}^a)(\partial^\mu c_a) + g_s f_{bd}^a G_a^\mu (\partial_\mu \bar{c}_b) c^d. \tag{2.28}$$

2.3 Hierarchy problem

Gauge and chiral symmetries protect the masses of gauge bosons and fermions from large loop-contributions. Their masses are therefore naturally small in comparison to the Planck scale or other high BSM scales.

In contrast, the renormalized mass of the only scalar particle in the SM, the Higgs boson, is not protected against quadratically divergent loop corrections. Its mass could therefore be expected to be at the scale of new physics. Keeping its value stable and near the measured 125 GeV is called the *hierarchy problem*.

One way to solve this, is to assume fine-tuning, which seems to be not very natural: Large loop-contributions need cancel each other 'accidentally' up to the small Higgs boson mass.

In a more natural way, this cancellation can also be achieved by assuming new particles that cancel the contributions of the particles from the SM. One method is to

---

[3]The gauge parameters could also be chosen independently for each term.

introduce new symmetries, for example extending the Poincaré-group by Supersymmetry (SUSY), which propose a super-partner for each particle. The spin of which differs by a half-integer and therefore it cancels (fully or partially, if the symmetry is broken) the loop-contributions of its partner.

2.4 Other challenges

Whilst the SM is very successful in describing the measurements in particle physics, there are at least some areas where it is obvious that BSM physics or at least a slight extension of the SM are necessary. This section lists some further experimental measurements and theoretical shortcomings which, hopefully, can be resolved in the future.

The SM includes only left-handed neutrinos, therefore neutrinos are massless in the SM. The measured neutrino oscillations [94–97] showed, however, that they must be regarded as massive, whereas their masses are orders of magnitude smaller than the other scales and masses in the SM, so that the SM must be extended to explain this.

There are multiple means of introducing right-handed neutrinos. Usually they are considered as sterile (i.e. do not interact with the fundamental interactions of the SM, but only via gravity) and/or very heavy, such that the Seesaw mechanism could naturally explain why the (left-handed) neutrinos are so light. In this case, the neutrinos would have Majorana characteristics (i.e. they are their own anti-particles).

There are some experimental results which are inconsistent with the theoretical predictions from the SM, such as the muon's anomalous magnetic dipole moment $(g-2)_\mu$ with three to four standard deviations (cf. [47, 48]). Top- and bottom-quark forward-backward asymmetries have been mostly resolved in the last years by more precise calculations and analyses (cf. [98, 99]).

From the LHC, some results such as the recent local excess in the diphoton final states at an invariant mass of $750\,\text{GeV}$ [100, 101] have given rise to speculations with respect to whether they are a hint for BSM or just a statistical fluctuation.

From a cosmological point of view, the SM is also not satisfactory. For example, a dark matter [e.g. 44–46] candidate is missing, furthermore the matter/anti-matter asymmetry in the universe is not explained. Due to the Sakharov criteria [102], CP-violation[4] needs to be present to have different reaction rates that create the matter/anti-matter

---

[4]CP-symmetry is a symmetry on combined charge conjugation (C) and parity (P) flip.

asymmetry. However, the CP-violation in the electroweak sector of the SM is too small. For the QCD sector, experiments indicate no CP-violation, so that possible CP-violating terms, which are not forbidden as such, need to be (very) small. This is known as strong CP-problem.[5]

It would also be appealing to unify the three gauge interactions, i.e. the strong, weak and electromagnetic interaction, which are described in the SM, in a Grand Unified Theory (GUT) using one larger gauge symmetry at very high energies (about 1×10^{16} GeV).

The gravitational force is not included in the SM. How it might be included correctly, is not yet clear.

The SM has several parameters, the values of which are not predicted by the theory itself, which are unrelated to each other and can therefore only be obtained from experiments. One example are the fermion masses, which cover a wide range ($m_t > 10^5 m_{e^-}$). This is seen as non-satisfactory.

---

[5]A small CP-violation in the QCD sector can be enforced by introducing a global $\mathsf{U}(1)$ symmetry (Peccei–Quinn symmetry) [103, 104] and, accordingly, new particles called axions. See [105] and references therein.

3 Effective field theories

3.1 Introduction

This short introduction to effective field theories (EFTs) is based on [106, 107].

An EFT allows a systematic description of physics at lower scales compared with known or unknown physics at higher scales. It allows concentration on the relevant fields and symmetries or, in general, on degrees of freedom at or below a specific scale, whereas effects of physics at higher energy scales can be decoupled. All possible interactions between the fields in form of an infinite set of local operators need to be included, but due to power counting, which can be seen as one of the ordering principle of EFTs and is described in Section 3.2, only a finite number of interactions have to be considered.

If the physics at the high energy scale is known and perturbative, an EFT can be constructed by eliminating heavy states. In the path integral formulation, these heavier states are essentially 'integrated out'. This procedure results in an effective action, which contain an infinite series of effective local, higher-dimensional operators and corresponding coefficients, called Wilson coefficients. To adapt the Wilson coefficient of the EFT to the full theory, a *matching* procedure needs to be carried out. Again, power counting can be used to isolate operators that are relevant at lower energy scales.

Due to the different energy scales involved, the full theory is sometimes called the ultraviolet (UV) theory, the effective theory the infrared (IR) theory.

Examples for kinds of theories for which the full theory is known, are the four-fermion theory discussed later, the soft-collinear effective theory (SCET) [108, 109], which is useful for high order resummation of Sudakov logarithms, theories such as non-relativistic Quantum Chromodynamics (NRQCD), which is used to describe non-relativistic quark-antiquark pairs (heavy quarkonia), and Heavy Quark Effective Theory (HQET) that is helpful in calculations with B-mesons.

There are also theories such as the Chiral Pertubation Theory (χPT) where the full theory (QCD) is known, but the Wilson coefficients cannot be calculated, at least not in a perturbative manner.

Employing EFT is convenient as it simplifies calculations and can be used to reduce the order of loop calculations, as in the case of the effective gluon-Higgs coupling where interactions mediated by top-quark loops are replaced by local interactions. Instead of a full two-loop calculation, the effect can be approximated by an effective coupling at one loop.

Furthermore, approximate symmetries (spin or chiral) are often manifest in EFTs and simplify calculations further.

In the case of unknown physics at higher scales such as in the case of BSM, EFT can be used for a general study of possible effects of various (still unknown) BSM scenarios.

Comparing precision measurements with EFT calculations, general limits can be retrieved on the coefficients of effective operators, which limits various BSM models.

The introduction of effective operators allows the relative importance of unknown interactions to be parametrized and predicted in a general, model-independent manner.

3.1.1 The Standard Model as an effective theory

At very high scales, like the Planck scale, the SM becomes inadequate and quantum gravity effects cannot be longer ignored. Therefore all theories at lower scales, including the SM, could be interpreted as effective theories. However, for better distinction, fully renormalizable theories, i.e. theories with a finite number of counter-terms and therefore only terms with dimension ≤ 4 such as the SM, are not regarded as EFT here.

3.2 Power counting

Power counting is the order principle of EFTs. It allows the operators to be arranged so as to distinguish more important from less important and therefore often negligible operators.

In weakly coupled EFTs, power-counting is identical to a dimensional analysis of each operator related to the canonical dimensions of the involved fields. Higher-dimensional operators need to be suppressed by powers of the cut-off scale Λ. One gets an expansion in ratios of energy scales.

In the case of fully or partially strongly coupled EFTs, such as χPT, which are non-renormalizable at leading order, naive dimensional analysis is not sufficient for power counting in all cases and information based on a study of the loop-structure needs to be added (see e.g. [110] for details).

3.3 Examples

3.3.1 Four-fermion interaction

A simple example of an effective field theory is the Fermi model, which contains a four-fermion interaction. Its Lagrangian can be written including the correct tensor structure (V-A) as:

$$\mathcal{L}_{\text{Fermi}} = -\frac{G_F}{\sqrt{2}} \left(\bar{u} \gamma^\mu (1 - \gamma^5) d \right) \left(\bar{\nu}_e \gamma_\mu (1 - \gamma^5) e \right) \tag{3.1}$$

with $\gamma^5 = \mathrm{i} \gamma^0 \gamma^1 \gamma^2 \gamma^3$ and $G_F = \frac{\sqrt{2}}{8} \frac{g_w^2}{m_W^2} = \frac{1}{\sqrt{2} v^2}$.

Historically, Fermi developed it to describe the β-decay [111]. He used neutrons and protons instead of their constituent quarks. Later the theory was found to be limited to low energies.

From a modern perspective, this is expected, since the exchange of $W^\pm$ or Z bosons is approximated by an effective four-point interaction with factor $\mathrm{i} \frac{G_F}{\sqrt{2}}$ in the Fermi model.

Going to higher energies, higher-dimensional operators, which are neglected in Eq. (3.1), since they are suppressed by additional powers of G_F, cannot be longer ignored. At an energy scale of $G_F^{-\frac{1}{2}} \approx 300\,\text{GeV}$, all of these (infinite number of) terms become important and perturbation theory cannot be longer applied. This can only be solved by employing the full theory as a UV-completion, i.e. (re-)introducing the intermediate bosons.

3.3.2 Effective Higgs couplings

Calculations with heavy-fermion-loop mediated gluon-Higgs interactions can be simplified in the heavy top limit ($m_t \rightarrow \infty$). These mediated interactions can be replaced by effective gluon-gluon-Higgs vertices (cf. Fig. 3.1) [112–114].
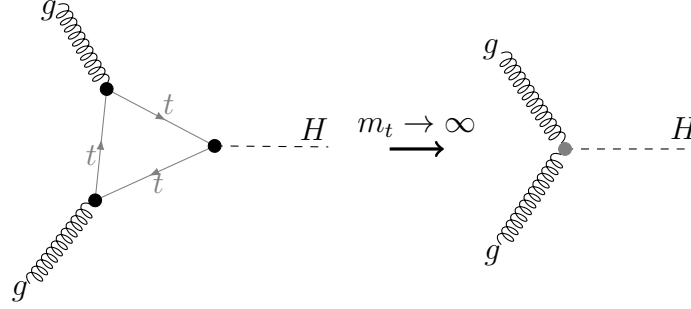
Figure 3.1: Effective gluon-gluon-Higgs vertex in the heavy-top limit.

The corresponding term in the effective Lagrangian is:

$$\mathcal{L}_{\text{Effective}} = -\frac{g_{\text{Eff}}}{4} H \operatorname{tr} G_{\mu\nu} G^{\mu\nu} \tag{3.2}$$

with an effective coupling constant g_{Eff}. Including higher order QCD corrections, its value is [115]

$$g_{\text{Eff}} = \frac{-\alpha_s \sqrt{2G_F}}{3\pi} \left(1 + \frac{11}{4\pi}\alpha_s\right) + O(\alpha_s^3) \tag{3.3}$$

in the $\overline{MS}$-scheme. $\alpha_s = \frac{g_s^2}{4\pi}$ is the QCD coupling strength parameter.

For energies below the top-pair production threshold, the effective model can be improved by expanding in $\frac{1}{m_t}$ to introduce mass effects.

For two Higgs bosons in the final state, effective Higgs couplings and expansions in $\frac{1}{m_t}$ have also been applied, see e.g. [116], but cannot substitute an NLO calculation with full top-mass dependence [117].

4 Further theoretical preliminaries

4.1 Physics at hadron colliders

At high collision energies, the description of physics at different scales factorizes according to the factorization theorem [118–120].

The cross section σ of a hadronic collision can be written accordingly as

$$\sigma(H_1, H_2 \to X) = \sum_{a,b} \int_0^1 \mathrm{d}x_a\,\mathrm{d}x_b f_{a;H_1}(x_a, \mu_F^2) f_{b;H_2}(x_b, \mu_F^2)\hat{\sigma}_{ab}\left(a, b \to X;\ \mu_F^2, \mu_R^2\right)$$

(4.1)

where the collision of two hadrons H_1, H_2 into the final state configuration X is assumed. The quarks and gluons, carrying momentum fraction $x_{a,b}$ of the total hadron momentum, enter the partonic cross section $\hat{\sigma}_{ab}$.

The first term of Eq. (4.1) describing long-distance physics is provided by the parton distribution functions (PDFs) $f(x_i, \mu_F^2)$ which are process-independent and can be determined by fitting to experimental data. The second part, the hard scattering cross section describing the small-distance physics, can be calculated perturbatively. It depends only on the momentum and identity of the involved partons, not on the full hadrons.

The hard scattering cross section is connected to the scattering matrix $\hat{S}$ that describes the probability $\mathcal{P}_{a,b\to X}$ of measuring the final state $|X\rangle_{\mathrm{fin}}$ from the initial state $|ab\rangle_{\mathrm{in}}$:

$$\mathcal{P}_{a,b\to X} = \left|{}_{\mathrm{fin}}\langle X| \hat{S} |ab\rangle_{\mathrm{in}}\right|^2.$$

(4.2)

The scattering matrix $\hat{S}$ can be split into a non-interacting part and the scattering amplitude $\hat{T}$,

$$\hat{S} = 1 + \mathrm{i}\hat{T}.$$

(4.3)

For a $2 \to n$ scattering process with momenta k_a, k_b, k_1, ..., k_n, the momentum conservation can be factored out as follows:

$$
{}_{\text{fin}}\langle k_1 \cdots k_n | \, \mathrm{i}\hat{T} \, | k_a k_b \rangle_{\text{in}} = \delta^{(4)}(k_a + k_b - \sum_{j=1}^{n} k_j) \, \mathrm{i}\mathcal{M} \tag{4.4}
$$

with the scattering matrix element $\mathcal{M}$.

Finally, the hard scattering cross section can be computed by integrating the squared scattering amplitude over the final state phase-space and dividing by the incoming flux,

$$
\hat{\sigma}_{ab} = \int \frac{1}{2E_a E_b |v_a - v_b|} \prod_{i=1}^{n} \frac{\mathrm{d}^3 k_i}{(2\pi)^3 2E_i} \delta^{(4)}(k_a + k_b - \sum_{j=1}^{n} k_j) \overline{\sum} |\mathcal{M}|^2 \tag{4.5}
$$

where E_a, E_b, $E_{1\cdots n}$ is the energy of the incoming and outgoing partons, $|v_a - v_b|$ the relative velocity of the colliding partons, and $\overline{\sum}$ the average over initial state colours and helicities and sum over final state colour and helicity configurations.

The tools and methods discussed later in this thesis focus on the hard scattering process. For the full calculation at the end of this thesis, all parts are considered.

The hard scattering matrix element $\mathcal{M}$ can be computed perturbatively by expanding in powers of the coupling constants. These correspond to extra radiation and loop-orders that implicate free momenta over which it must be integrated.

Since calculation capabilities and knowledge are limited, it is necessary (except for very specific cases where all orders can be resummed) to truncate the perturbation series at the first elements. The results depend therefore on two unphysical scales, the factorization scale μ_F, to which scale PDFs need to be evolved, and the renormalization scale μ_R, which results from UV renormalization that absorbs UV divergences in the parameters and fields. In practice, this is accomplished by adding counter-terms to the Lagrangian that cancel the UV divergences. The final result calculated at infinite orders in the perturbative series does not depend on unphysical scales. A truncation of the perturbative series results in a remaining dependency on μ_R and μ_F, which gives a hint with respect to the size of missing contributions at higher orders.

As the remaining dependency appears as logarithms of the ratios between $\mu_{R,F}$ and the (unknown) scale of the hard interaction, a scale for μ_R and μ_F is selected as an

educated guess that is typical for the process. To estimate the uncertainty, this central scale is usually varied by a factor of two in both directions.

The complexity of the calculations of processes rises with the number of involved scales, external momenta and loops.

For all phenomenologically relevant processes, next-to-leading order calculations can be made in an automated way, which is an achievement of the last decade.

Beyond one-loop, the picture is different. Only few processes have yet been calculated manually at next-to-next-to-leading-order (NNLO) or even higher order (N^{3}LO) and are becoming a main focus of research.

This thesis focuses on improvements to the automation of next-to-leading-order (NLO) calculations and one application.

4.2 NLO calculation

At NLO, in addition to the Born contribution (leading-order (LO)) three additional contributions that have the same order in the coupling constant of the perturbative series have to be taken into account.

The real-emission contribution consists of an additional parton in the final state. This extra parton may become unresolved and therefore may not be distinguishable experimentally.

The virtual contribution has the same initial and final state as the Born contribution, but contains an additional internal particle. This implies that a loop with free loop momentum arises for which integration is necessary.

The real-emission and virtual parts are usually infrared-divergent from soft and collinear divergences, but according to the KLN-theorem [121, 122] their divergences cancel each other in sufficiently inclusive, infrared-save observables and therefore their sum must be finite (except from initial state collinear singularities, which are included in the parton distribution functions (PDFs)).

The virtual contribution contains also ultraviolet (UV) divergences. By renormalization, these divergences can be absorbed into the coupling constants and fields.

Finally, the divergences can be regularized in terms of $\frac{1}{\epsilon}$-poles by going to $4 - 2\epsilon$ dimensions, as described in the next section.

With Monte-Carlo-programs, which are especially helpful for integration with cuts, the phase-space integration can only be performed with integer dimensions and the real- and virtual contributions must be integrated separately due to their different final state. To accomplish this, a subtraction term is added or subtracted as appropriate from each term, such that both terms become finite. The final result is not changed by this procedure:

$$\sigma^{\text{NLO}} = \int_m d\sigma^{\text{Born}} + \int_{m+1} \left(d\sigma^{\text{real}} - d\sigma^{\text{subtr}} \right) + \int_m \left(d\sigma^{\text{virt}} + \int_1 d\sigma^{\text{subtr}} \right). \tag{4.6}$$

This implies the introduction of subtraction terms, which are another ingredient of a common NLO calculation. They need to have a suitable infrared structure, such that they cancel the corresponding divergences.

The most widely used methods to determine the subtraction terms are the Catani-Seymour dipole subtraction method [123, 124], the FKS method [125, 126] and the Antenna subtraction [127–129], all of which are all suitable for automated calculations. In the calculation presented in Chapter 9, the Catani-Seymour method is used.

Alternatively, phase-space-slicing methods can be used (see [130–136] and references therein). They approximate the matrix element and the phase space integration measure in boundary regions and depend on (non-physical) cut-off or resolution parameters.

The virtual contribution, which is usually the most complicated part to compute, involves integrals over the free loop momentum in the loop integrals.

4.3 Loop integrals

A one-loop integral can be classified by the number and properties of incoming and outgoing momenta (called external legs), and the masses of the internal propagators. By convention, all external momenta are taken as incoming.

Whereas a large loop momentum leads to UV divergences, massless particles can cause IR and collinear divergences when they propagate in a loop, since the corresponding denominators

$$(k + r_a)^2 = -2\left|\vec{r}_a\right|\left|\vec{k}\right|(1 - \cos\theta_{\angle(\vec{r}_a, \vec{k})}) \quad (\text{with } k^2 = r_a^2 = 0) \tag{4.7}$$

with the loop momentum k and the sum of external momentum $r_a = \sum_{i=1}^{a} p_i$ can become zero if the loop momenta vanishes ($k \to 0$), the (sum of) external momenta goes to zero ($r_a \to 0$) or, in case of collinear divergences, both become parallel. These divergences are canceled by corresponding real-emission Feynman diagrams with the same massless particle and the PDFs.

There are different methods to regularize divergences, such that they can be included in the calculation and the final canceling of divergences be checked.

Beside the basic approach of cut-off-regularization, which uses bounds to isolate UV and IR divergences (but breaks gauge-invariance and is not suitable for non-abelian theories) dimensional regularization [137–140] is usually used nowadays, which preserves gauge and Poincaré invariance. The idea is to calculate the loop amplitude (at least partially) in a D-dimensional space instead of the ordinary $3 + 1$-dimensional Minkowski space.

To be able to perform the limit $D \to 4$ at the end of the calculation, all (temporary) divergences must cancel each other for all physical quantities.

As the singularities appear in this limit, $D = 4 - 2\epsilon$ or $D = 4 - \epsilon$ is usually used and, accordingly, the limit $\epsilon \to 0$. UV divergences are regularized by assuming $D < 4$, i.e. $\epsilon > 0$. For IR and collinear divergences, an analytic continuation to $D > 4$ ($\epsilon < 0$) is used (see e.g. [141]).

At the one-loop-level, the Laurent expansion in ϵ of the result can always be written in *double-pole* terms of $O\left(\frac{1}{\epsilon^2}\right)$, *single-pole* terms of $O\left(\frac{1}{\epsilon}\right)$ and the *finite part* of $O(1)$. Terms of $O(\epsilon)$ or higher can be neglected, as they disappear in the limit $\epsilon \to 0$ (described e.g. in [142]).

A matrix element of an N-point one-loop integral can therefore be written in the case of QCD corrections as follows:

$$\left|\mathcal{M}_{\text{1-loop}}\right|^2 = r_{\text{convention}} \cdot \left(\frac{c_{-2}}{\epsilon^2} + \frac{c_{-1}}{\epsilon} + c_0 + O(\epsilon)\right) \tag{4.8}$$

where a factor

$$r_{\text{convention}} = \frac{\alpha_s(\mu_R)}{2\pi} \frac{(4\pi)^\epsilon}{\Gamma(1 - \epsilon)} g_s^{2b} \tag{4.9}$$

can be placed outside the brackets. Γ denotes Euler's gamma function and $2b$ the order in g_s of the underlying Born process, and μ_R the renormalization scale.

There are different schemes for dimensional regularization: A common choice is the 't Hooft-Veltmann scheme ('t HV) [138] or conventional dimensional regularization

(CDR) [143] (which are equivalent at one-loop), where internal states or, respectively, all states are treated as D-dimensional, i.e. their spin and momenta degree of freedom (d.o.f.) continued from four to D dimension.

Another possibility is dimensional reduction (DRED) [144, 145], which is especially useful for SUSY calculations, since the number of bosonic d.o.f. matches the number of fermionic d.o.f.. The four-dimensional space is compactified to a (smaller) D-dimensional space. Momenta and integration measures are adapted, but gamma matrices, for example, are kept in four dimensions (cf. [146]).

In the GoSam framework presented below (Chapter 5, p. 43), DRED is used by default and if desired, the squared one-loop matrix-element $\left|\mathcal{M}^{(\mathrm{DRED})}\right|^2_{\mathrm{NLO}}$ converted to 't HV/CDR using the conversion formula (cf. [50])

$$\left|\mathcal{M}^{(\text{'t HV/CDR})}\right|^2_{\mathrm{NLO}} = \left|\mathcal{M}^{(\mathrm{DRED})}\right|^2_{\mathrm{NLO}} - \frac{\alpha_s}{2\pi}\left|\mathcal{M}^{(\mathrm{DRED})}\right|^2_{\mathrm{LO}}\sum_k \tilde{\gamma}_k^{(\mathrm{DRED})}. \tag{4.10}$$

$\sum_k$ denotes the sum over external massless partons with $\gamma_k^{(\mathrm{DRED})} = \frac{C_F}{2}$ for massless quarks and anti-quarks, $\gamma_k^{(\mathrm{DRED})} = \frac{C_A}{6}$ for gluons, which include the QCD colour factors $C_F = \frac{4}{3}$ and $C_A = 3$. $\left|\mathcal{M}^{(\mathrm{DRED})}\right|^2_{\mathrm{LO}}$ is the squared Born-level matrix element calculated in DRED.

All loop-integrals can be represented by a linear combination of a set of 'basis' integrals[1] plus rational terms. At the one-loop level, possible sets of these integrals are known. The usually used 'basis' integral set contains scalar integrals with up to four external legs (see e.g. [141]). Choosing integrals in six- and eight-dimensions as 'basis' integrals, which are partially UV/IR finite, helps thereby to separate divergences [147].

There are multiple ways to obtain coefficients of these 'basis' integrals.

More traditional approaches reduce tensor integrals analytically. The tensor integral library Golem95C [3, 51, 52] follows this approach. In Chapter 7, p. 63, its method is explained in detail and extended towards higher-rank tensors.

The coefficients can also be reconstructed from scattering amplitudes by exploiting their analytic structure, especially unitarity (i.e. the conservation of probability) or infrared singular behaviour. Cutting the loop amplitude, i.e. putting internal propagators on-shell, helps to deduce the coefficients of the 'basis' integrals iteratively or recursively.

---

[1]The integrals are only end-points of the reduction algorithms. In a mathematically sense, they do not form a basis. Often, they are also called master integrals.

It is possible to determine the coefficients already at the integrand level without performing any integration. This is used in the OPP approach [148–150]. Similar methods are introduced in [151, 152].

Over the last decade, multiple tools have been developed for performing NLO calculations using various techniques to calculate loop integrals. One of them is GoSam [2, 49, 50] which is described and used later in this thesis. Other programs that can deliver amplitudes for processes at one-loop level in an automated way (or at least offer them for some categories of processes as a library) are, for example, BlackHat [153], FeynArts and FormCalc [154–156], GRACE-loop [157], Helac-NLO [158], MadGolem [159], MadGraph5_aMC@NLO [160], MCFM [72], NJet [161], OpenLoops [162], Recola [163] and VBFNLO [164]. With a few exceptions, they are available publicly.

4.4 Parton shower

In the calculation presented in Chapter 9, p. 81, parton shower effects are studied, therefore, a short overview about parton showers and related techniques is given in this section.

In parton shower calculations, radiation effects such as additional QCD Bremsstrahlung are added to the hard subprocesses that are described by the matrix elements calculated at fixed order.

Not only the final state particles can radiate, but also the initial state partons. Additionally, multiple parton interactions can be taken into account, i.e. simultaneously occurring collisions of spectator partons (beam remnants) that do not belong to the primary hard process.

The parton shower is calculated in Markov processes, where further particles are added to the hard subprocess. Thereby, four-momentum and probability (i.e. unitarity) of the described process need to be conserved.

Colour confinement forbids that coloured particles (gluons, quarks) exist individually for a longer time, therefore coloured particles combine (hadronize) into colourless hadrons. These hadrons mostly decay further. As hadronization involves mostly non-perturbative processes, its properties need to be deduced from measurements. The jet structure, which describes the distribution of energy in the final state by clustering it in (usually) narrow cones, should be related to the structure of partons in the hard subprocess. Hadronization needs therefore to be infrared and collinear

safe, i.e. should not depend on additional, unresolved radiation. See e.g. [165] for more details.

In the case of combining processes with different parton multiplicities and parton shower, *double-counting* must be avoided. There are multiple algorithms for achieving this merging and matching.

One approach for merging processes calculated at LO matched to parton showers is the CKKW algorithm [166, 167], which separates the domains of the matrix elements and the parton shower by jet resolution defined by the $k_\perp$-jet-clustering algorithm [168] (also known as Durham algorithm). A variant is the CKKW-L algorithm [169]. There is also the MLM approach [170, 171].

For NLO calculations with parton shower, double-counting issues are immanent due to the real-radiation part. This can be solved by using matching algorithms like MC@NLO [172–174]. A competitive approach is POWHEG matching [175] that avoids negative weights.

Both techniques, merging (combining calculations with different jet multiplicities) and matching (including parton showers, especially to processes calculated at higher orders) can be combined in NLO merging schemes such as, for example, NL^3 [176], FxFx [177], MEPS@NLO [178] or UNLOPS [176, 179].

Today, parton shower and hadronization are integrated in most Monte-Carlo event generators, progressively combined with matching and merging procedures. Examples for Monte Carlo programs (MCs) that implement at least parts of the mentioned algorithms are Herwig/Herwig++ [180–182], Sherpa [183], Pythia [184, 185] with its VINCIA plugin [186–189], or Ariadne [190].

Using fully resumed results, higher logarithmic accuracy can be reached. This is implemented in the Geneva Monte Carlo framework [191].

Part II

Automation: Concepts and Tools

5 GoSam 2.0

Part II of this thesis introduces further concepts and tools applied in the automation of NLO calculations.

In this first chapter of this part, the software framework GoSam is presented. Several developments, summarized in the 2.0 release and partially implemented by the author, are discussed.

The improved interface of GoSam to Monte Carlo programs (also partially author's work) is discussed in Chapter 6. GoSam and especially this interface are later employed in the last part of this thesis (Chapter 9).

The two last chapters of this part focus on the integral library Golem95C, which is used by GoSam.

Chapter 7 discusses an extension to higher tensor-ranks, which is useful for calculations with e.g. effective field theories or spin-2 particles. It completes the author's developments in Golem95C towards higher ranks, introduced in [192]. These earlier developments were already applied in [4].

Chapter 8 on numerically calculated box integrals presents a possible means of improving the numerical stability for exceptional kinematics in Golem95C.

5.1 Overview

GoSam [2, 49, 50] is a program package that can provide multi-particle one-loop amplitudes in a fully automated way. It is especially useful for calculating QCD corrections to processes in the SM and beyond. Internally, a Feynman-diagram based approach is applied and projections onto helicity amplitudes are used. GoSam has been used in various calculations [1, 4, 5, 193–207].

For these calculations, GoSam has to be combined with MCs that provide the real radiation and subtraction, perform the phase space integration and optional showering and hadronization. Mainly the software package Sherpa [183] or the combination

of MadGraph4 [208], MadDipole [209, 210] and MadEvent [211] were used as MC programs. Recently, GoSam has been combined with Herwig++/Matchbox [6, 180–182, 212], which is used later in this thesis, MadGraph5_aMC@NLO [160, 206] and the POWHEG BOX [213, 214]. In addition, GoSam can be interfaced now inside WHIZARD [215] as One-Loop provider (OLP) [216, 217]. It has also been used to calculate electroweak corrections [218, 219].

These combinations of tools allow fully automated NLO calculations to be performed including matching to parton showers.

5.2 Workflow

GoSam can be controlled via an input file (called *input card*) or the standard interface to Monte-Carlo programs, as explained further in Chapter 6, p. 55. These interfaces allow the user to specify the process requested, i.e. its initial and final state, the order in coupling constants, and further settings such as which reduction program should be used by GoSam.[1]

The workflow of GoSam is shown in Fig. 5.1. After reading the input card, GoSam calls QGraf [220] to generate Feynman diagrams. Beside the default diagram selection settings in QGraf, GoSam can filter the diagrams in addition: Via the input card, the user can provide custom filters using Python expressions to exclude or select specific diagrams.

To control the finally used diagrams, the user can create a documentation that includes all Feynman diagrams and further information about the process such as a list of the helicity configurations.

Using FORM[2] [221–223] with the Spinney library [224], GoSam transforms the diagram expressions which are generated by QGraf into computable code.

This code still needs to be divided into sub-expressions because the optimization routines in Fortran compiler usually cannot deal well with huge expressions. This partitioning is performed either by the new FORM [223] features to write optimized code or Haggies [225].

---

[1]Some settings can only be set via an input card that can be provided in all cases to GoSam. In case of the standard interface to Monte-Carlo programs, also multiple processes can be requested simultaneously.

[2]FORM is a computer algebra system especially built to manipulate huge expressions.
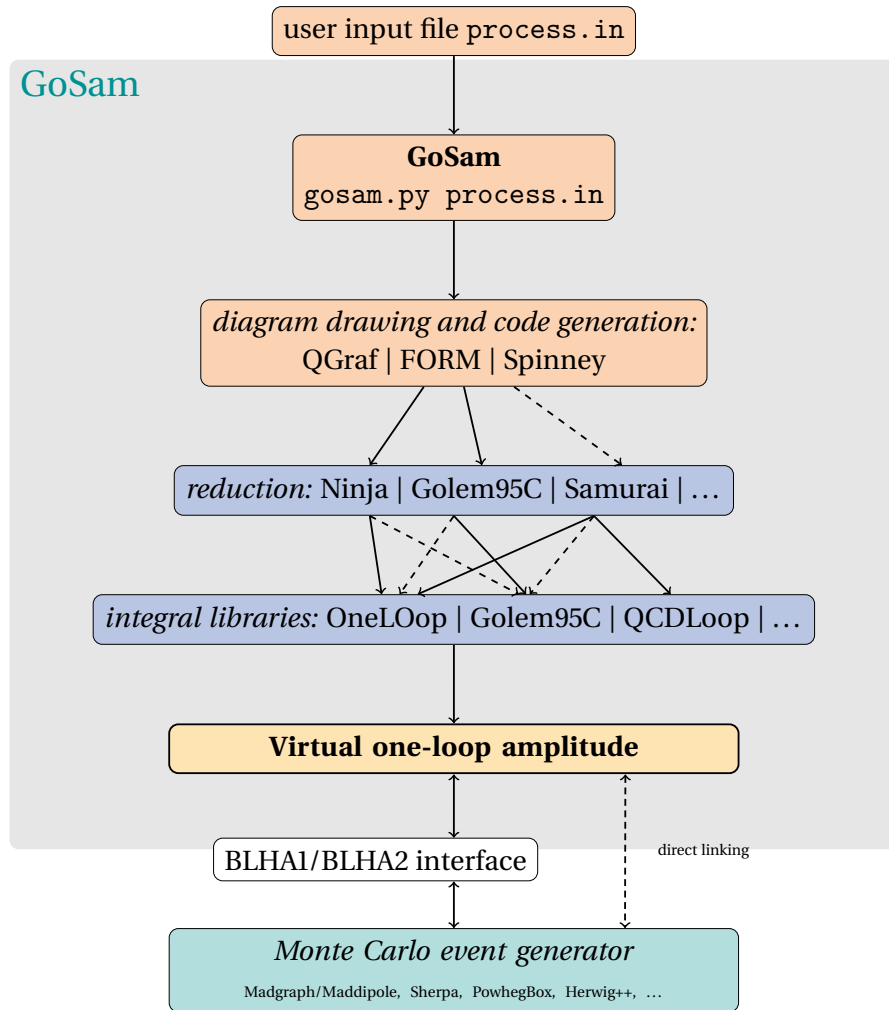
Figure 5.1: Basic workflow scheme of GoSam 2.0.

The reduction of the loop integrals is done either using the OPP approach [148, 149] or by means of a more 'traditional' approach using Golem95C [3, 51, 52].

For the OPP approach either the integrand reduction via Laurent expansion [226] implemented in Ninja [55, 56] or Samurai [53, 54] can be used, which implements a generalized D-dimensional unitary-cut technique and polynomial interpolation with Discrete Fourier Transformation of the numerator.

For the approach with Golem95C, the coefficients are determined by tensorial re-

duction [227] using derivatives of the numerator $\mathcal{N}(q)$ evaluated at $q = 0$.[3] How Golem95C calculates tensor integrals is described in Section 7.2, p. 65.

These reduction libraries use internally the integral libraries QCDLoop [228, 229], OneLOop [230] or LoopTools [155], which depend partially on scalar one-loop functions of the library FF [231], but especially in the case of Golem95C, most integrals are directly implemented.

In addition to the internal model files for the SM with and without the diagonal CKM-matrix, the Minimal Supersymmetric Standard Model (MSSM) and SM plus an effective gluon-Higgs-coupling (cf. Section 3.3.2, p. 32), GoSam has also support for Universal FeynRules Output (UFO) model files [232]. This allows BSM calculations since UFO-model files can be generated by FeynRules [233, 234] from (nearly) arbitrary Lagrangians. SARAH [235], which starts from given symmetries of a model instead of its Lagrangian, also supports UFO-model files as output format.

Additionally, an experimental support for PJFry [236–238], which is another one-loop tensor integral library, is currently included in GoSam.

The generated code, which can calculate the virtual one-loop amplitude at arbitrary phase space points, is finally provided as a library to the user and can then be interfaced by Monte-Carlo program and used, for example, in full NLO calculations.

5.3 New features of GoSam 2.0

The GoSam version 2.0 introduces various improvements and new features. Some of them are described in separate chapters of this thesis:

- The support of the Binoth Les Houches Accord 2 (BLHA2) [8] and various electroweak schemes including their automatic choice is presented in Chapter 6, p. 55.

- How loop-integrals with higher tensor ranks can be calculated with Golem95C, is described in Chapter 7, p. 63 .

---

[3]With the extension `noderive`, the numerator is alternatively evaluated at several points which produces usually less accurate results but reduces slightly the code generation time and can also be used as an internal check of the derivation method.

New reduction method and optimized code generation
GoSam 2.0 uses the new integrand reduction method via Laurent expansion implemented in the Ninja library [55, 56] as mentioned before.

The previously mentioned optimized code generation via the corresponding new FORM feature [223] is also used since GoSam 2.0.

Summing and grouping diagrams with common substructure
In GoSam 2.0, the GoSam 1.0 capabilities of grouping similar diagrams (more exactly diagrams that share a common set of denominators) is extended further. With the new option `diagsum`, diagrams that share at least a common-loop structure (including different particles in the loop) are combined and evaluated together, which increases the performance and reduces the code size.

Numerical polarization vectors
For massless gauge bosons (gluons and photons), GoSam 2.0 uses numerical polarization vectors. This allows code to be shared between different helicity configurations of these particles and, therefore, decreases not only the code generation time, but also the memory and disk footprint of the code generated by GoSam. This feature can be switched off if needed, for example, to verify Ward identities or to allow manual selection of reference vectors for each helicity configuration.

Improved rescue system
Possible numerical errors influence the reliability of all numerical calculations in finite precisions. Especially in higher order calculations, where all kinds of (spurious/cancelling) singularities occur, it is important to estimate the final uncertainty and to detect and solve (*rescue*) unstable points as far as possible. If needed, GoSam re-calculates the result for a phase space point by using another reduction method. By default, Golem95C is used as rescue system.

GoSam uses a combination of different checks to determine the quality of its result and returns an estimated precision. The first method is to compare calculated infrared pole coefficients with their analytic values, which result from the universal structure of IR singularities in QCD. Within certain limits [56], the precision of the finite term is correlated with the pole precision, which can therefore be used to estimate the precision of the finite part.

The number of valid digits (precision) can be calculated as

$$p_{\text{IR-check}} = -\log_{10}\left|\frac{c_{-1} - c_{-1,\text{IR}}}{c_{-1,\text{IR}}}\right| \tag{5.1}$$

with c_{-1} the calculated single pole coefficient (cf. Eq. (4.8), p. 37) and $c_{-1,\text{IR}}$ the analytic infrared pole coefficient.

The finite part can be tested directly by exploiting symmetry properties of amplitudes, which requires re-evaluation of the phase space point with a changed kinematic point that should lead to the same result by symmetry, and comparing the result with the original one.

GoSam uses a *rotation test* (cf. [56]), in which all momenta are azimuthally rotated around the beam axis. As this should leave the result invariant, but triggers possible numerical instabilities in a different way, it is a good method for determining the precision of the result. The disadvantage is that the amplitude must be evaluated twice, which is time consuming as it doubles the evaluation time per phase space point.

The estimated precision obtained by the rotation test is obtained by

$$p_{\text{rotation}} = -\log_{10}\left(2\left|\frac{c_0 - c_{0,rot}}{c_0 + c_{0,rot}}\right|\right). \tag{5.2}$$

Another similar possibility would be a *scaling test* [239], in which all involved physical scales are multiplied with a factor. Due to the known scaling behaviour of the amplitude, the result can be compared with the original one and its precision determined.

If phase space point checks are not completely disabled, GoSam first performs the pole check and, if the estimated precision is neither good enough to accept the result nor low enough to trigger directly the rescue system, GoSam performs additionally a rotation test. If the estimated precision of the result is below a limit (settable by the user), the rescue system is triggered, i.e. Golem95C used to evaluate the phase space point. Its result is also checked and the final estimated precision returned.

Tensorial reconstruction
GoSam 2.0 also now uses the previously mentioned tensorial reconstruction via derivation by default. This increases the precision of the rescue system compared with the previously used numerical reconstruction of the integrand.

New installation

The install process of GoSam itself has been simplified by a new user-friendly install script. It helps to download, build and install GoSam and all the necessary components, such as the various integral and reduction libraries, QGraf and FORM in an automated and portable way. In addition, it allows automatic updates (and also uninstallation) of GoSam itself and its components.

Improved user-interface

The input card of GoSam has been simplified: New parameters have been introduced and existing ones given useful default parameters. Numerous features, which in GoSam 1.0 were accessible only by the `extensions` parameter, have their own configuration field (new fields are e.g. `regularisation_scheme`, `reduction_programs`, `polvec_method`).

Compiler flags, such as paths to installed libraries, are determined in standard installations in an automated way and therefore do not need to be set by the user in the input card.

Numerous other small improvements have also been made; for example, output directories are now created automatically and do not need to be created by the user by hand.

5.4 Precision check for loop-induced processes

The pole check mentioned previously cannot be applied directly to loop-induced processes, as their single and double pole coefficients vanish. It is, however, still possible to use the calculated pole values to detect points that cause numerical instabilities.

This section explains how this can be performed and demonstrates its effectiveness by examining an example. At the second part of this section, another precision check is introduced and applied to test the validity of the rescued points. Both checks were implemented by the author of this thesis.

As a measurement of the single pole quality, the following value is introduced:

$$q_{\mathrm{pole}} = -\log_{10}\left(\left|\frac{c_{-1}}{c_0}\right|\right) \tag{5.3}$$

where c_{-1} is the result of the single pole coefficients (the $\frac{1}{\epsilon}$-part of the amplitude) and c_0 the finite part (cf. Eq. (4.8), p. 37).

This value indicates how many orders of magnitude the single pole coefficient is smaller than the finite part.
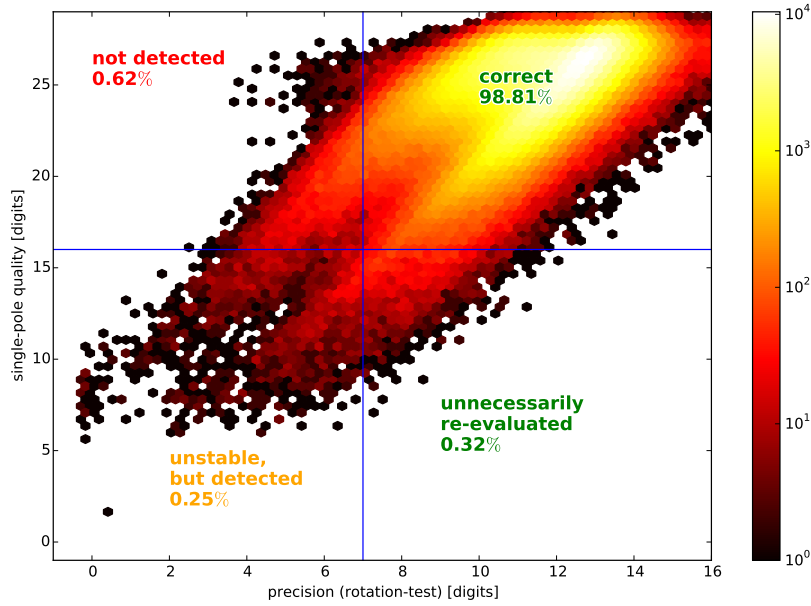
Figure 5.2: Result of a simulation with 1×10^6 points (generated by GoSam's RAMBO) for the loop-induced $gg \rightarrow WW \rightarrow l\nu l'\nu'$ with only Ninja enabled (rescue system disabled). The pole quality check can be used to distinguish most stable points from (maybe) unstable points that need further testing.

As shown in Fig. 5.2 for the loop-induced process $gg \rightarrow WW \rightarrow l\nu l'\nu'$ (corresponding Feynman diagrams are listed in Appendix C.1, p. 127) including massive bottom- and top-loops calculated with GoSam/Ninja (without rescue system), q_{pole} often correlates with the precision obtained by the rotation test[4]. For this plot, 1×10^6 events are generated by GoSam's RAMBO event generator, evaluated with Ninja and tested with the pole and rotation test. The colour in the plot shows the density of these events in each region in a logarithmic scale.

For the selected process, a pole quality limit of 16 digits has been chosen ($q_{\mathrm{pole}} > 16$) and a gainable precision of 7 digits.

---

[4]The result of the rotation test itself correlates strongly with the precision obtained by comparing with the rescue system (Golem95C) and can therefore be taken as an approximation of the true precision.
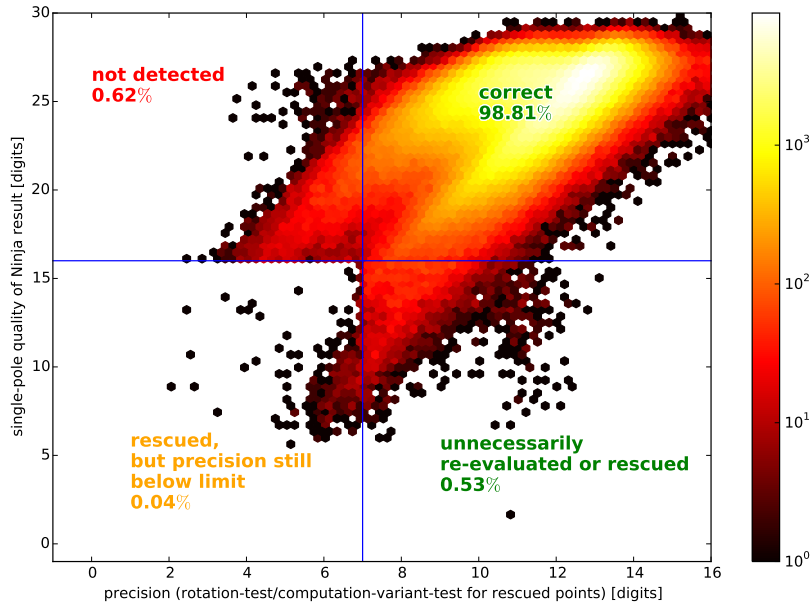
Figure 5.3: Same plot as in Fig. 5.2, but with rescue system (Golem95C) enabled. Nearly all unstable points could be rescued to sufficient precision, whereas the precision of few points is still below the limit.

The horizontal and vertical lines separate different regions: All events below the horizontal line have low pole quality and are therefore tested by the rotation test and rescued as required (i.e. if they are in the left-lower quarter). The vertical line splits the points with precision below and above the wanted precision (here 7 digits). The events resulting in dots in the right-lower quarter ('false positives') are (unnecessarily) re-tested which nearly doubles their evaluation time.

The problematic points are in the upper-left quarter ('false negatives'): Their pole quality is above the limit and are therefore missed by the test, but they do not satisfy the precision that should be gained. Still, their fraction is low and as it can be seen, their precision is still quite good (mostly only a few digits below the precision limit), whereas the precision of the true-positives is in part very low, which could have a non-negligible impact on the precision of the end result after the phase space integration.

By raising the limit on q_{pole}, the fraction of false negatives can be further reduced, but also the fraction of true-negatives increases, so that the runtime trade-off is high.

For simpler processes (especially without internal masses), the limit on q_{pole} can be increased to increase the discrimination power of the pole quality check.

In Fig. 5.3, p. 51, the same plot as in Fig. 5.2 is shown with the rescue system, i.e. Golem95C, enabled. This results in the events in the bottom left corner being re-evaluated by the rescue system and therefore shifted horizontally in the plot, as on the x-axis, the estimated final precision is plotted. It is apparent, whilst the rescue system improved the precision, it did not reach the desired precision in all cases (this might be related to the precision test used, see below).

The rotation test cannot be used to estimate the precision of the rescued results, because the internal representation of the kinematics in Golem95C is rotation-invariant and therefore the computation is not really changed by rotation of the kinematics.

The precision of the rescued points is therefore measured here using a newly developed computation-variant test inside Golem95C, published in its recent 1.3.3 release. It is similar to a scaling test, but more user-friendly as most of its parts are hidden inside the library: The computation-variant test changes the way how the $\mathcal{S}$-matrix (defined in Eq. (7.5), p. 64) is normalized inside Golem95C: To improve the numerical stability, the $\mathcal{S}$-matrix is normally divided by its biggest element. This scaling is then undone in the results returned. Instead, with the computation variant (No. 1) enabled, the second largest element of the $\mathcal{S}$-matrix is used.[5,6] This changes the internal computation in such a way that the numerical precision can be estimated by comparing the final result with the default behaviour.

This computation-variant test has not yet been studied fully. It probably underestimates the real precision by a few digits, as it compares with results that are in most cases non-optimally computed, such that the number of really rescued points might be much higher (as most rescued points are near the more or less arbitrary limit).

For Golem95C, the pole quality is in general quite high and correlates only weakly with the precision of the finite part, such that a pole-quality test would have only low discriminatory power and is therefore not really useful.

In summary, a precision test for loop-induced processes has been presented. In the example used, nearly all events could be rescued to high precision. Further studies are needed to determine whether the precision measure used for the rescued points estimates their precision correctly. One possible way would be to compare with results calculated in quadruple precision.

The described precision test, based on the pole quality and the rotation test has been implemented in GoSam, such that GoSam can also return the estimated precision of

---

[5]The divisor is automatically down-scaled if the second largest element is too close to the largest element (in absolute values) which would otherwise lead to too little or no effect.

[6]Computation variant No. 2 disables the normalization of the $\mathcal{S}$-matrix completely, which reduces usually the stability of the results further.

its result for loop-induced processes and if needed, call its rescue system. This allows reliable calculations for loop-induced processes.

The new computation-variant inside Golem95C, which was employed to determine the precision of the rescue system, is not yet used inside GoSam, but can easily be integrated as soon as further analysis determine how its results map to the true precision.

6 Implementation of the Binoth Les Houches Accord 2 in GoSam

6.1 Introduction

The Binoth Les Houches Accord (BLHA) provides a standardized interface between Monte Carlo programs (MCs) and One-Loop providers (OLPs) such as the program package GoSam. Whereas GoSam 1.0 supports only the first version of the standard, the original version of the Binoth Les Houches Accord (BLHA1) [240], GoSam 2.0 also implements BLHA2 [8].

In the past, OLP-specific interfaces needed to be implemented separately for every used OLP. The BLHA reduces or, ideally, nearly abolishes the effort to support different OLPs in a MC. In theory, the interface needs to be implemented only once on both sides, and any combination of MCs and OLPs can be combined.

In practice, all MCs and OLPs are, at least in a certain sense, specialized or focused (e.g. regarding high multiplicities in the final state, BSM-capabilities, electroweak corrections) and therefore not all combinations make sense. Moreover, still OLP-specific code is needed.[1]

Additionally, the BLHA2 cannot, of course, cover all implementation choices and possible extensions. Some parts of the BLHA2 are marked as optional and, therefore, do not need to be supported by every OLP.

The first part of this chapter explains the features of the BLHA2. In the second part, some of the implementation choices that were made for the current implementation of BLHA2 in GoSam 2.0, are described. The author of this thesis was involved in the formulation of the BLHA2 and implemented most of its new features in GoSam.

Using the BLHA2 implementation in Herwig++/Matchbox, the BLHA2 interface of GoSam has been tested and verified in $pp \to Z/\gamma * +\mathrm{jet} \to e^+e^- + \mathrm{jet}$ and various

---

[1] For example, OLP-specific code is needed to let the OLP read in the order card initially and is often useful to set various OLP-specific options, like Feynman diagrams that should be excluded.

other processes [6, 182]. The calculations shown in Chapter 9 use also the BLHA2 interface.

Beside Herwig++/Matchbox, WHIZARD is also interfacing GoSam via the BLHA2.

On the other hand, the interfaces of MadGraph5_aMC@NLO, POWHEG BOX and Sherpa still rely on the BLHA1 interface of GoSam 2.0.

An alternative runtime interface between MC and OLP programs has been suggested in [241], but did not become an accepted standard.

Beside the BLHA, the Les Houches Accord (LHA) for user-defined processes [242–245] is also available. It defines how events from parton level generators can be transferred to showering and hadronization event generators, which are, however, nowadays often already combined into one program such that an extra interface is not needed anymore. Nevertheless, its Les Houches Event File (LHEF) file format is still used widely to store or buffer already showered events for later or parallel analyses with third-party tools such as Rivet [246].

6.2 BLHA2

6.2.1 Workflow

The communication between the MC and OLP can be divided into three phases (cf. Fig. 6.1):

The pre-runtime/preparation phase
In the first step, the MC 'orders' all needed subprocesses from the OLP. It creates an input file, the *order file*, and calls the OLP, which answers with a *contract file* that labels each subprocess with an unambiguous number[2].

In this step, the OLP usually creates code that needs to be compiled or processed further before it can be linked by the MC.

---

[2]Caveat: With GoSam, the number in the label does not necessarily coincide with the order in which the processes are specified in the order file.
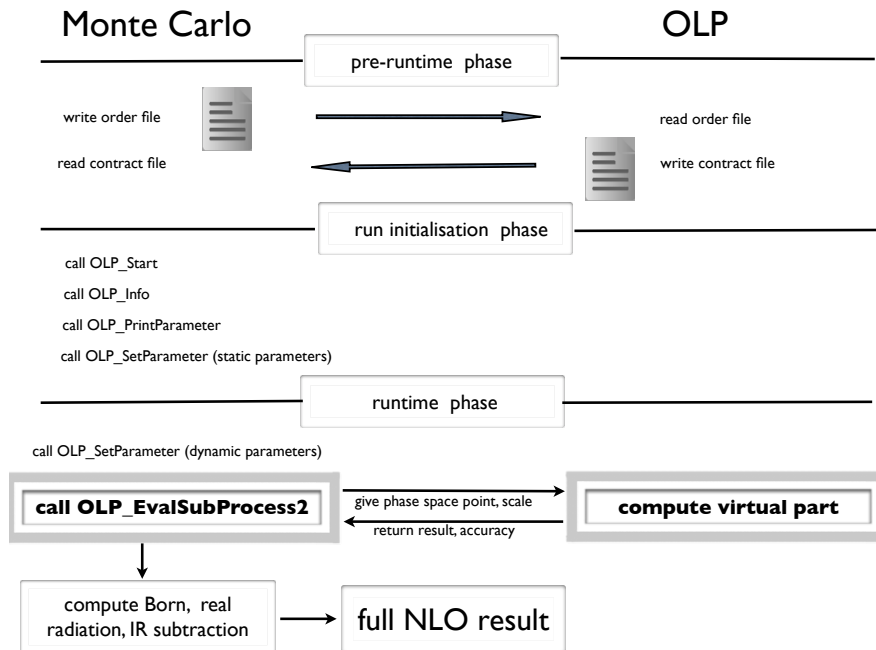
Figure 6.1: Workflow of the BLHA2 interface [8].

The initialisation phase

Here, the MC asks the OLP to initialise its runtime code via the function `OLP_Start`. Additionally, (static) parameters such as particle masses or couplings can be set (using `OLP_SetParameter`).

The runtime phase

For each part of the calculation, phase space points are generated by the MC. The corresponding amplitudes are either calculated internally (for tree-level processes such as the Born or real-radiation contribution including infrared subtraction) or via the OLP (mainly the virtual amplitude) using the interface function `OLP_EvalSubProcess2` and the subprocess label from the contract file. Runtime parameters (e.g. running couplings) can be changed via `OLP_SetParameter`.

With the BLHA2 interface, the Born or real-radiation amplitudes can also be calculated by the OLP.[3]

---

[3]For completeness: Some MCs (such as e.g. Herwig++/Matchbox) have also code for specific virtual amplitudes built-in which can substitute or complement the OLP.

The MC uses this information to perform the full NLO result. In particular, it builds the subtraction terms, integrates over the phase space and combines the different contributions of the NLO calculation, optionally with attached parton shower and hadronic decays.

6.2.2 New features

In comparison to BLHA1, the interface has been extended in several ways.

One of the main new features is that BLHA2 allows subprocesses with different properties/settings to be placed in one order card. This is especially helpful for merging procedures with different jet multiplicities or mixed QCD-electroweak calculations.

As different kinds of matrix elements (tree-level, loop, loop-induced, spin-/colour-correlated) can be mixed, the MC can now use the OLP (as far as it supports it) for different parts of the NLO calculation.

Even parts of a NNLO prediction like the real-virtual, virtual squared[4] or double-real contribution can be retrieved via the BLHA2 interface.

The adaption of parameters such as masses or coupling constants, diverging from the used model file, has been standardized with the new function `OLP_SetParameter` and is now also supported during runtime. The new function `OLP_PrintParameter` can likewise be used to write the value of all currently used parameters to a file, which is helpful for verifying the parameter set.

Another new function `OLP_Info` returns the currently used version of the OLP program and the literature which should be cited if the OLP is used.

6.3 Implementation details

GoSam can provide colour- and spin-correlated matrix elements that are helpful for building Catani-Seymour subtraction terms [123] (cf. Section 4.2, p. 35). According to BLHA2, entries for non-coloured legs should be 'ignored'. The interpretation of this in GoSam is that in the colour and spin matrices, the corresponding rows/columns are not present (i.e. skipped) and therefore maximally dense matrices are returned.

---

[4]At least with GoSam, the virtual squared term can be calculated by declaring the process to be loop-induced.

input variables	derived variables	No. of GoSam ew-scheme
G_F, m_W, m_Z	e, $\sin\theta_W$	1
α_{EW}, m_W, m_Z	e, $\sin\theta_W$	2
α_{EW}, $\sin\theta_W$, m_Z	e, m_W	3
α_{EW}, $\sin\theta_W$, G_F	e, m_W	4
α_{EW}, G_F, m_Z	e, m_W, $\sin\theta_W$	5
e, m_W, m_Z	$\sin\theta_W$	6
e, $\sin\theta_W$, m_Z	m_W	7
e, $\sin\theta_W$, G_F	m_W, m_Z	8

Table 6.1: Supported electroweak schemes by GoSam. G_F and α_{EW} are not used internally, therefore not calculated as derived variables.

Depending on the chosen model, GoSam's implementation of `OLP_SetParameter` supports names such as `mZ` or `wZ` for mass and width of the *Z* boson etc., in addition to the standardized `mass(PDG-code)` and `width(PDG-code)` parameter names, where PDG particle numbers ('codes') [247] are used. Furthermore, `alpha` or `alphaEW` (for the electroweak coupling constant $\alpha_{EW} = e^2/4\pi$) and `alphaS` or `aS` (for the QCD coupling constant $\alpha_s = g_s^2/4\pi$) are supported.

6.3.1 Electroweak scheme choice

In the SM, the various electroweak parameters are related (cf. Eqs. (6.1) and (6.2)). Therefore it is useful to specify only few of them as input parameters and calculate the others as derived parameters.

As there is no common standard, GoSam supports various electroweak schemes for the built-in models, i.e. offers the possibility of selecting which parameters are input parameters and which are derived (cf. Table 6.1 and [2, Sec. 3.3]).

The final scheme is chosen automatically[5] as soon as three electroweak parameters

---

[5]For automatic setting of the electroweak scheme, the setting `model.options` in GoSam input card needs to contain the `ewchoose` option (set by default).

are set via `OLP_SetParameter`. Using the (leading-order) relations

$$\frac{G_{\mathrm{F}}}{\sqrt{2}} = \frac{\alpha_{\mathrm{EW}}\pi}{2m_{\mathrm{W}}^2 \sin^2\theta_{\mathrm{W}}} = \frac{e^2}{8m_{\mathrm{W}}^2 \sin^2\theta_{\mathrm{W}}} \tag{6.1}$$

$$\sin^2\theta_{\mathrm{W}} = 1 - \frac{m_{\mathrm{W}}^2}{m_{\mathrm{Z}}^2}, \tag{6.2}$$

GoSam calculates the missing ones.[6]

Only the internal GoSam model files support different electroweak schemes. If not otherwise specified in the `model.options` parameter in the input card or if the automatic choice is disabled, GoSam assumes the set (α_{EW}, m_{W}, m_{Z}) by default.

For UFO-models, the electroweak scheme is fixed and depends on the input files used to generate the UFO-models.

6.3.2 Other implementation choices

The following implementation choices and derivations from the BLHA2 can be found in GoSam 2.0:

- The keyword `CouplingPower`, which allows to specify the coupling powers of the process requested, is only supported for SM couplings, not BSM couplings[7]. Currently, it needs to be set to the order of the (possibly fictional) Born-level process.

- In contrast to BLHA2, if only `CouplingPower QCD` or `CouplingPower QED` is provided in the input card, the omitted coupling order is not forced to be zero, but ignored, i.e. all diagrams at the specified QCD or QED order are used. Diagrams beyond one-loop are not generated.

- The keyword `WidthScheme` defines the treatment of unstable particles. By default, the `FixedWidth` scheme is used in GoSam. The `ComplexMass` scheme is also supported. Not (yet) supported are the `RunningWidth` and `PoleApprox` scheme, see e.g. [245].

---

[6] For the built-in `sm_complex` and `smdiag_complex` model, the widths of the vector bosons are also included in the conversion formulae. In all cases, widths are input parameters and not re-calculated.

[7] BSM coupling order can be set only via the QGraf verbatim options in a separate GoSam input card.

6.3.3 Extensions to BLHA2

For interference between Born and loop-induced processes (e.g. for processes that are loop-induced in the SM, but for which a BSM Born-level process exists), a new `AmplitudeType LoopInterference` (alias `LIEffInterference`) has been introduced. In contrast to `AmplitudeType Loop`, the phase-point check for loop-induced processes is used.

This extension for interference terms was developed by the author and is used for the calculations presented in Chapter 9, p. 81.

7 Higher rank integral reduction

7.1 Introduction

GoSam 2.0 includes the support of higher rank tensor integrals (explained in this chapter) which can occur in loop-calculations with spin-2 particles (gravitons / Kaluza-Klein modes), in EFT models, and calculations with other gauges than the Feynman gauge. In SM calculations within the Feynman gauge, this case does not occur, since the tensor rank of one-loop integrals is here always smaller or equal to the number of propagators.

In this chapter, the extension to higher ranks of the reduction and integral library Golem95C is discussed. After a short introduction to the reduction method in Section 7.2, p. 65, the formulae for pentagons and hexagons are presented in Section 7.3, p. 70 and finally the implementation details are discussed in Section 7.4, p. 71.

Higher rank support has been also implemented for the case of one additional rank in Ninja [55, 56] and in the XSamurai extension [54] of Samurai [53].

The method described in this section and the used conventions follow the work in Refs. [51, 147]. Detailed descriptions can also be found in Refs. [49, 192, 248].

A general one-loop integral in dimension D with N external legs of momenta p_i (considered here as incoming) and rank r can be written as

$$I_N^{D, \mu_1, \ldots, \mu_r}(a_1, \ldots, a_r; S) = \int \frac{\mathrm{d}^D k}{\mathrm{i}\pi^{D/2}} \frac{q_{a_1}^{\mu_1} \cdots q_{a_r}^{\mu_r}}{(q_1^2 - m_1^2 + \mathrm{i}\delta) \cdots (q_N^2 - m_N^2 + \mathrm{i}\delta)} \tag{7.1}$$

with the internal momenta $q_a = k + r_a$, the loop momentum k, the sum over the external loop momenta $r_a = \sum_{i=1}^a p_i$, and, for later use, the set of labels of internal parameters $S = \{1, \ldots, N\}$.

For the analytical calculation of one-loop integrals, it is useful to use their Lorentz structure and divide them into Lorentz tensors and (scalar) Feynman parameter

integrals [249, 250],

$$I_N^{D, \mu_1, \ldots, \mu_r}(a_1, \ldots, a_r; S) = (-1)^r \sum_{m=0}^{\lfloor \frac{r}{2} \rfloor} \left(-\frac{1}{2}\right)^m \sum_{j_1 \cdots j_{r-2m}}^{N} \left[(g^{\cdot\cdot})^{\otimes m} \Delta_{j_1 \cdot} \cdots \Delta_{j_{r-2m} \cdot}\right]_{\{a_1 \cdots a_r\}}^{\{\mu_1 \cdots \mu_r\}}$$
$$\cdot I_N^{D+2m, r-2m}(j_1, \ldots, j_{r-2m}; S), \quad (7.2)$$

with the shorthand notation $\left[(g^{\cdot\cdot})^{\otimes m} \Delta_{j_1 \cdot} \cdots \Delta_{j_{r-2m} \cdot}\right]_{\{a_1 \cdots a_r\}}^{\{\mu_1 \cdots \mu_r\}}$ for the sum over all ways [1] to distribute the Lorentz indices and momentum labels to the translation-invariant quantities

$$\Delta_{ij}^{\mu} = r_i^{\mu} - r_j^{\mu} = q_i^{\mu} - q_j^{\mu} \tag{7.3}$$

and m metric tensors $g^{\cdot\cdot}$. The translation invariance of Δ_{ij}^{μ} avoids additional terms during reduction when the loop momentum would otherwise need to be shifted to restore the original loop-integral form. $\lfloor \frac{r}{2} \rfloor$ stands for the rounded down integer $\frac{r}{2}$.

The Feynman parameter integrals used in Eq. (7.2) have their origin in the Feynman parametrization in which the product of the denominators $D_i = (q_i^2 - m_i^2 + i\delta)$ (cf. Eq. (7.1), p. 63) is combined into a single denominator by introducing Feynman parameters z_i,

$$\frac{1}{D_1 \cdots D_N} = (N-1)! \int_0^{\infty} dz_1 \cdots dz_N \frac{\delta(1 - \sum_{i=1}^{N} z_i)}{(z_1 D_1 + z_2 D_2 + \cdots + z_N D_N)^N}. \tag{7.4}$$

Combining all kinematic variables in the modified Cayley matrix $\mathcal{S}(S)$

$$\mathcal{S}_{ij}(S) = (r_i - r_j)^2 - m_i^2 - m_j^2, \tag{7.5}$$

and

$$R^2 = -\frac{1}{2}\left(\vec{z}\mathcal{S}\vec{z} - i\delta\right) = -\frac{1}{2} \sum_{i,k=1}^{N} z_i \mathcal{S}_{ik} z_k - i\delta, \tag{7.6}$$

the Feynman parameter integrals can be rewritten as integrals over Feynman para-

---

[1] For terms with metric tensors (higher-dimensional integrals), the distribution is not exhaustive, i. e. in each term of the sum only a subset of the momentum labels can be used.

meters $z_1 \cdots z_N$:

$$I_N^{D,r}(j_1, \ldots, j_r; S)$$

$$= (-1)^N \Gamma\left(N - \frac{D}{2}\right) \int \prod_{i=1}^{N} \mathrm{d}z_i \delta\left(1 - \sum_{k=1}^{N} z_k\right) z_{j_1} \cdots z_{j_r} (R^2)^{\frac{D}{2}-N}. \quad (7.7)$$

The various integral libraries usually implement form factors $A_{j_1 \cdots j_r}^{N,r}(S)$, $B_{j_1 \cdots j_{r-2}}^{N,r}(S)$, etc., which combine both the Feynman parameter integrals and their scalar pre-factors of Eq. (7.2), p. 64. Using these form factors, a general one-loop integral can be written as follows:

$$
\begin{aligned}
I_N^{D,\mu_1,\ldots,\mu_r}(a_1, \ldots, a_r; S) = &\sum_{j_1 \cdots j_r \in S} \left[\Delta_{j_1\cdot} \cdots \Delta_{j_r\cdot}\right]_{\{a_1 \cdots a_r\}}^{\{\mu_1 \cdots \mu_r\}} A_{j_1 \cdots j_r}^{N,r}(S) \\
&+ \sum_{j_1 \cdots j_{r-2} \in S} \left[g^{\cdot\cdot}\Delta_{j_1\cdot} \cdots \Delta_{j_{r-2}\cdot}\right]_{\{a_1 \cdots a_r\}}^{\{\mu_1 \cdots \mu_r\}} B_{j_1 \cdots j_{r-2}}^{N,r}(S) \\
&+ \sum_{j_1 \cdots j_{r-4} \in S} \left[g^{\cdot\cdot}g^{\cdot\cdot}\Delta_{j_1\cdot} \cdots \Delta_{j_{r-4}\cdot}\right]_{\{a_1 \cdots a_r\}}^{\{\mu_1 \cdots \mu_r\}} C_{j_1 \cdots j_{r-4}}^{N,r}(S) \quad (7.8) \\
&+ \sum_{j_1 \cdots j_{r-6} \in S} \left[g^{\cdot\cdot}g^{\cdot\cdot}g^{\cdot\cdot}\Delta_{j_1\cdot} \cdots \Delta_{j_{r-6}\cdot}\right]_{\{a_1 \cdots a_r\}}^{\{\mu_1 \cdots \mu_r\}} D_{j_1 \cdots j_{r-6}}^{N,r}(S) \\
&+ \cdots .
\end{aligned}
$$

7.2 Reduction method

The traditional reduction method of Passarino and Veltmann [251] reduces all tensor integrals to scalar integrals. Thereby, the inverse and determinant of the Gram matrix are needed. The Gram matrix $G^{(N-1)}$ is defined as product of the external momenta:

$$G_{ij}^{(N-1)} = 2r_i \cdot r_j, \quad i, j = 1 \ldots (N-1). \quad (7.9)$$

The traditional method is numerically unstable in case of small Gram determinants without any further steps (cf. [147, 252–259] for possible solutions, such as expansions in small Gram determinants, which are implemented e.g. in the integral library Collier [260]).

Numerical problems of small Gram determinants can be avoided by using higher-dimensional basis integrals or different reduction techniques (cf. [250, 261–267]).

The method presented here is the subtraction method [147], implemented in the tensor integral library Golem95C [3, 51, 52, 268]. The method is based on modified Cayley matrices rather than Gram matrices. In case of small inverse determinants, Golem95C switches automatically to numerical integration, which is based on a one-dimensional integrand representation that allows fast numerical integration.[2]

7.2.1 The scalar case

In the scalar case [249], the subtraction method functions as follows: The numerator is extended by adding and subtracting $\sum_{i \in S} b_i(S)(q_i^2 - m_i^2)$:

$$
\begin{aligned}
I_N^D(S) &= \int d\bar{k} \frac{1}{\prod_{j \in S}(q_j^2 - m_j^2 + i\delta)} \\
&= \int d\bar{k} \frac{1 - \sum i \in S b_i(S)(q_i^2 - m_i^2)}{\prod_{j \in S}(q_j^2 - m_j^2 + i\delta)} + \sum_{i \in S} \int d\bar{k} \frac{b_i(S)(q_i^2 - m_i^2)}{\prod_{j \in S}(q_j^2 - m_j^2 + i\delta)} \\
&= \int d\bar{k} \frac{1 - \sum_{i \in S} b_i(S)(q_i^2 - m_i^2)}{\prod_{j \in S}(q_j^2 - m_j^2 + i\delta)} + \sum_{i \in S} b_i(S) I_{N-1}^D(S \setminus \{i\}) \\
&=: I_{N,\,\mathrm{fin}}^D + I_{N,\,\mathrm{div}}^D
\end{aligned}
\tag{7.10}
$$

where the integral measure $\frac{d^D k}{i \pi^{D/2}}$ is abbreviated with $d\bar{k}$ and $S \setminus \{i\}$ is the set of internal parameters S without element i.

By choosing $b_i(S)$ as

$$
b_i(S) = \sum_{k \in S} \mathcal{S}_{ki}^{-1},
\tag{7.11}
$$

with $\mathcal{S}$ defined in Eq. (7.5), p. 64, the first term of Eq. (7.10) becomes infrared-finite and can be written as[3]:

$$
I_{N,\,\mathrm{fin}}^D = -B(S)(N - D - 1) I_N^{D+2}(S)
\tag{7.12}
$$

---

[2]The case of non-scalar massive four-point functions, where the numerical integration is not yet implemented, is discussed in Chapter 8, p. 75.

[3]Power counting shows that I_N^{D+2} is infrared-finite for $D = 4 - 2\epsilon$

with

$$B(S) = \sum_{i \in S} b_i(S) = \sum_{i,\,k \in S} \mathcal{S}_{ki}^{-1}. \tag{7.13}$$

The remaining term $I_{N,\,\text{div}}^D$ is still infrared divergent, but its integrals have one less leg. $\mathcal{S}^{-1}$ is the (pseudo-)inverse[4] of $\mathcal{S}$ which exists for $N \le 6$.

$B(S)$ is related with the Gram matrix by the relation [147]

$$B(S)\det\{\mathcal{S}(S)\} = (-1)^{N+1}\det G^{(N-1)}. \tag{7.14}$$

Combining Eq. (7.10) and Eq. (7.12), p. 66, a reduction formula for higher-dimensional scalar integrals can be derived:

$$I_N^{D+2}(S) = \frac{1}{B(S)}\frac{1}{D-N+1}\left(I_N^D(S) - \sum_{k \in S} b_k(S)\, I_{N-1}^D(S \setminus \{k\})\right). \tag{7.15}$$

Since the $\frac{1}{B(S)}$ factor in Eq. (7.15) re-introduces numerical problems if $B(S)$ tends towards zero, this reduction step should be avoided as far as possible by including higher-dimensional integrals into the set of master integrals [147].

However, due to the four-dimensional Minkowski space, there can be only four independent momenta. Therefore, the Gram matrix vanishes for $N \ge 6$, and hence $B(S) = 0$ and $I_{N \ge 6,\,\text{fin}}^D = 0$.[5]

For $N = 5$ and $D = 4-2\epsilon$, $B(S)$ generally does not vanish. However, since $D - N + 1 = -2\epsilon = \mathcal{O}(\epsilon)$ and I_5^{D+2} is UV and IR finite and has therefore no $\frac{1}{\epsilon}$-pole, the coefficients of I_5^{D+2} are also of $\mathcal{O}(\epsilon)$; hence the finite contribution of Eq. (7.10), p. 66 does not need to be calculated.

In these cases, the reduction formula simplifies to

$$I_N^D(S) = \sum_{i \in S} b_i(S)I_{N-1}^D(S \setminus \{i\}) + \mathcal{O}(\epsilon) \qquad \text{for } N \ge 5. \tag{7.16}$$

---

[4]The Moore-Penrose pseudo inverse needs to be used for exceptional kinematics. Alternatively, the inverse can be calculated from a pinched $\mathcal{S}$ matrix.

[5]The Gram matrix contains $N-1$ momenta. Due to momentum conservation, the omitted momentum is in all cases linear dependent.

7.2.2 The tensor case

By replacing $b_i(S)$ by tensors $C_{j a_1}^{\mu_1}$, the splitting in infrared-finite and simpler infrared-divergent integrals can be extended to tensor integrals,

$$
\begin{aligned}
I_N^{D,\mu_1,\ldots,\mu_r}(a_1,\ldots,a_r;S) = & \int \mathrm{d}\bar{k} \, \frac{\left(q_{a_1}^{\mu_1} + \sum_{j \in S} C_{j a_1}^{\mu_1}(q_j^2 - m_j^2)\right) q_{a_2}^{\mu_2} \cdots q_{a_r}^{\mu_r}}{\prod_{j=1}^N (q_j^2 - m_j^2 + \mathrm{i}\delta)} \\
& - \sum_{j \in S} \int \mathrm{d}\bar{k} \, \frac{C_{j a_1}^{\mu_1}(q_j^2 - m_j^2) q_{a_2}^{\mu_2} \cdots q_{a_r}^{\mu_r}}{\prod_{j=1}^N (q_j^2 - m_j^2 + \mathrm{i}\delta)} \\
=: & \; I_{N,\mathrm{fin}}^{D,\mu_1,\ldots,\mu_r} + I_{N,\mathrm{div}}^{D,\mu_1,\ldots,\mu_r}.
\end{aligned}
\tag{7.17}
$$

By choosing C_{ij}^{μ} to solve the equation

$$
\sum_{j \in S} \mathcal{S}_{kj} C_{jl}^{\mu} = \Delta_{kl}^{\mu},
\tag{7.18}
$$

i. e.

$$
C_{ij}^{\mu} = \sum_{k \in S} (\mathcal{S}^{-1})_{ik} \Delta_{kj}
\tag{7.19}
$$

with the (pseudo-)inverse $\mathcal{S}^{-1}$, one gets an infrared-finite expression $I_{N,\mathrm{fin}}^{D,\mu_1,\ldots,\mu_r}$.

For later use, we also define

$$
\mathcal{V}_a^{\mu} = \sum_{j \in S} C_{ja}^{\mu} = \sum_{k \in S} b_k \Delta_{ka}^{\mu}.
\tag{7.20}
$$

The infrared finite term $I_{N,\mathrm{fin}}$ can be expressed in terms of higher-dimensional integrals [49, 147]:

$$
\begin{aligned}
I_{N,\mathrm{fin}}^D(j_1,\ldots,j_r) = & -\sum_{k=2}^r \mathcal{S}_{j_1 j_k}^{-1} I_N^{D+2}(j_2 \ldots \hat{j}_k \ldots j_r; S) \\
& - \sum_{k=1} \mathcal{S}_{k,j_1}^{-1}(N - D - r) I_N^{D+2}(j_2,\ldots,j_r; S)
\end{aligned}
\tag{7.21}
$$

with $j_2 \ldots \hat{j}_k \ldots j_r = j_2 \ldots j_{k-1} j_{k+1} \ldots j_r$. This can be combined into a general reduc-

tion formula for tensor integrals:

$$
\begin{aligned}
I_N^D(j_1, \ldots, j_r; S) = & -\sum_{k=2}^{r} \mathcal{S}_{j_1 j_k}^{-1} I_N^{D+2}(j_2 \ldots \hat{j}_k \ldots j_r; S) \\
& - b(j_1, S) \cdot (N - D - r) I_N^{D+2}(j_2, \ldots, j_r; S) \\
& + \sum_{k \in S} \mathcal{S}_{j_1 k}^{-1} I_{N-1}^D(j_2 \ldots j_r; S \setminus \{k\}).
\end{aligned}
\tag{7.22}
$$

For five-point integrals, called pentagons, this formula can also be used, but indeed their reduction formula can be written without higher dimensional pentagon integrals *and* inverse Gram determinants (up to rank 5) [c.f. appendix C of 147]. Pentagons can be calculated as [147]:

$$
\begin{aligned}
I_5^{D, \mu_1 \cdots \mu_r}(a_1, \ldots, a_r; S) = \sum_{j \in S} \Bigg(& \Xi_{r-1} \left[\left(\frac{1}{2} b_j \mathcal{T}_{[4] a_{r-1} a_r}^{\mu_{r-1} \mu_r} - \mathcal{V}_{a_r}^{\mu_r} C_{j a_{r-1}}^{\mu_{r-1}} \right) Q_{2j}^{\mu_1 \cdots \mu_{r-2}} \right] \\
& - C_{j a_r}^{\mu_r} I_4^{D, \mu_1 \cdots \mu_{r-1}}(a_1, \ldots, a_{r-1}; S \setminus \{j\}) \Bigg) + \mathcal{O}(\epsilon)
\end{aligned}
\tag{7.23}
$$

where

$$
\mathcal{T}_{[4] a_1 a_2}^{\mu \nu} = g^{\mu \nu} + 2 \sum_{j \in S} C_{j a_1}^{\mu} \Delta_{j a_2}^{\nu}
\tag{7.24}
$$

and the relation

$$
\mathcal{T}_{[4] a_1 a_2}^{\mu \nu} = \frac{2}{B} \mathcal{V}_{a_1}^{\mu} \mathcal{V}_{a_2}^{\nu}
\tag{7.25}
$$

were used. $\mathcal{V}$ is defined in Eq. (7.20), p. 68. The values of the $Q_{2j}^{\mu_1 \cdots \mu_{r-2}}$ are listed in the appendix of [147]. They are zero for $r < 3$. For $r = 3$ and $r = 4$, they can be calculated as:

$$
Q_{2j}^{\mu_1} = (2 - D) \sum_{i \in S \setminus \{j\}} \Delta_{a_1 i}^{\mu_1} I_4^{n+2}(i; S \setminus \{j\})
\tag{7.26}
$$

$$
Q_{2j}^{\mu_1 \mu_2} = (1 - D) \left(g^{\mu_1 \mu_2} I_4^{n+4}(S \setminus \{j\}) + \sum_{i, k \in S \setminus \{j\}} \Delta_{a_1 i}^{\mu_1} \Delta_{a_2 k}^{\mu_2} I_4^{n+2}(i, k; S \setminus \{j\}) \right).
\tag{7.27}
$$

Ξ_{r-1} is a necessary symmetrization operator that averages all cyclic permutations of the pairs $(a_1, \mu_1) \ldots (a_{r-1}, \mu_{r-1})$ of an already in $r - 2$ first arguments identically

symmetrized tensor function. It can be defined recursively:

$$\Xi_{r-1}T^{\mu_1\cdots\mu_{r-1}}(a_1,\ldots,a_{r-1}) := \frac{1}{r-1}\Big(\Xi_{r-2}T^{\mu_1\cdots\mu_{r-1}}(a_1,\ldots,a_{r-1}) \tag{7.28}$$
$$+ \Xi_{r-2}T^{\mu_2\cdots\mu_{r-1}\mu_1}(a_2,\ldots,a_{r-1},a_1)$$
$$+ \cdots$$
$$+ \Xi_{r-2}T^{\mu_{r-1}\mu_1\cdots\mu_{r-2}}(a_{r-1},a_1,\ldots,a_{r-2})\Big)$$
$$\Xi_1 := id. \tag{7.29}$$

The $O(\epsilon)$ contributions can be neglected in phenomenological NLO calculations.

Similar to the scalar case, the reduction for integrals with $N \geq 6$ is trivial [147],

$$I_N^{D,\mu_1,\ldots,\mu_r}(a_1,\ldots,a_r;S) = -\sum_{j\in S} C_{ja_1}^{\mu_1} I_{N-1}^{D,\mu_2\cdots\mu_r}(a_2,\ldots,a_r;S\setminus\{j\}). \tag{7.30}$$

7.3 Higher rank pentagons and hexagons

Whereas for six-point integrals (hexagons) and above, i.e. for cases $N \geq 6$, the reduction formula can easily be extended to higher ranks (i.e. tensor integrals with rank r higher than the number of external legs N), special care has to be taken in the case of pentagons. The reason is that the rank-6 pentagon is UV divergent, in contrast to the lower rank pentagons as mentioned in the updated version of [147]. From the reduction point, therefore the higher-rank pentagons are the most complicated ones.

In the derivation of formula Eq. (7.23), p. 69 otherwise negligible $O(\epsilon)$-terms need to be considered. This leads to the extended reduction formula with an additional rational part:

$$I_5^{D,\mu_1\cdots\mu_6}(a_1,\ldots,a_6;S) = \sum_{j\in S}\Big(\Xi_5\left[\left(\frac{1}{2}b_j\mathcal{T}_{[4]a_5a_6}^{\mu_5\mu_6} - \mathcal{V}_{a_6}^{\mu_6}C_{ja_5}^{\mu_5}\right)Q_{2j}^{\mu_1\cdots\mu_4}\right]$$
$$-C_{ja_6}^{\mu_6}I_4^{D,\mu_1\cdots\mu_5}(a_1,\ldots,a_5;S\setminus\{j\})\Big) \tag{7.31}$$
$$+\frac{D-4}{960}\frac{1}{\epsilon}\sum_{j\in S}\sum_{i\in S\setminus\{j\}}\left[\frac{\mathcal{V}_\cdot}{B}\mathcal{D}_{j\cdot\cdot}^{\cdot\cdot}\left(g^{\cdot\cdot}\Delta_{i\cdot} + g^{\cdot\cdot}\Delta_{i\cdot} + g^{\cdot\cdot}\Delta_{i\cdot}\right)\right]_{a_1\cdots a_6}^{\mu_1\cdots\mu_6}$$

with

$$\mathcal{D}_{j\,a_1 a_2}^{\mu_1 \mu_2} = \left(b_j \mathcal{T}_{j\,a_1 a_2}^{\mu_1 \mu_2} - C_{ja_1}^{\mu_1} \mathcal{V}_{a_2}^{\mu_2} - C_{ja_2}^{\mu_2} \mathcal{V}_{a_1}^{\mu_1} \right) \tag{7.32}$$

and

$$\begin{aligned}
Q_{2j}^{\mu_1 \cdots \mu_4} = (-1-D)\Bigg(& \frac{1}{4} \left(g^{\mu_1 \mu_2} g^{\mu_3 \mu_4} + g^{\mu_1 \mu_3} g^{\mu_1 \mu_4} + g^{\mu_1 \mu_4} g^{\mu_2 \mu_3} \right) I_4^{D+6}(S \setminus \{j\}) \\
& -\frac{1}{2} \sum_{i_1, i_2 \in S \setminus \{j\}} \left(g^{\mu_1 \mu_2} \Delta_{a_3 i_1}^{\mu_3} \Delta_{a_4 i_2}^{\mu_4} + g^{\mu_1 \mu_3} \Delta_{a_2 i_1}^{\mu_2} \Delta_{a_4 i_2}^{\mu_4} + \right. \\
& \quad g^{\mu_2 \mu_3} \Delta_{a_1 i_1}^{\mu_1} \Delta_{a_4 i_2}^{\mu_4} + g^{\mu_1 \mu_4} \Delta_{a_2 i_1}^{\mu_2} \Delta_{a_3 i_2}^{\mu_3} + g^{\mu_2 \mu_4} \Delta_{a_1 i_1}^{\mu_1} \Delta_{a_3 i_2}^{\mu_3} \\
& \quad \left. + g^{\mu_3 \mu_4} \Delta_{a_1 i_1}^{\mu_1} \Delta_{a_2 i_2}^{\mu_2} \right) I_4^{D+4}(i_1, i_2; S \setminus \{j\}) \\
& + \sum_{i_1 \cdots i_4 \in S \setminus \{j\}} \Delta_{a_1 i_1}^{\mu_1} \Delta_{a_2 i_2}^{\mu_2} \Delta_{a_3 i_3}^{\mu_3} \Delta_{a_4 i_4}^{\mu_4} I_4^{D+2}(i_1, \ldots, i_4; S \setminus \{j\}) \Bigg).
\end{aligned} \tag{7.33}$$

The corresponding form factors (cf. Eq. (7.8), p. 65) to Eq. (7.31) are listed in Appendix A, p. 121.

The reduction of higher rank hexagons can be performed using Eq. (7.30), p. 70.

7.4 Implementation in Golem95C

The form factor for the higher rank pentagons Eqs. (A.1) to (A.9) (pp. 121–123) and hexagons has been implemented in Golem95C in a generic way[6] [3]. The implemented method can thus, in principle, be extended easily to higher ranks (rank-7 pentagons etc.).

The general formula has been checked by consistency checks. These use contracted integrals that can be simplified by hand or FORM programs to known integrals, but can also be evaluated directly with the form factors that should be tested.

For illustration, a simple example of a consistency check is presented. In the following, testing the triangle form factors of a massless triangle ($N = 3$, $m_{1,2,3} = 0$, four-dimensional external legs and without loss of generality (w.l.o.g.) $r_3 = 0$) with scalar bubble form factors ($N = 2$) is shown. For simplicity, it is also assumed that the first

---

[6]Except the symmetry factors for the pentagons that are listed in Appendix A, p. 121 for rank-6 and need to be explicitly implemented for higher ranks (e.g. rank-7 pentagons).

incoming momentum is on-shell ($r_1^2 = 0$). By contracting the integral with $r_{1\mu}$, one gets:

$$r_{1\mu} \int \mathrm{d}\bar{k} \frac{q_1^\mu}{((k+r_1)^2 + \mathrm{i}\delta)((k+r_2)^2 + \mathrm{i}\delta)((k+r_3)^2 + \mathrm{i}\delta)}$$
$$= r_{1\mu} \left(\Delta_{12}^\mu A_2^{3,1}(S) + \Delta_{13}^\mu A_3^{3,1}(S) \right)$$
$$= (r_1 \cdot r_2) A_2^{31}(S) \tag{7.34}$$

On the other hand, the following formulas can be applied to reduce the integral:

$$r_1^\mu = (q_1 - q_3)^\mu, \tag{7.35}$$

$$q_i \cdot q_3 = \frac{1}{2} \left(q_1^2 + q_i^2 - r_i^2 \right). \tag{7.36}$$

Abbreviating $\left((k+r_i)^2 + \mathrm{i}\delta \right) = D_i$, yields:

$$r_{1\mu} \int \mathrm{d}\bar{k} \frac{q_1^\mu}{((k+r_1)^2 + \mathrm{i}\delta)((k+r_2)^2 + \mathrm{i}\delta)((k+r_3)^2 + \mathrm{i}\delta)}$$
$$= \int \mathrm{d}\bar{k} \frac{r_1 \cdot q_1}{D_1 D_2 D_3} = \int \mathrm{d}\bar{k} \frac{(q_1 - q_3) \cdot q_1}{D_1 D_2 D_3}$$
$$= \int \mathrm{d}\bar{k} \frac{q_1^2 - \frac{1}{2} \left(q_1^2 + q_3^2 - r_1^2 \right)}{D_1 D_2 D_3} = \int \mathrm{d}\bar{k} \frac{\frac{1}{2} D_1 - \frac{1}{2} D_2}{D_1 D_2 D_3}$$
$$= \int \mathrm{d}\bar{k} \left(\frac{1}{2} \frac{1}{D_2 D_3} - \frac{1}{2} \frac{1}{D_1 D_3} \right)$$
$$= \frac{1}{2} I_2(S \setminus \{1\}) - \frac{1}{2} I_2(S \setminus \{2\}) \tag{7.37}$$

Both reductions should yield the same result. Special attention has to be taken in the ($D \neq 4$)-dimensional kinematic.

Beside internal consistency checks, the results were also cross-checked with the implementation of rank $N + 1$ integrals in the XSamurai extension [54] of Samurai [53].

For the usage with GoSam, the tensorial reconstruction interface [227] of Golem95C was extended to rank $N + 1$. Both consider now the additional rational terms of Eq. (7.31), p. 70.

At the matrix-element level, the implementation was also successfully compared with Ninja [55] in several processes, e.g. Higgs + multiple jet calculations. In Ref. [269], the

high (or at least sufficient) accuracy of Golem95C results is shown compared to other reduction programs even in the case of more complicated processes with higher-rank pentagons.

8 Numerical box diagrams in Golem95C

For special kinematics, especially for small determinants of the modified Cayley matrix (Eq. (7.5), p. 64), the reduction method introduced in Section 7.2 could fail for reason of numerical instability. Such special cases are either directly implemented in Golem95C, calculated at runtime by numerical integration methods or by calls of third-party libraries.

For up to three-point functions, the stability has been studied and confirmed in [248], especially for vanishing determinants of the Gram and/or S matrix.

Still, for non-scalar massive four-point functions (boxes), all limits have not yet been implemented, so that the result of Golem95C can become unstable in certain limits. This special box kinematic scenarios appear especially in the reduction of pentagons and hexagons with internal masses.

A one-dimensional integrand representation is still an unsolved problem in the case of general massive boxes (for three-point integrals they are listed in Ref. [268]), but would allow easy and fast numerical integration. Instead, another approach to solve this issue is discussed in this chapter.

The concept is to change completely to numerical integration of these boxes. As these integrals include infrared and collinear singularities, this is not trivial, but need special treatment.

This treatment has been implemented in SecDec [270–273], a program which isolates these singularities by sector decomposition and allows therefore to integrate them by Monte-Carlo techniques.

For the (at least in the scalar case) divergent box integrals, listed as No. 6–16 in [228] and on the QCDLoop homepage[1] and, in addition, for seven generic, non-divergent boxes[2] with at least one massive leg, SecDec was called. In each case, all possible (sorted) Feynman-parameter combinations in the numerator were generated from

---

[1]`http://qcdloop.fnal.gov`.

[2]The cases are 4 masses; 3 masses; 2 masses adjacent with one on-shell, 2 masses adjacent; 2 masses opposite with one on-shell; 2 masses opposite, one massive internal leg.

rank-1 to rank-4. To date, only the case of real masses has been considered, although an extension to complex masses would function similarly.

As required by the implemented form factors for boxes, pentagons and hexagons in Golem95C, rank-1 to rank-3 six-dimensional boxes, and rank-1 eight-dimensional boxes were also generated.

In total, SecDec was called for 2115 different cases. Since some of the resulting integrals have single and double poles, 2330 expressions were finally handled.

The output of SecDec (C++ code) for the various cases was transformed into an internal library for Golem95C. In the case of small $B(S)$ values (cf. Eq. (7.14), p. 67), which corresponds to the exceptional kinematic cases, the SecDec-generated integrals are called automatically.

For multi-dimensional numerical integration, the Divonne algorithm from the CUBA library [274] is used. This library implements also other numerical integral algorithms. Beside the CUBA library, which could be integrated seamlessly in the Golem95C build system, no further dependency has been introduced. In particular, no extra call of the SecDec program itself is needed.

Two scenarios are used for testing the introduced integrals, described in Ref. [275]. The scenarios contain box integrals in exceptional phase-space regions that result from the reduction of hexagons and pentagons respectively (i.e. 6/5-point loop integrals). For the first case with $\det G \to 0$, form factors of the box integral with following properties are calculated:

$$m_1 = m_3 = m_4 = 0 \qquad\qquad m_2 = 91.1876 \,\text{GeV}$$
$$s = 2 \times 10^4 \,\text{GeV}^2 \qquad\qquad t = -4 \times 10^4 \,\text{GeV}^2$$
$$p_1^2 = 1 \times 10^4 \,\text{GeV}^2 \qquad\qquad p_2^2 = p_3^2 = 0$$
$$p_4^2 = \left(-6 \times 10^4 \,\text{GeV}^2\right)(1+x)$$

The result is shown in Fig. 8.1. Here, the critical limit $x \to 0$ is plotted of the form factors A41 $(= A_1^{4,1}$ of Eq. (7.8), p. 65), A42 $(= A_{11}^{4,2})$ and A44 $(= A_{1111}^{4,4})$ for the current version of Golem95C and the SecDec-improved version. It can be seen that for the A42 form factor, the current version of Golem95C is unstable in this limit, whereas the SecDec-improved version remains stable. For A41, the call of the SecDec-integrals would not be needed.

In the second case, the behaviour in the limit of a vanishing modified Cayley matrix determinant ($\det S \to 0$) and simultaneous vanishing Gram determinant ($\det G \to 0$)
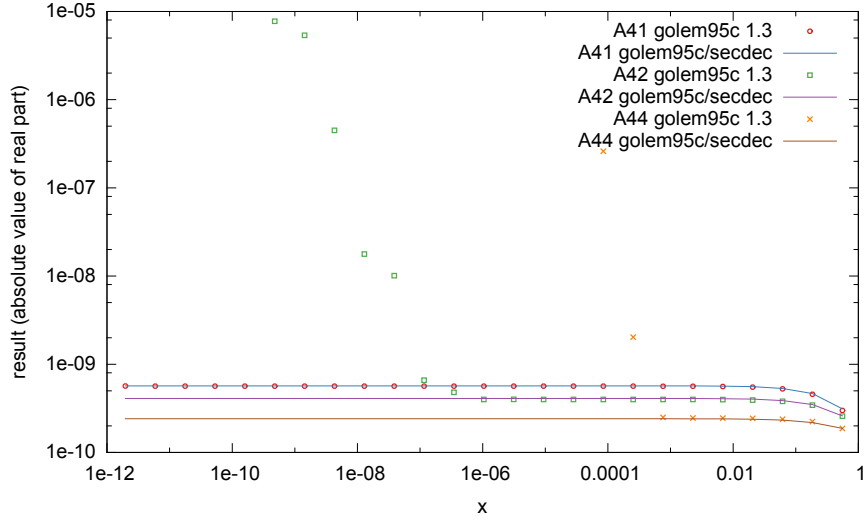
Figure 8.1: Stability test (I) for massive boxes in Golem95C. Whereas in the critical limit of a vanishing Gram determinant (here parametrized by $x \to 0$), the rank-1 form factor A41 is stable, the rank-2 form factor A42 and rank-4 A44 form-factor grow uncontrolled due to numerical instabilities. The integrals from SecDec remain both stable and give the same results (up to numerical errors from the integration).

are analyzed. The box integral used is defined as follows

$$m_1 = m_3 = 0 \qquad\qquad m_2 = 0.066\,\text{GeV} \qquad\qquad m_4 = 91.1876\,\text{GeV}$$

$$s = 6.4 \times 10^3\,\text{GeV}^2(1 + x) \qquad t = 4 \times 10^4\,\text{GeV}^2(1 + x)$$

$$p_1^2 = 4 \times 10^4\,\text{GeV}^2 \qquad\qquad p_2^2 = (0.066\,\text{GeV})^2 \qquad\qquad p_3^2 = 6.4 \times 10^3\,\text{GeV}^2 \quad p_4^2 = 0.$$

As in the first example, the exceptional kinematic appears at the limit $x \to 0$. The result is shown in Fig. 8.2. Here, the form factors from the existing Golem95C version show again unstable behaviour at the exceptional limit, whereas in the SecDec-improved versions, they remain stable. The numerical integration for the form factor A43 ($= A_{111}^{4,3}$) shows some minor fluctuations.

In both examples, the SecDec-improved code yielded reasonable results, i.e. the numerical integrals yielded the same (or due to numerical integrations very similar) results as the already implemented integrals near the exceptional cases, but showed no numerical instabilities at the limits. However, the runtime in both examples increased by about a factor of 1000–2000 if the SecDec-improved integrals were used (the exact factor depends very much on the precision settings of the numerical integration with CUBA and the involved kinematic and form-factors).
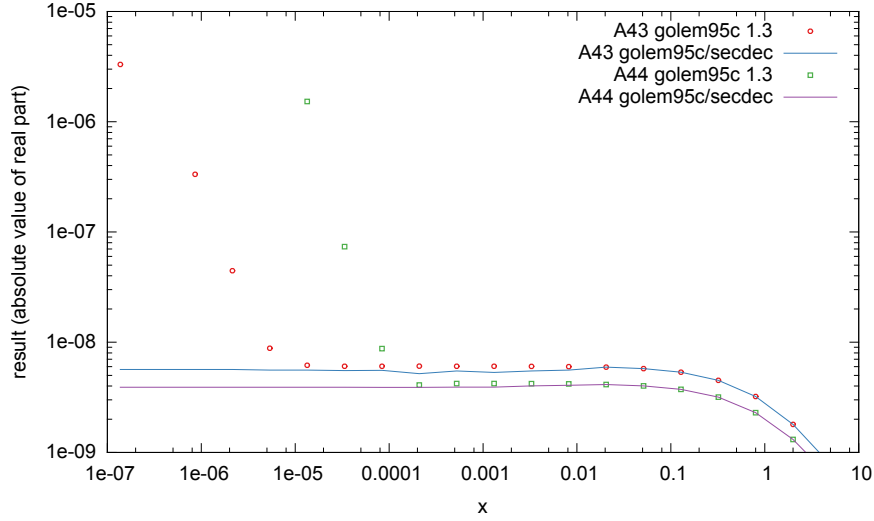
Figure 8.2: Stability test (II) for massive boxes in Golem95C. The critical limit of a vanishing modified Cayley and Gram determinant (here parametrized by $x \to 0$) is analyzed for the rank-3 form factor A43 and rank-4 A44 form-factor. In opposite to the existing Golem95C implementation, the form factors from the SecDec-improved Golem95C version remain both stable.

In combination with GoSam, which calls large numbers of form factors for one phase space point through the tensor-reconstruction interface [227], the runtime is unfortunately no longer practical (seconds to minute range), especially when the requested precision from the numerical integrations is set to appropriate values.

Due to the very slow runtime and the big code size, the change could not yet included in the official Golem95C version.

As SecDec can only generate integrals for a fixed kinematic, and the generated integrals are finally used for all similar configuration cases, it remains uncertain whether the chosen configurations cover all needed cases. As the generated integrals fail, if they are called with invalid kinematic, this issue can, however, be easily detected and fixed by adding further special configurations.

In general, there is a trade-off between time spent on calculating unstable points and calculating (large numbers) of other stable points nearby. For the one-loop parts of NNLO calculations, however, exceptional kinematic cases are more important and cannot be avoided, so that the extension might still find application in the future.

Part III

Phenomenological applications

9 $pp/gg\,(\to W^+W^-)\to e^+\nu_e\,\mu^-\bar{\nu}_\mu$ with anomalous couplings

In this chapter, the previously discussed tools, especially GoSam 2.0 and Herwig 7, linked by BLHA2, are applied to calculate the process $pp\,(\to W^+W^-)\to e^+\nu_e\,\mu^-\bar{\nu}_\mu$ at NLO in the QCD coupling, including and focusing on the loop-induced production process from the gluon-gluon (gg) channel enhanced by anomalous $ggWW$ couplings stemming from the general EFT operators that contribute at the lowest possible dimension eight.

The calculation performed does not involve higher-rank tensor integrals[1], but calculating for example QCD-corrections to the dimension-8 operators contributions would require rank-4 two-point integrals (bubbles) and rank-6 three-point integrals (triangles).

Most results shown in this chapter at LHC energies were recently published in Ref. [1]. The author of this thesis was mainly involved in the preparing, testing and extending GoSam including its interface to the Monte-Carlo event generator Herwig and the model file used for this calculation, testing the developments and modifications applied to Herwig, re-writing and improving the analysis code used, performing the actual runs and, finally, compiling the results into the plots shown.

9.1 Motivation

Due to an excess in the diboson measurements of the ATLAS [276, 277] and CMS [278, 279] experiments, the diboson channel was paid extra attention. The excess was especially visible in the hadronic decay channel. In the first 13 TeV data presented in December 2015, the excess was no longer visible, but could not yet statistically fully excluded. Various theories have been considered to explain the excess, for example

---

[1]An application of higher rank integrals can be found in Ref. [4], where NLO QCD corrections to diphoton plus jet production through graviton exchange in a large extra dimensional model are calculated.

by introducing new particles, s-channel resonances, strongly coupled dynamics, such as composite Higgs models, extended gauge groups like Z' or W' and multiple ways to extended Higgs sector. A summary with references to the various theoretical explanations can be found in [280].

In addition to this excess, the diboson process is also an important background to the Higgs boson decay $H \to WW$ as well as in the search of unknown reasons of missing energy, which could be a hint for several BSM models. It allows precision measurements and predictions of the electroweak symmetry breaking.

Furthermore, there were differences between phenomenological calculations and experiments observed at the total cross section level, but also in differential observables. This matter requires for further precision calculations, also involving BSM effects.

In the following sections, the current experimental and phenomenological aspects are summarized before a new calculation for $pp\,(\to W^+W^-) \to e^+\nu_e\,\mu^-\bar{\nu}_\mu$ is presented including anomalous couplings that enlarge the gg channel. The effects of parton showering and top mass effects are also examined. In the second step, the calculation is extended to the center-of-mass energy of 100 TeV for future proton-proton colliders beyond the LHC.

9.1.1 Experimental measurements

Several measurements at the LHC and previous colliders have determined the diboson rate.

The results at a center-of-mass energy of 7 TeV at the LHC were published in [86, 281, 282], later the 8 TeV results were added [283–285]. These measured total inclusive cross sections showed some tensions to theoretical predictions at NLO as mentioned in the next sections. Experimental results for the here analyzed final state at 13 TeV are not yet published. First searches for diboson resonances in the $lvqq$ and $llqq$ final state can be found in [286–288]. Results for ZZ production at 13 TeV, which would also be affected by the anomalous couplings analyzed, can be found in Refs. [289, 290].

As mentioned before, the $WW \to e^+\nu_e\,\mu^-\bar{\nu}_\mu$ channel is also important for Higgs physics. In Ref. [291], it was used to determine the spin and parity of the Higgs boson.

Earlier searches for anomalous couplings have been performed by the DØ collaboration [292, 293].

9.1.2 Existing calculations

Since the first $q\bar{q} \rightarrow W^+W^-$ NLO calculations in the 1990s [58–60] with on-shell W-bosons, there have been multiple efforts to improve the calculation. Helicity amplitudes including decay to leptons have been provided in [61] and were later used in [62] to study anomalous couplings. A matching procedure to parton shower was applied in MC@NLO [172] and in MadGraph5_aMC@NLO [63, 294].

From the beginning, the calculations were driven by the Higgs boson search which needed a precise possible background estimation to the $H \rightarrow W^+W^- \rightarrow l\nu_l l^{(')}\nu_{l^{(')}}$ decay. After the Higgs boson was found, this process is still of interest as it allows to measure the Higgs boson width. This can be performed by examining the off-shell production and decay as proposed and studied in [295–302]. From the ZZ final state, the Higgs boson width could already be constrained [303].

The first estimations to the loop-induced, $gg \rightarrow W^+W^-$ cross section with on-shell W-bosons come from $gg \rightarrow ZZ$ calculations [64–66]. Ref. [67] included the leptonic decays of the W-bosons for massless fermions. In Ref. [68], this calculation was extended by considering also massive top- and bottom-quarks.

Recent results of the full SM process including shower, contributions from the gg-channel and up to one merged additional jet can be found in [69].

The outcome of MCFM NLO-calculations, including the gluon-gluon-initial channel [70–72] were up to 20 % lower in the leptonic decay than the LHC measurements. NNLO calculations [73] lowered this gap.

Two-loop calculations showed a K-Factor of 1.2 – 1.6 depending on the scale choice from the loop-induced gg initial channel (gg LO) to the two-loop result (gg NLO) at 13 TeV. As the gg-channel is still loop-suppressed, the total cross section (pp) increases by only 2 %. [74]

Two-loop code for the qq and gg initial state and four-lepton final state has been published in the VVamp project [304, 305].

Further studies [75–79] have shown that large logarithms from jet veto conditions cannot be ignored and that including these, discrepancies to experimental data appear only at the 1σ level if the fiducial cross section is analyzed, i.e. the region where the detectors are most sensitive. The extrapolation method to the final cross section thus need to be reconsidered [78].

A discussion about the a-priori underestimated uncertainty from scale variation in diboson production at LO can be found in [306].

The p_T distribution of W^+W^- has been calculated at NNLL+NNLO (next-to-next-to-leading-log combined with next-to-next-to-leading order fixed order calculation) in [307].

Electroweak-corrections were calculated in [80, 81, 308]; subleading processes to W^+W^- production like $\gamma\gamma \to W^+W^-$ are studied in [309]

The case of an additional jet state, i.e. the process $pp \to W^+W^-$+ jet, has been calculated in [310–312] at NLO in QCD. In Ref. [313], electroweak corrections were added. The loop-induced process $gg \to W^+W^-$+ jet, which was neglected in those studies, is studied in [314].

The effects of large extra-dimensions in the ADD model [57] on W^+W^- have been analysed in [315]. The extra-dimensions enhance the invariant mass distribution tail of the diboson system similar to the dimension-8 operators discussed here.

For the process $pp \to l^+l^-$, the effect of dimension-eight operators introducing ggl^+l^- couplings was analyzed in [316]. For the final state analyzed in this thesis with different lepton flavours, these operators do not contribute at the perturbation order considered. WWZ and $WW\gamma$ dimension-six operators that contribute to the $e^+\nu_e\,\mu^-\bar{\nu}_\mu$ final state were analyzed in [134] in a narrow-width approximation. Possible operators of dimension six and higher are classified and enumerated in [317–322]. Ref. [323] notes that dimension-eight operators could be more important than dimension-six operators in certain circumstances, in particular, for example, if dimension-six operators are loop-suppressed in the full theory, but dimension-eight operators are created at tree-level.

9.2 Effective model: dimension–8 operators

The speciality of the gluon-gluon channel is that the first possible operators, mediating directly between the four bosons, occur at dimension eight and are therefore suppressed by four powers of the effective scale Λ. There are multiple other operators already at dimension six, which would also contribute to this channel, such as effective Higgs boson couplings to vector boson pair or two gluons, or triple and quartic gauge couplings [317, 318, 324]. They have been discussed already extensively in the literature, mainly in vector-boson-fusion, and are constrained by several measurements (cf. e.g. [82–88]) and are, therefore, not considered here.

Furthermore, interference effects and cancellations can hide these operators partially, so that BSM effects, which can be described by them, are more difficult to find.

There are three different types of the dim-8 operators, one CP-even and two CP-odd,

$$O_1 = \frac{c_1}{\Lambda^4} G^a_{\mu\nu} G^{a,\mu\nu} W^I_{\rho\sigma} W^{I,\rho\sigma} \tag{9.1}$$

$$O_2 = \frac{c_2}{\Lambda^4} \tilde{G}^a_{\mu\nu} G^{a,\mu\nu} W^I_{\rho\sigma} W^{I,\rho\sigma} \tag{9.2}$$

$$O_3 = \frac{c_3}{\Lambda^4} G^a_{\mu\nu} G^{a,\mu\nu} \tilde{W}^I_{\rho\sigma} W^{I,\rho\sigma} \tag{9.3}$$

where

$$G^a_{\mu\nu} = \partial_\mu G^a_\nu - G\partial_\nu G^a_\mu - g_s f_{abc} G^b_\mu G^c_\nu \tag{9.4}$$

$$\tilde{G}^a_{\mu\nu} = \frac{1}{2}\varepsilon^{\mu\nu\rho\sigma} G^a_{\rho\sigma} \tag{9.5}$$

is the gluonic field strength tensor, respectively its dual tensor, and

$$W^I_{\mu\nu} = \partial_\mu W^I_\nu - \partial_\nu W^I_\mu - g\varepsilon^{IJK} W^J_\mu W^K_\nu \tag{9.6}$$

$$\tilde{W}^I_{\mu\nu} = \frac{1}{2}\varepsilon^{\mu\nu\rho\sigma} W^I_{\rho\sigma} \tag{9.7}$$

with the SU(2) fields W^I. These fields can be written in the physical field basis:

$$W^1_\mu = \frac{1}{\sqrt{2}}(W^+_\mu + W^-_\mu) \tag{9.8}$$

$$W^2_\mu = \frac{i}{\sqrt{2}}(W^+_\mu + W^-_\mu) \tag{9.9}$$

$$W^3_\mu = Z_\mu \cos\theta_w + A_\mu \sin\theta_w \tag{9.10}$$

The resulting Feynman-rules for new $ggWW$ vertices that are introduced by the operators Eqs. (9.1) to (9.3) are listed in Appendix B, p. 125. The operators are orthogonal, i.e. they do not interfere with each other.

In the following, the coefficients c_1, c_2 and c_3 are often set to the same value and therefore they are abbreviated with c_i ($i = 1\ldots3$).

For the gg cross section analyzed, interference terms between the loop-induced SM calculation and the dimension-8 operators are included as follows:

$$\sigma_{ggWW,\texttt{gg\_All}} \sim \left|\mathcal{M}^{\text{1-loop}}_{\text{SM}}\right|^2 + 2\,\text{Re}\left(\mathcal{M}^{\text{1-loop}}_{\text{SM}}\mathcal{M}^*_{\text{dim-8 op}}\right) + \left|\mathcal{M}_{\text{dim-8 op}}\right|^2 \tag{9.11}$$
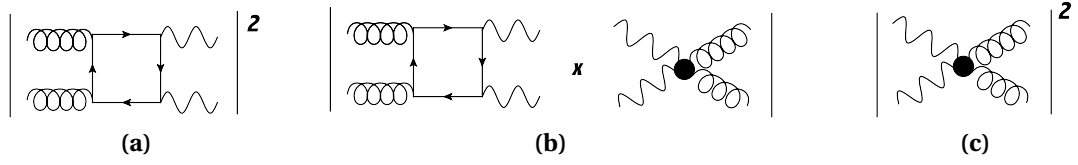
Figure 9.1: This diagram visualizes the contributions included in `gg_All` (cf. Eq. (9.11)) [1]. (a): The squared loop-induced SM contribution. (b): The interference term. (c): The squared dim-8 operator.

9.3 Setup and input parameters

Only the purely leptonic decays of the *W*-bosons in two different lepton flavours are considered, i.e. the process $pp \to e^+ \nu_e \, \mu^- \bar{\nu}_\mu$. It is calculated at a center-of-mass energy of 8 TeV and 13 TeV.

The same flavour final state $pp \to W^+ W^- \to l^+ \nu_l \, l^- \bar{\nu}_l$ would need to be combined with non-resonant contributions such as $ZZ \to l^+ \nu_l \, l^- \bar{\nu}_l$ and is therefore not considered here.

The quarks and leptons of the first two generations are considered as massless, the third generation as massive. Accordingly, a diagonal CKM matrix is assumed.

The loop-induced SM contribution (*gg* initial state) contains only triangle diagrams with internal Higgs boson exchange and box diagrams. The other possible single- and double-resonant triangle diagrams, which are important for gauge invariance, cancel each other; photon exchange diagrams also vanishes due to Furry's theorem [325]. The Feynman diagrams are listed in Appendix C.1, p. 127. [66]

For the SM background (*qq* and *qg* initial state), all possible diagrams are considered with the $e^+ \nu_e \, \mu^- \bar{\nu}_\mu$ final state at the NLO in the QCD coupling constant including single- and double-resonant diagrams. The Born and virtual diagrams are listed in Appendix C.2, p. 128 for the $u\bar{u}$ channel.

For the parton distribution functions, MMHT2014nlo68cl_nf4 [326] is used. Accordingly, four (massless) quark flavours are assumed in the initial state (i.e. a four-flavour scheme). The parton distribution function is accessed using the library LHAPDF 6.1.5 [327].

The default renormalization and factorization scale are set to the same value. Two choices are made. Either a fixed scale $\mu_R = \mu_F = m_W$ is chosen or a dynamic scale at

the invariant mass of the WW-pair

$$\mu_R = \mu_F = m_{WW} = \sqrt{\left(p_{e^+} + p_{\nu_e} + p_{\mu^-} + p_{\bar{\nu}_\mu}\right)^2}. \tag{9.12}$$

All QCD renormalization procedures needed are automatically applied by GoSam. GoSam uses the $\overline{MS}$-scheme to renormalize the strong coupling. For massive quarks, subtraction at zero momentum is employed (cf. [50]). For the SM background calculated at NLO QCD, only α_s renormalization is required. The massive quark loops of the loop-induced gluon-gluon channel are UV-finite.

The dimension-8 operators (cf. Eqs. (9.1) to (9.3), p. 85) depend linearly on the $\frac{c_{i=1,2,3}}{\Lambda^4}$ ratios. Where not otherwise noted, $\frac{c_i}{\Lambda^4} = \frac{0.1}{(1\,\text{TeV})^4}$ is chosen. This choice prevents unphysical results already at lower energies (cf. the discussion in Section 9.8, p. 107).

If the choice $c_i = 1$ appears more natural, identical results can be obtained by the corresponding scale $\Lambda \approx 1.778\,\text{TeV}$.

Further settings of parameters are listed in Table 9.1. The non-listed electroweak parameters are derived from the set (α_{EW}, G_F, M_Z) of input parameters according to Eqs. (6.1) and (6.2), p. 60.

Several cuts were applied (cf. Table 9.2) at generator level (mainly to exclude unstable and divergent phase space regions) and at analysis level (to model experimental W-identification cuts).

This splitting allows further analysis of the cut effects, as a second analysis was also carried out without any additional cuts (in the following named *generator-level analysis*).

9.4 Computational setup: Herwig and GoSam

The computation is performed by using the Monte-Carlo event generator Herwig 7 (also known as Herwig++ 3) [182] and GoSam, which provides the tree- and one-loop amplitudes.[2]

The workflow is controlled by Herwig, which requests the amplitudes needed from GoSam, combines them properly and finally provides weighted events than can

---

[2]For the *gg* sub-process, the BLHA2 order file generated by Herwig 7 and the GoSam input card are listed in Appendix D, p. 133.

Fermi coupling constant	G_F	$1.166\,37 \times 10^{-5}\,\mathrm{GeV}^{-2}$
fine-structure constant	α_{EW}	$\frac{1}{128.91}$
b mass	m_b	$4.2\,\mathrm{GeV}$
top mass	m_t	$174.2\,\mathrm{GeV}$
top width	Γ_t	$1.4\,\mathrm{GeV}$
Higgs boson mass	m_h	$125.7\,\mathrm{GeV}$
Higgs boson width	Γ_h	$4.11\,\mathrm{MeV}$
W width	Γ_W	$2.085\,\mathrm{GeV}$
Z mass	m_Z	$91.1876\,\mathrm{GeV}$
Z width	Γ_Z	$2.4952\,\mathrm{GeV}$
dim-8 operator strengths	$c_{i=1,2,3}$	0.1
effective scale	Λ	$1\,\mathrm{TeV}$
CKM-Matrix	V_{UD}	$\mathrm{diag}(1,1,1)$

Table 9.1: Input parameters for the calculation (where not otherwise noted).

Generator cuts[a]	
invariant mass of same-flavour lepton-neutrino pair	$50\,\mathrm{GeV} \leq m_{l\nu_l} \leq 150\,\mathrm{GeV}$
transverse momentum of same-flavour lepton-neutrino pair	$p_{T,l\nu_l} \geq 10\,\mathrm{GeV}$
rapidity[b] of charged leptons	$|y_l| \leq 3.5$
lepton transverse momentum	$p_{T,l} \geq 15\,\mathrm{GeV}$
missing transverse momentum (vector-summed)	$\displaystyle{\not}p_T \geq 15\,\mathrm{GeV}$
Analysis cuts	
invariant mass of same-flavour lepton-neutrino pair	$60\,\mathrm{GeV} \leq m_{l\nu_l} \leq 100\,\mathrm{GeV}$
pseudo-rapidity[b] of charged leptons	$|\eta_l| \leq 3$
transverse energy of charged leptons	$p_{T,l} \geq 25\,\mathrm{GeV}$
missing transverse momentum (vector-summed)	$\displaystyle{\not}p_T \geq 25\,\mathrm{GeV}$

[a] The cuts are slightly smeared-out in the Herwig default setup. Also here, the default values `FuzzyTheta:EnergyWidth 4.0*GeV` and `FuzzyTheta:RapidityWidth 0.4` are used.

[b] Since leptons are considered as massless, there is no difference between rapidity and pseudo-rapidity.

Table 9.2: Applied cuts at generator and analysis level.

be further analyzed. For the NLO setup used for the SM background, Herwig 7 composes automatically Catani-Seymour subtraction terms [123] from the color-correlated matrix elements provided by GoSam.

The generator cuts are applied in Herwig at generator level, i.e. at the Monte-Carlo event generation. The analysis cuts are later added by the analysis code.

The complex mass scheme [328] is used and, therefore, a non-zero top-width (cf. Table 9.1, p. 88).

For this application, Herwig 7 is extended by custom patches to support the combination of loop-induced SM diagrams and corresponding tree-level BSM diagrams including interference effects.

The matrix elements of all diagrams are calculated by GoSam, including real radiation diagrams, colour-correlated diagrams and the diagrams of the dimension-8 operators which have a different power in α_s in comparison to the loop-induced diagrams.

In contrast to normal calculations, in which Herwig knows all diagrams including their exact coupling constant powers and can therefore pass a fixed value of the QCD coupling constant α_s to the tree/loop-provider and re-normalizes afterwards with the correct value of α_s, the α_s handling is changed. An option was developed and is used, which passes immediately the correct value of α_s to GoSam and avoids any later adjustment that would require the knowledge of the correct power.

For the interference term, the normal NLO-setup is used in GoSam as the matrix element corresponds to a Born amplitude (in our case the tree-like BSM term with the effective operator) multiplied by a virtual 1-loop-amplitude (in this case the loop-induced gluon-gluon SM part). Only the precision checks of loop-induced processes (cf. Section 5.4, p. 49) must be switched on.

Finally, the generated events are directly forwarded by Herwig to the program package Rivet 2.4 [246] and analysed, i.e. the distributions of various observables, which are shown below in the result sections, are deduced from the properties of the generated events (such as their probability and kinematic). Thereby, the analysis cuts (cf. Table 9.1, p. 88) are applied. The *W*-bosons are reconstructed from the momenta of their decay products (muon/positron and corresponding (anti-)neutrino). This circumvents problems with current version of Rivet's `WFinder` implementation, which, even if more realistic, is not able to reconstruct both *W*-bosons properly from the considered final state.

9.5 Validation

The matrix element of the loop-induced process $gg \rightarrow W^+(\rightarrow e^+\nu_e)W^-(\rightarrow \mu^-\bar{\nu}_\mu)$ was validated against MCFM [72] and MadGraph5_aMC@NLO.

The SM background was checked by switching to MadGraph5_aMC@NLO (including MadLoop) as LO/NLO provider in Herwig instead of using GoSam. Additionally, the total cross section was successfully compared with the values in Ref. [71] at LO and NLO after adapting the setup to the 'basic' cut scenario described there.

9.6 Results

9.6.1 Gluon-induced contributions and BSM effects from the dimension-eight operators

To address all effects of the eight-dimensional EFT operators in detail, it is useful to restrict the study initially to the gluon-gluon channel, which is loop-induced in the SM.

In Fig. 9.2, p. 92 and in the following, the different contributions to the *gg*-channel, listed in Fig. 9.1, p. 86 or Eq. (9.11), p. 85, are separated and, in addition, analyzed after being combined differently: The contribution of the dimension-eight operators squared is named gg_Eff2, the loop-induced SM contribution gg_SM, the interference terms between both gg_Interf. As the interference is destructive in most parts, it is shown with the opposite sign (gg_NegInterf).

The combination of gg_SM and gg_Interf is designated as gg_SM+Interf. Likewise, gg_Eff2+Interf is the combination of gg_Eff2 and gg_Interf.

Finally, gg_All denotes the combination of all SM and BSM *gg* contributions including interference effects.

Where no scale-variation bands are shown in the plot (e.g. Fig. 9.9, p. 97), yellow bands in the ratio plots denote MC errors on the first plotted curve in each case, on which the ratio plots are always based. Except for tail regions with low statistics, MC errors can usually be neglected as they are much smaller than the scale variation effects.

The invariant mass of the W-boson pair is defined via the momentum of the decay products

$$m_{WW} = \sqrt{\left(p_{e^+} + p_{\nu_e} + p_{\mu^-} + p_{\bar{\nu}_\mu}\right)^2}. \tag{9.13}$$

Its distribution is shown in Fig. 9.2a.

For low energies, the (negative) interference terms, which are linear contributions from the dimension-eight operators, dominate over the quadratic contributions of the dimension-eight operators (`gg_Eff2`).

At around $400\,\text{GeV}$, both cancel each other and the quadratic contributions begin to dominate. This is also the point at which the sum of both (`gg_Eff2+Interf`) becomes positive. As expected, the quadratic contributions grow with the center-of-mass energy $\sqrt{\hat{s}}$ (here identical to m_{WW}). The exact values depend on the chosen ratio $\frac{c_i}{\Lambda^4}$, and are therefore valid only for the chosen set of BSM parameters, but by virtue of their linear or quadratic dependency can be easily rescaled to other values of this ratio and therefore give at least a qualitative picture.

The loop-induced SM contributions (`gg_SM`) reveal nearly the opposite behaviour, such that the BSM contributions, which are largely suppressed by c_i/Λ^4 or even $\left(c_i/\Lambda^4\right)^2$, dominate clearly beyond 500–$600\,\text{GeV}$ (including scale variation effects). Beforehand, they reduce slightly the SM cross section.

A low-energy effective theory can only describe physics properly at a scale sufficiently smaller than the scale of (possibly unknown) New Physics. It should therefore be noted that the point at which linear and quadratic contributions become equal can also be considered as the point at which the EFT approach begins to become invalid, since the suppression by powers of Λ is repealed by the growth proportional to s^2 and therefore also dimensional-10 and even higher operators would start to contribute considerably. In other words, the principle of power-counting (cf. Section 3.2, p. 30) will reach its limits.

In the high energy region, the dimension-eight operators violate also unitarity as discussed in Section 9.8, p. 107.

The $\Delta R_{WW} = \sqrt{(\phi_{W^+} - \phi_{W^-}))^2 + (y_{W^+} - y_{W^-})^2}$ observable is shown in Fig. 9.2b. ΔR_{WW} measures the azimuthal angle difference (i.e. the angle in the transverse plane) and rapidity distance between the two W-bosons. In contrast to the m_{WW} observable, the BSM effects are seen here in every bin. As part of the BSM contributions comes from the high-energy region, where the EFT approach breaks down, the values need to be interpreted carefully.

The results in this section are without showering and at LO. Therefore, the W-bosons are always back-to-back ($\Delta\phi = \pi$), which simplifies ΔR_{WW} to $\sqrt{(\pi)^2 + (\Delta y_{WW})^2}$, hence the region $\Delta R_{WW} < \pi$ is not (yet) populated. The LO calculation is also responsible for the high scale-variation uncertainty visualised by the shaded bands from a variation of $\mu_R = \mu_F$ by a factor 2 around their central value.
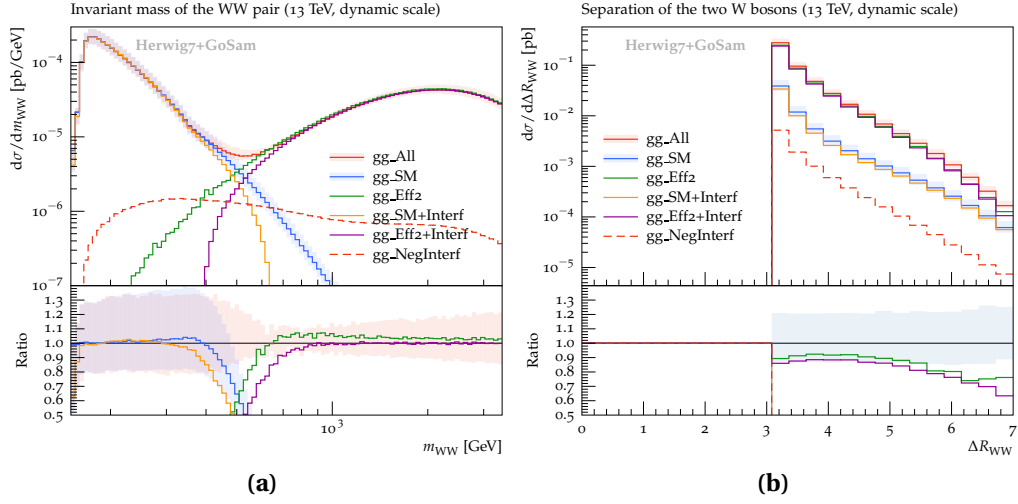
Figure 9.2: (a) Invariant mass distribution of the W-boson pair and (b) ΔR_{WW} distribution of gg-initiated SM/BSM contributions at $\sqrt{s} = 13$ TeV. For `gg_All` and `gg_SM`, scale-variation bands are shown.

The same observables are shown in Fig. 9.3 at the center-of-mass energy of $\sqrt{s} = 8$ TeV and the fixed scale $\mu_R = \mu_F = m_W$. At this lower energy, the BSM effects are less pronounced, but still beyond about 550 GeV clearly visible, where the dimension-8 operator starts to contribute considerably. This behaviour difference is not due to the choice of fixed vs. dynamic scale (cf. the fixed scale plot at $\sqrt{s} = 13$ TeV shown in Fig. E.1, p. 135).

With respect to the directly measurable observables, the effects of the higher dimensional operators are seen already at lower scales. Figure 9.4 shows the transverse momentum of the positron from the W^+ decay and the invariant mass of both charged leptons in the interesting lower energy region ($m_{e^+\mu^-}$). More than 20 % BSM effects are visible already above $p_{\perp,e^+} = 50$ GeV (or 80 GeV, taking scale variation effects into account). In the $m_{e^+\mu^-}$ distribution (Fig. 9.4b), the BSM effects are visible above 150–190 GeV.

Clear separation of SM and BSM contributions can be also seen in Fig. 9.5, p. 94, in which the relative azimuthal angles between the charged leptons ($\Delta\phi_{e^+\mu^-}$) and their
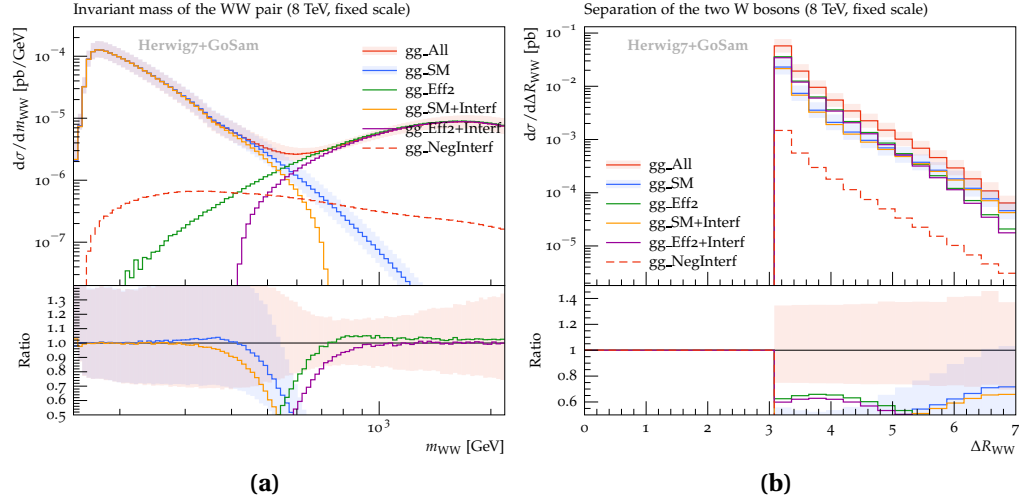
Figure 9.3: (a) Invariant mass distribution of the *W*-boson pair and (b) ΔR_{WW} distribution of *gg*-initiated SM/BSM contributions at $\sqrt{s} = 8$ TeV. For gg_All and gg_SM, scale-variation bands are shown.
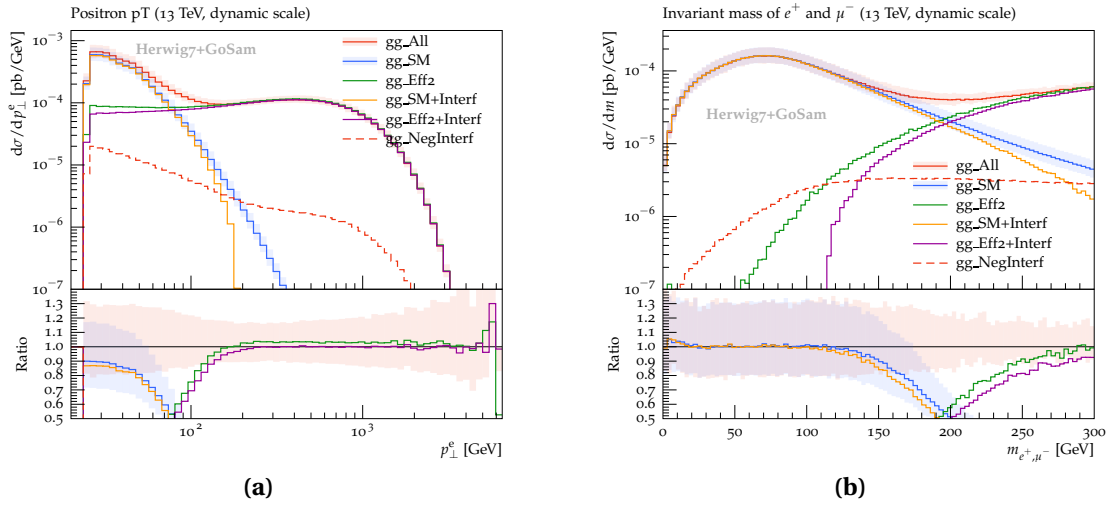
Figure 9.4: Transverse momentum of the positron (a) and invariant mass of the charged leptons (b), for the *gg*-initiated contributions. Scale-variation bands are shown for gg_All and gg_SM.
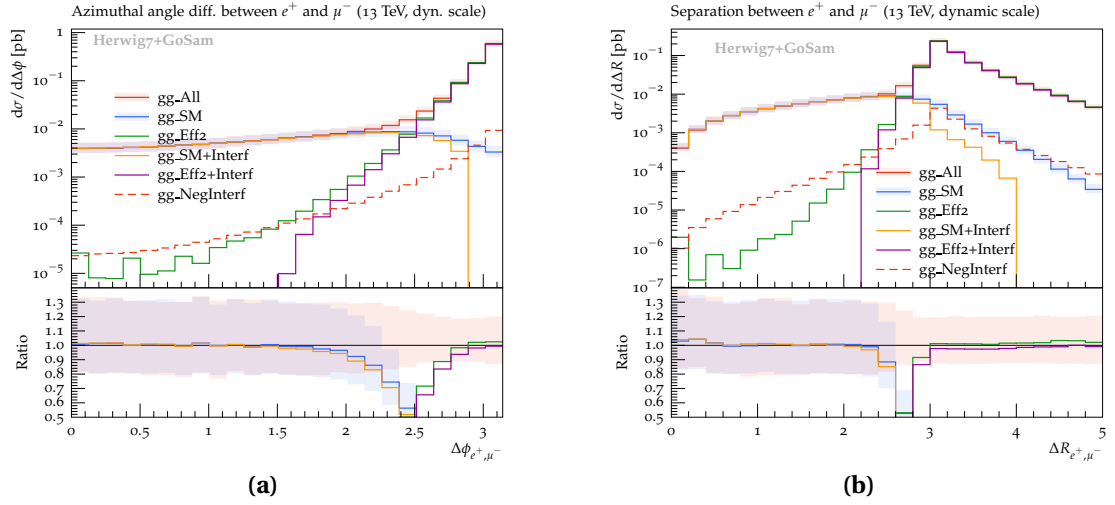
Figure 9.5: Distributions of (a) relative azimuthal angle $\Delta\phi_{e^+\mu^-}$ and (b) $\Delta R_{e^+\mu^-}$, for the *gg*-initiated contributions. Scale-variation bands are shown for `gg_All` and `gg_SM`.

$\Delta R_{e^+\mu^-}$ separation are plotted. In both observables, the higher dimensional operators contribute mostly in the upper bins, where the leptons are nearly back-to-back and probably originate from highly boosted *W*-bosons.

9.6.2 Scale choice

Most existing SM studies of the examined process have been performed at a fixed scale $\mu_F = \mu_R = m_W$. At higher energies, this choice is, however, at least questionable.

Figure 9.6 shows the difference between the dynamic and fixed scale for the full BSM contributions at $\sqrt{s} = 13\,\text{TeV}$. It can be seen that the scale variation bands do not overlap, therefore varying the scale by factor 2 around the central scale does not fully estimate the uncertainty from the scale choice for this process. This is especially true, if only the SM part is analyzed as in Fig. 9.7, p. 96. At least for the part in which the SM contributions dominate, the higher cross section of the fixed scale can be explained by the fact that nearly everywhere the fixed scale is much smaller than the dynamic scale and therefore leads to larger α_s values.

As in Fig. 9.2a, p. 92, the region around 600 GeV in which the BSM contributions begin to dominate shows a reduced dependency on the chosen scale. This is due to the fact

that the pure BSM contributions do not depend on the renormalization scale[3] and therefore only effects from the simultaneous factorization scale variation are seen.

The bands for the dynamic scale are slightly smaller than the fixed scale, which might suggest that the dynamic scale choice is more appropriate.

This topic is taken up again in Section 9.6.7, p. 101 where the results from the *gg* initial channel are combined with the full SM background.

(a)   **(b)**
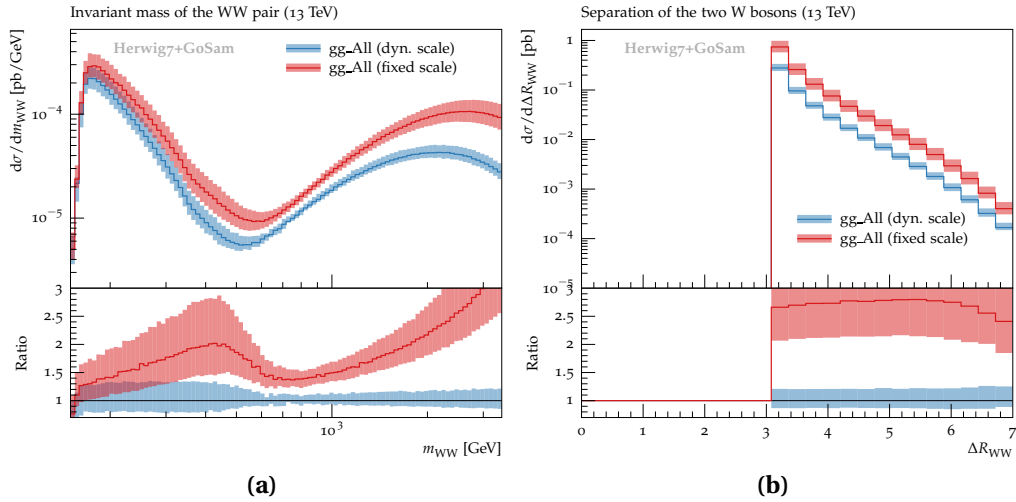
Figure 9.6: Comparison of the scale variations plots between the dynamic and fixed scale of the *gg*-initiated contributions, for (a) invariant mass distribution of the *W*-boson pair and for (b) the ΔR_{WW} distribution of *gg*-initiated SM/BSM contributions at $\sqrt{s} = 13$ TeV.

9.6.3 Comparison between the three dimension-eight operators

Whereas in the previous and following sections, the three dimension-eight operators are always shown combined, they are now analyzed separately by setting one $c_i = 0.3$ and the two others to zero in each case. The coefficient of the operator which should be analyzed is set to 0.3 instead of 0.1 to keep the same total magnitude of the BSM effects. This also helps to differentiate more easily between the operators.

---

[3] The leptonic decay of the *W*-bosons has still a scale dependency, but due to the slow running, it is neglected in this calculation.

(a)   **(b)**
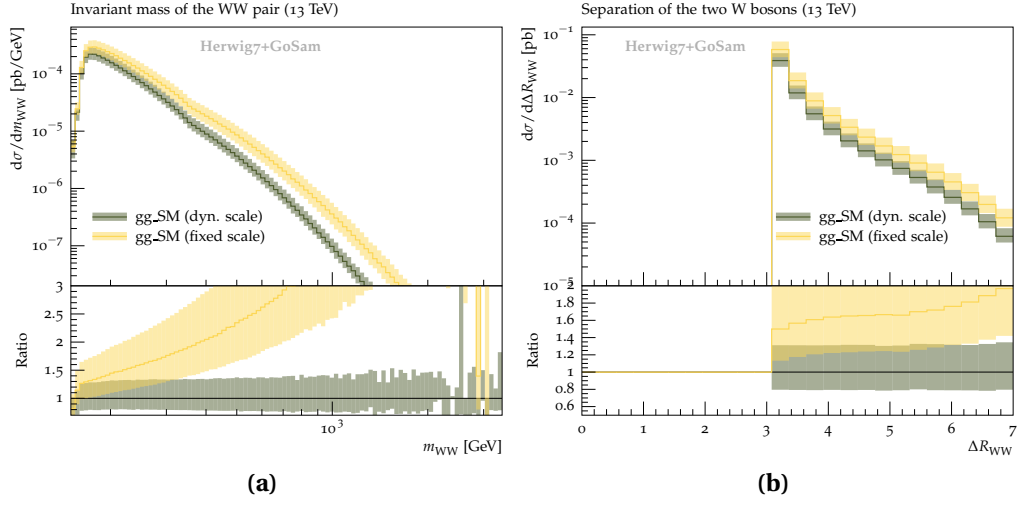
Figure 9.7: Comparison of the scale variations plots between the dynamic and fixed scale of the *gg*-initiated contributions, for (a) invariant mass distribution of the *W*-boson pair and for (b) the ΔR_{WW} distribution of *gg*-initiated SM contributions at $\sqrt{s} = 13$ TeV.

For better comparison, only plots at the fixed scale m_W are shown in this section.[4]

In Fig. 9.8, the distribution of the angle between the *W*-decay planes $\cos(\Psi)$ is plotted at $\sqrt{s} = 13$ TeV and 8 TeV, respectively. Since O_1 and O_2 has the same angular dependency if squared, `gg_Eff2_c2_0.3` masks `gg_Eff2_c1_0.3` perfectly. This is no longer true for the interference terms, so that `gg_All_c1_0.3` and `gg_All_c2_0.3` differ slightly.[5] At $\sqrt{s} = 13$ TeV, the total cross section is more dominated by the high-energy part of the higher dimensional operators than at $\sqrt{s} = 8$ TeV, such that the differences between the `gg_Eff2` and `gg_All` curves are much smaller.

It should be noted that O_3 has no angular dependency on its own. The remaining angle dependency — especially at the border of the plot (i.e. when the decay planes are almost perpendicular) — is due to the chosen cuts and is therefore removable.

Whereas O_3 can be distinguished easily from O_1 and O_2 in the $\cos(\Psi)$ observable, O_1 can be distinguished from O_2 and O_3 in the invariant mass distribution shown in Fig. 9.9 for $\sqrt{s} = 13$ TeV. Here, O_1 causes a larger decrease of the distribution around $m_{WW} \sim 500$ GeV.

---

[4]For the dynamic scale at 13 TeV, plots are listed in Fig. E.2, p. 136.

[5]In this section, all calculations were started with the same MC seeds, so that differences between curves are real and not statistical fluctuations.
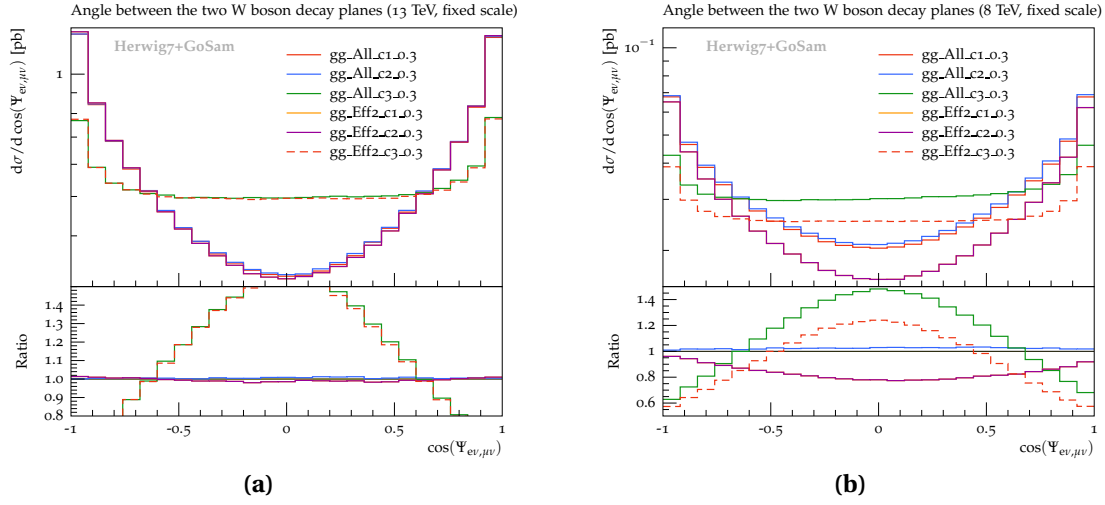
Figure 9.8: For the operators O_1, O_2, O_3, the distribution of the angle between the W-boson decay planes are shown for the fixed scale $\mu_R = \mu_F = m_W$ at (a) $\sqrt{s} = 13$ TeV and (b) $\sqrt{s} = 8$ TeV. The ratio plots are with respect to gg_All_c1_0.3 ($c_1 = 0.3$, $c_2 = c_3 = 0$).
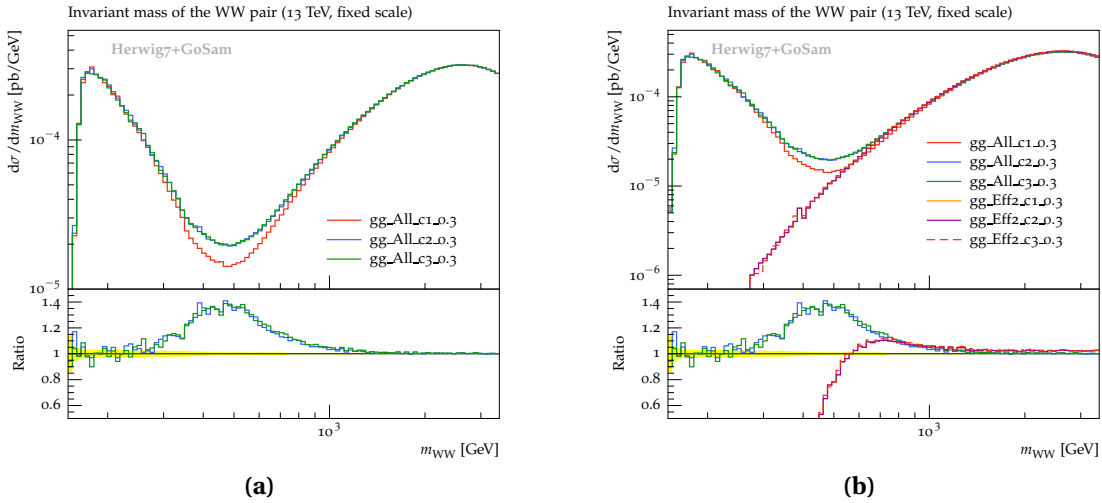
Figure 9.9: Invariant mass distribution of the W-boson pair for each dimension-8 operator at $\sqrt{s} = 13$ TeV and fixed scale m_W. In (b), the pure effects of each operator squared is added. It can be seen that O_1 and O_2 are identical in this observable (up to MC-errors). The ratio plots are with respect to gg_All_c1_0.3 ($c_1 = 0.3$, $c_2 = c_3 = 0$).

Combining these two observables $\cos(\Psi)$ and m_{WW}, all three operators can be distinguished from each other, at least in principal, since in practice, the overall BSM effect in the relevant areas of the combined analysis (discussed in Section 9.6.7, p. 101) might be too small to allow significant conclusions.

By using the different contributions as shown in Section 9.6.1, p. 90, and, additionally, splitting between the three operators, morphing techniques (cf. [329]) can be applied to fit the BSM parameters (i.e. the c_i parameters) to experimental data.

9.6.4 Enhancement of the interference effects
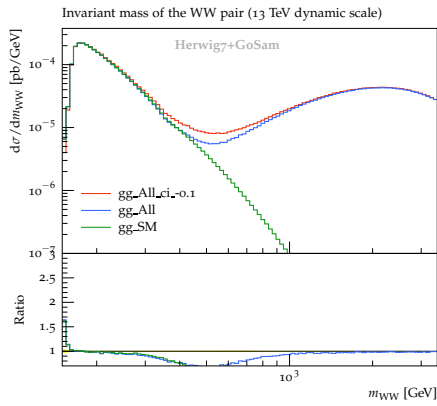
Figure 9.10: Comparison of the BSM effects between $c_i = -0.1$ and $c_i = 0.1$ (gg_All). The differences are only due to the different sign of the interference terms. The pure SM contributions (gg_SM) are also shown.

By choosing a negative value for the coefficients c_i in Eqs. (9.1) to (9.3), the BSM effects can be further enlarged as the interference terms are inversely proportional to the c_i and, therefore, increases the cross section. This is shown in Fig. 9.10 where the effect of $c_{i=1,2,3} = -0.1$ is compared with the $c_i = 0.1$ case that is used where not otherwise noted. The (negative) value of the interference terms can also be seen in Figs. 9.2 to 9.5 (pp. 92–94), designated gg_NegInterf. They are identical to the (positive) interferences in the $c_i = -0.1$ case.

Using different signs for c_i, the interference effects of the different operators cancel at least partly depending on the chosen observable.

The BSM-only terms (from the dimension-8 operators squared) depend on c_i^2 and are therefore not sensitive with respect to the sign of c_i.

9.6.5 Top mass effects in the Standard Model

Top-quarks are only contributing in the loop-induced $gg \to W^+W^-$ SM process, but not in the quark channels at NLO discussed later.[6] In contrast to the bottom quarks, whose mass effects are hardly visible (in the order of the Monte-Carlo uncertainties),

---

[6]This can be assumed for the LHC, where top-quarks in the initial state can be neglected and, moreover, a four-flavour scheme be used, but not necessarily at higher energies in future colliders.

	$\sigma_{gg,\mathrm{SM}}$ (generator cuts)	$\sigma_{gg,\mathrm{SM}}$ (analysis cuts)
with top mass (SM)	$(34.3 \pm 0.1)\,\mathrm{fb}$	$(18.65 \pm 0.01)\,\mathrm{fb}$
without top	$(33.00 \pm 0.02)\,\mathrm{fb}$	$(18.03 \pm 0.01)\,\mathrm{fb}$
$\Rightarrow$ top contribution	$4\,\%$	$3.3\,\%$
with massless top and bottom	$(74.31 \pm 0.02)\,\mathrm{fb}$	$(40.39 \pm 0.01)\,\mathrm{fb}$

Table 9.3: Effect of the top mass m_t to the total $\sigma_{gg,\mathrm{SM}}$ cross section.

the top-mass cannot be neglected.

In Ref. [72], the effect of the whole third quark generation was analyzed as the parameter of the top mass for the SM. In the following, the effect of including or excluding massive top quark loop is examined similarly. Two special cases are analyzed.

In the first case, designated `notop`, all top quark loops are excluded from the Feynman diagram used. This eliminates also all contributions from diagrams including bottom quarks, except one diagram in which a bottom triangle couples to the boson pair via Higgs boson. As the contribution of this diagram is suppressed by the small Yukawa bottom-Higgs coupling, the `notop` case is nearly identical to the two quark generation case.

In the second case, the otherwise massive quarks (tops and bottoms) are considered as massless (denoted by `massless`). This also switches off their Yukawa-couplings.

Neglecting the top quarks (`notop` case) has a minor effect on the total SM section of the loop-induced gluon-gluon channel. They contribute about 3–4 % (cf. Table 9.3).

In the invariant mass of the final-state leptons and their R-separation shown in Fig. 9.11, also no major effects are visible.[7]

Setting the masses of the third generation to zero (`massless` case), the effects are, as expected, much larger. The additional massless generation in the loops leads to a factor $\frac{9}{4} = 2.25$ (cf. [72]), here slightly reduced to about 2.16 in the total cross section due to the chosen cuts. The effect can also be seen in Fig. 9.12, in which the invariant mass and the R-separation of the charged leptons in the final state are plotted.

With respect to the whole BSM process, the influence of the contributions of top quark loops is less distinct. With the massless third-generation, the effects are up to about 10 % (cf. Fig. 9.13, p. 101), whereas in the `notop` case, the contribution to

---

[7]The invariant mass distribution of the W-bosons plotted in Fig. E.4, p. 137 shows similar behaviour.
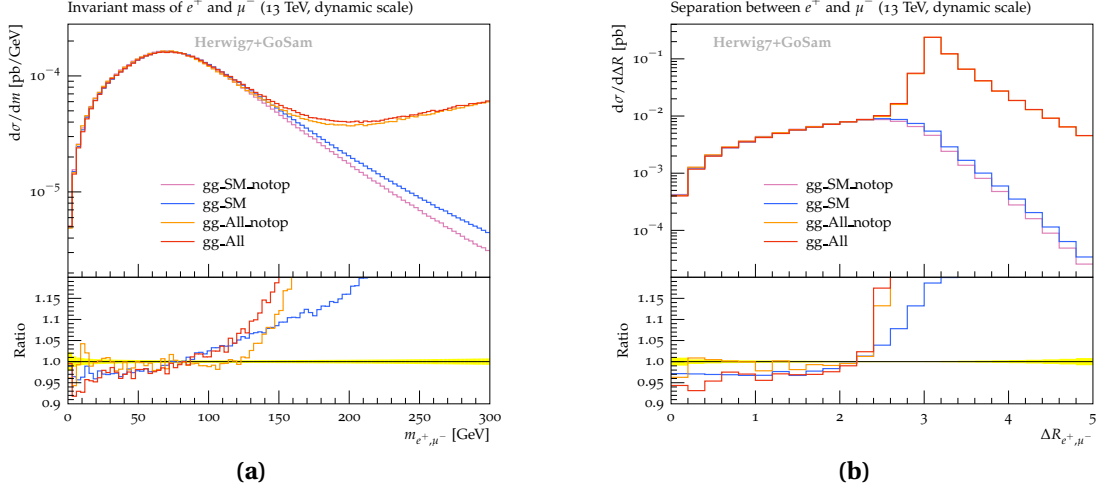
Figure 9.11: Distribution of the invariant mass (a) and ΔR-separation (b) of the charged leptons. In the `_notop` curves, diagrams with top-quarks have been omitted.
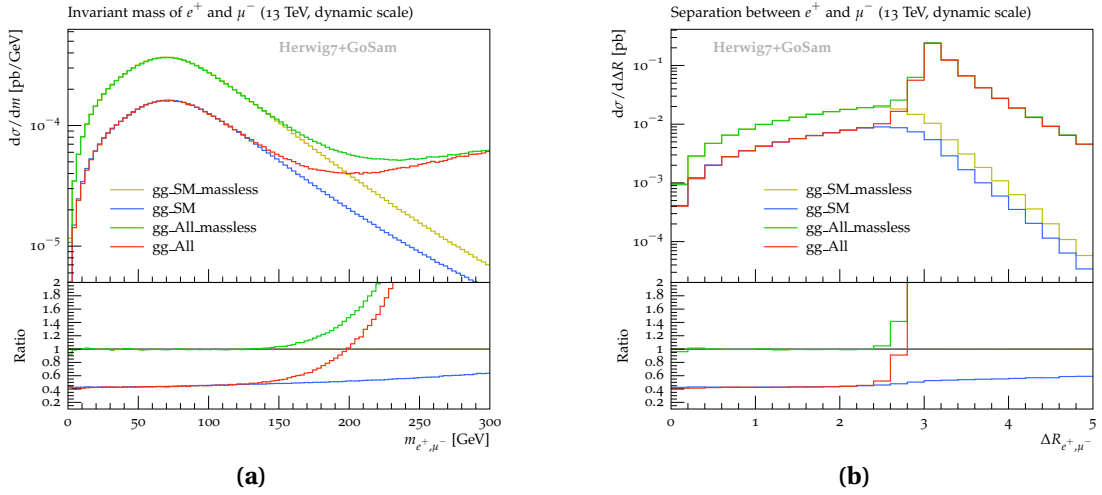
Figure 9.12: Distribution of the invariant mass (a) and ΔR-separation (b) of the charged leptons. For the curves labeled `_massless`, the top and bottom quarks were assumed to be massless. For better visibility, only the area is plotted in the $m_{e^+\mu^-}$ distribution, where the BSM effects begin to dominate.

the total SM or BSM cross section is less than 1 % and therefore, also in the various differential distributions, within the scale variation and MC uncertainties. [8]
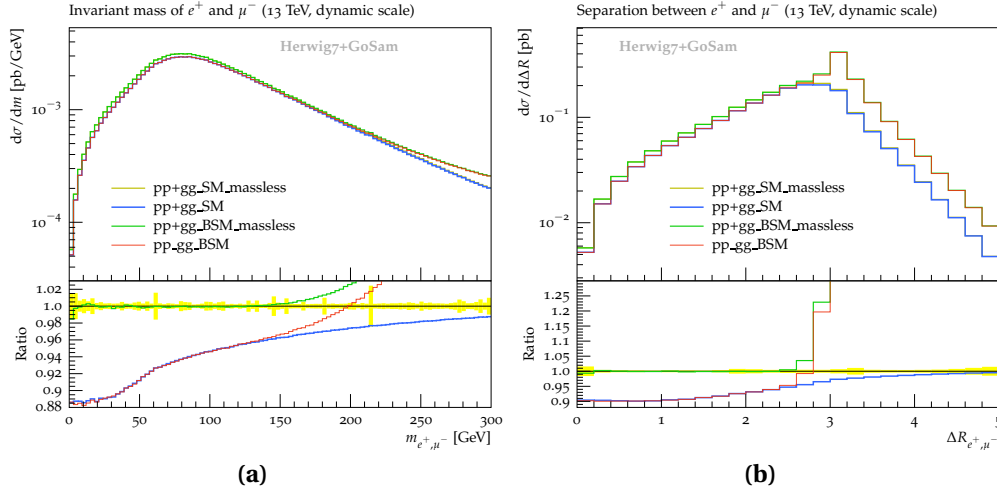
Figure 9.13: For the full pp initial state, impact of massive vs. massless top-quark loops on (a) the invariant mass of the charged leptons and (b) $\Delta R_{e^+\mu^-}$ distribution

In summary, the analysis shows that the top mass effects are small, but can partly obscure BSM effects. It could be verified that the error introduced by omitting the top entirely is substantially smaller than considering it (or the whole third generation) as massless.

9.6.6 Quark-initiated Standard-Model part

In the SM, the $e^+\nu_e\mu^-\bar{\nu}_\mu$ final state can also be produced from quarks and anti-quarks in the initial states. This is therefore a background to the previously discussed BSM effects. In the real radiation processes at QCD NLO, also qg and $\bar{q}g$ initial states need to be considered.

9.6.7 Combined results

The full result is shown in Fig. 9.14 in which the invariant mass and the ΔR_{WW} separation of the reconstructed W-bosons are plotted in the combined quark-quark/quark-gluon SM NLO calculation with the analyzed gluon-gluon-channel including the

---

[8]Further plots of the mass effects are shown in Fig. E.3 and Fig. E.4, p. 137.

anomalous couplings isolated in the previous sections.

In the combined results, the BSM effects impinge at the m_{WW} distribution at about 700 GeV, whereas in the gluon-gluon-channel, they are already distinguishable from 500–600 GeV and onwards. In the ΔR_{WW} distribution (Fig. 9.14b), now also the left side $\Delta R_{WW} < \pi$ is filled by the real radiation of the qq/qg NLO calculation.
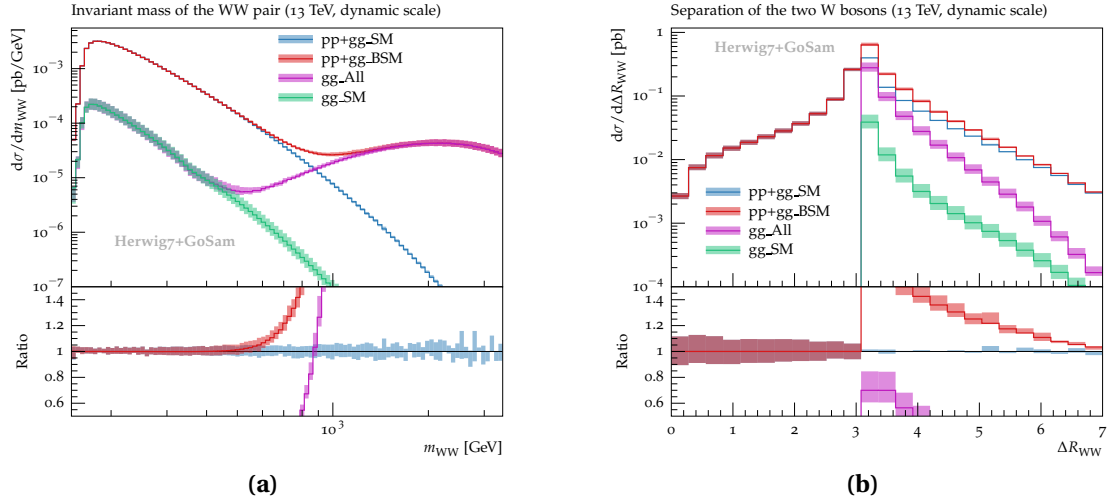
Figure 9.14: Invariant mass distribution m_{WW} and ΔR_{WW} separation of the W-boson pair. All calculated SM/SM+BSM contributions from the partonic channels are included, i.e. the quark-initiated channels at NLO in QCD are combined with the loop-induced SM gg-contributions, and for the BSM curves (`_All`), also with all effects of the dimension-8 operator. In addition, the gg-contributions are shown separately.

The difference between the dynamic scale ($\mu_{F,R} = m_{WW}$) and fixed scale ($\mu_{F,R} = m_W$) choices are shown in Fig. 9.15. The conclusions are similar to the previous analyzed gluon-channel. The relatively low fix scale leads again to a higher cross section and larger scale variation bands as the dynamic scale.

It should be noted that the gluon-gluon and the quark-initiated channels have inverted behaviour with respect to scale variation, which reduces the scale dependency on the combined results, but may also lead to an underestimation of the total scale uncertainty. Hence, an uncertainty estimation from the scale variation of the combined results must be approached carefully. Independent variation of μ_R and μ_F

could yield a better estimation of the actual scale uncertainty.[9]
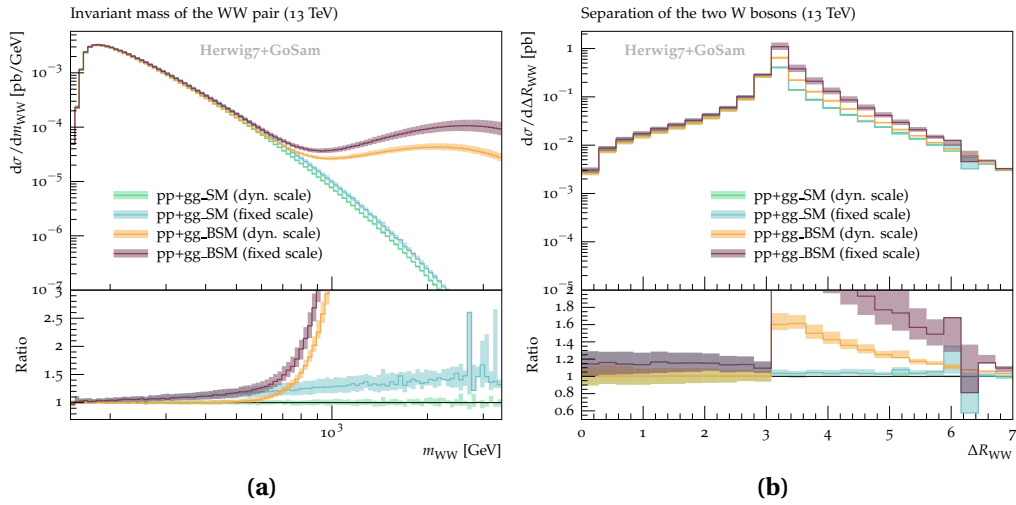
Figure 9.15: Comparison of the scale variations plots between the dynamic ($\mu_{F,R} = m_{WW}$) and fixed scale ($\mu_{F,R} = m_W$) of the gg-initiated contributions, for (a) invariant mass distribution of the W-boson pair and for (b) the ΔR_{WW} distribution of gg-initiated SM contributions at $\sqrt{s} = 13\,\text{TeV}$.

---

[9]cf. the scale variations performed in Ref. [71], which compares the default scale variation method (using $\mu_{R,F} \to \xi\mu_{R,F}$; $\xi = \{2, \frac{1}{2}\}$) to an opposite variation ($\mu_R \to \xi\mu_R \wedge \mu_F \to \frac{1}{\xi}\mu_F$).

9.7 Shower effects

The measured observables at hadron colliders contain parton shower effects, therefore the fixed-order result from the previous sections are supplemented by parton shower effects in this section.

The Herwig angular ordered parton shower [330] based on [331, 332] is used as shower algorithm with the subtractive matching algorithm (MC@NLO-like) [172, 333]. Only pure QCD-showering is enabled, as the effect of hadronization or full showering is negligible for the studied observables. Therefore, the decay products of the W-boson do not shower or hadronize and are affected only by the changed kinematic of the shower. This allows retentions of the direct and unique reconstruction of the W-bosons from their decay products in the analysis code without using advanced reconstruction techniques. This procedure, which accelerates the calculation considerably, was confirmed by initial studies with fully showered and hadronized events using the `WFinder` implementation of prior Rivet versions, which were able to reconstruct the W-bosons correctly from those final states.

For the reconstruction of jets from the parton shower and the real radiation, the library FastJet [334, 335] is used with the anti-k_T jet clustering algorithm [336]. The radius is set to $R = 0.4$.
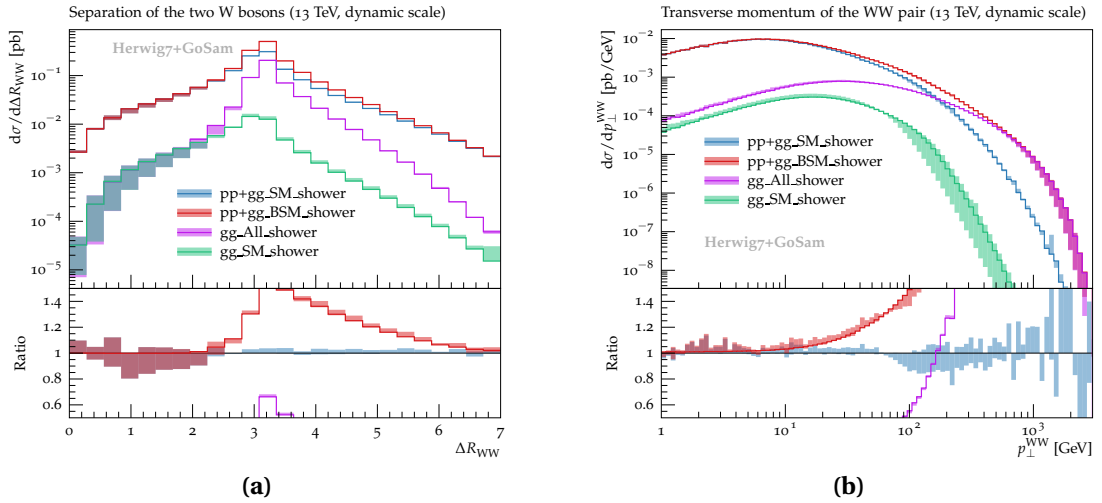
Figure 9.16: Shower effects in the (a) ΔR and (b) $p_\perp$ distributions of the reconstructed W-boson pair for the sum of all partonic channels (pp+gg_) and only in the gluon-gluon-channel (gg_) including μ_Q variations and optionally BSM effects from the dimension-8 operators.
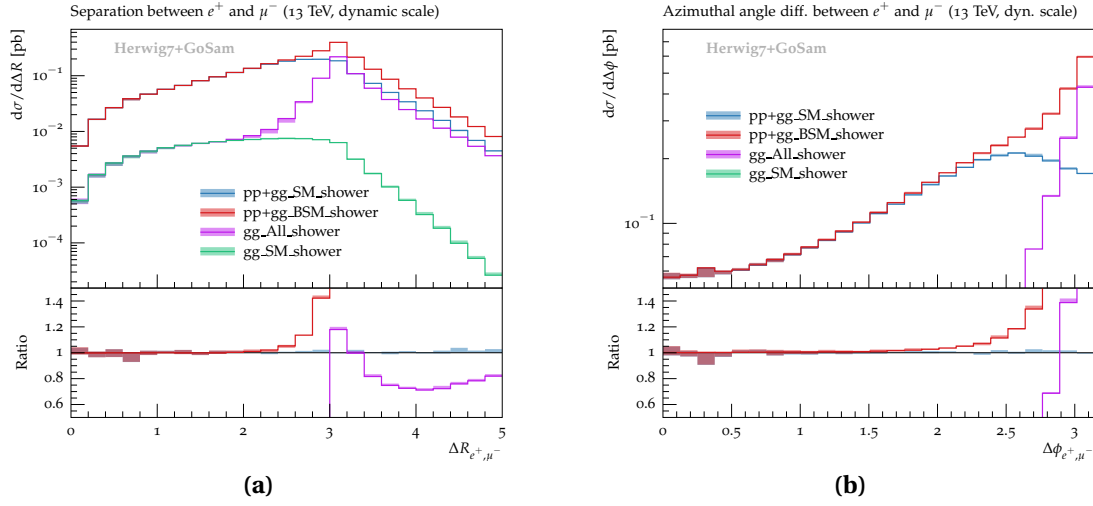
Figure 9.17: Shower effects in the $\Delta R_{e^+\mu^-}$ (a) and (b) $\Delta\phi_{e^+\mu^-}$ distributions.
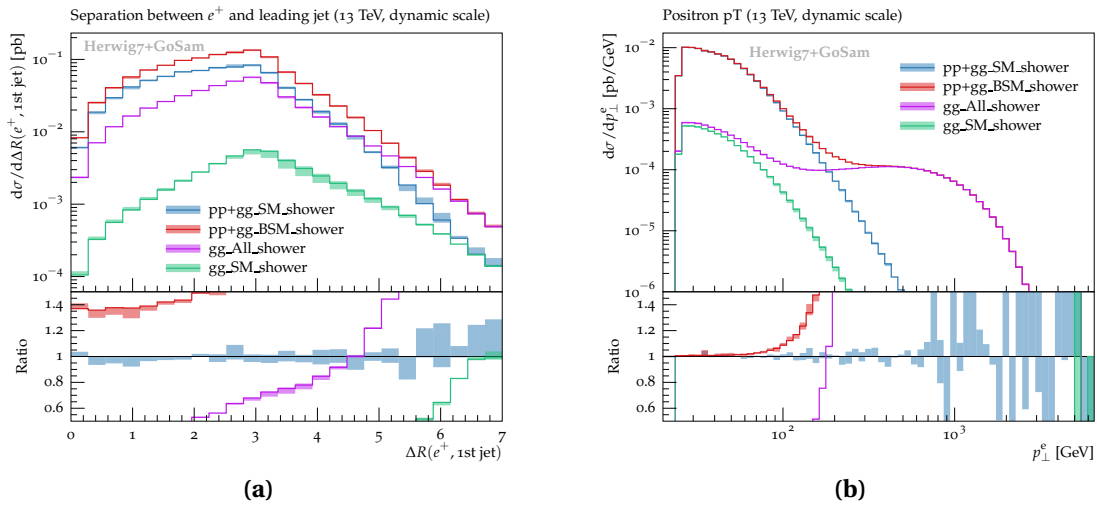
Figure 9.18: Shower effects in the (a) ΔR_{e^+j} and (b) $p_\perp^e$ distributions.

For the leading order calculations (these are the loop-induced ones) the built-in MC@LO algorithm is used (instead of the `DefaultLO-Shower` which includes some matrix-element corrections). This allows a fair comparison between the showered LO and NLO results and does not disturb the chosen order.

Instead of varying the factorization and renormalization scale to quantify the uncertainties, as for the fixed-order results, the hard shower scale μ_Q is altered by factor 2 in either direction. This estimates the effect of non-optimally modelled emissions at large angles and missing logarithmic contributions. Alternatively, another shower algorithm could have been chosen.

Parton shower effects are only visible in infrared-sensitive observables. Other observables, as for example the invariant mass of the W-pair m_{WW}, are — as expected — not affected by the shower, which gives some evidence for the correctness of the showering procedure employed.

In Fig. 9.16, p. 104, the ΔR and $p_\perp$ distributions of the reconstructed W-boson pair are plotted. It can be seen that in the R-difference plot, the left side ($\Delta R < \pi$) of the gg-contribution is now also filled by the additional radiation from the parton shower and is therefore very sensitive to μ_Q-variation. In the combination of all channels, the shower uncertainty is reduced, since in the mostly prevailing qq/qg channels, real radiation contributes and therefore a NLO matching procedure is applied, which is less sensitive to μ_Q-variation. In the $p_\perp$ plot (Fig. 9.16b), it can be seen that at large momentum, where the BSM dominates, the shower uncertainties are large since the shower is responsible for all radiation. LO multi-jet merging or, preferably, calculating QCD corrections to the existing gg-channel contributions should reduce this uncertainty. Another method is to use other observables, like the R- and ϕ-separation of the charged leptons shown in Fig. 9.17, p. 105. They are hardly effected by the parton shower, but distinguish well between SM and BSM effects.

For the experimental reconstruction of the W-bosons from the final state, additional observables are interesting. In Fig. 9.18a, p. 105, the R-separation between the positron and the leading jet is displayed. Jets are produced by the parton shower and real-radiation. At low separation values, the BSM effects do not change the shape, but only increase the cross section, so that experimentally needed cuts in this region for a lepton-jet isolation should not introduce any large bias. The R-separation is partly affected up to 10 % by variations of the parton shower scale by factor two (neglecting effects from large MC uncertainties at low statistic), but is, in most regions, quite stable.

In the transverse momenta distribution of charged leptons, shown in Fig. 9.18b, p. 105 for the positron, BSM effects are clearly recognizable for transverse momenta be-

yond about 100 TeV. Here, shower effects are only secondary. The missing transverse momentum distribution, which is also important for the reconstruction, shows comparable behaviour[10].

9.8 Unitarity bound

At higher energies EFT breaks down, as the effect of higher dimensional operators rises with increasing center-of-mass energy, so that unitarity may be violated. This is especially true for the dimension-8 operators discussed here.

Using the related $2 \rightarrow 2$ process with stable W-bosons in the final state, a unitary bound can be calculated and, similarly, a limit to the operator strengths c_i.

As discussed in [1] (a similar calculation was performed in [337]), from the unitarity property of the scattering matrix (i.e. $\hat{S}\hat{S}^{\dagger} = 1$), a limit on the partial wave expansions of the integrated inelastic scattering amplitude $\hat{T}$ (defined by $\hat{S} = 1 + i\hat{T}$) can be derived. For the gluon initial state and the total angular momentum $J = 0$, this yields for the inelastic $2 \rightarrow 2$ scattering amplitude T^{in} integrated over the corresponding phase space PS_2 (similar to Eq. (B.12) in [337]):

$$\sum_{\lambda_3,\lambda_4} \int \mathrm{d}PS_2 \left|T^{\mathrm{in}}\right|^2 \leq 8\pi \tag{9.14}$$

with the final state helicities $\lambda_{3,4}$.

Inserting this limit into the total cross section, which is averaged over the colours in the initial state, summed over the helicity and colour configurations in the final state and contains the flux factor $\frac{1}{2\hat{s}}$ with the partonic center-of-mass energy $\hat{s}$,

$$\sigma_{ggWW} = \frac{1}{2\hat{s}}\frac{1}{4}\frac{1}{(N_c^2-1)^2} \sum_{\mathrm{colours}} \sum_{\lambda_1,\lambda_2} \sum_{\lambda_3,\lambda_4} \int \mathrm{d}PS_2 \left|T^{\mathrm{in}}\right|^2, \tag{9.15}$$

yields the limit (with $N_c = 3$ and four helicity configurations in the initial state):

$$\sigma_{ggWW} \leq \frac{\pi}{2\hat{s}} \tag{9.16}$$

---

[10]cf. Fig. E.5, p. 137.

which unfortunately cannot be translated directly into a limit on the full $2 \rightarrow 4$ cross section that is used in this chapter, especially as it includes cuts on the decay-products.

By projecting the full amplitude to single partial waves (usually the lowest are used, as they contribute most), limits on the absolute values of the c_i values can be obtained, giving the strength of the dimension-8 operators.

From the 0th-partial wave, the limit for the first two operators from longitudinally polarized W-bosons (the third operator is not contributing) is:

$$\left|\frac{c_{1,2}}{\Lambda^4}\right| \leq \frac{2\pi}{m_W^2 \hat{s}} \tag{9.17}$$

and from transversally polarized W-bosons (here the third operator contributes), the even stronger limits are

$$\left|\frac{c_{1,2}}{\Lambda^4}\right| \leq \frac{30\pi}{\hat{s}(26\hat{s} - 11m_W^2)}, \qquad \left|\frac{c_3}{\Lambda^4}\right| \leq \frac{\pi}{\hat{s}^{\frac{3}{2}}\sqrt{\hat{s} - m_W^2}}. \tag{9.18}$$

These can be simplified and estimated by

$$\left|\frac{c_i}{\Lambda^4}\right| \lessapprox \frac{\pi}{\hat{s}^2} \tag{9.19}$$

for $\hat{s} \gg m_W^2$. The value of $c_i = 0.1$ and $\Lambda = 1\,\text{TeV}$ (cf. Table 9.1, p. 88) corresponds therefore to a unitarity bound of $\hat{s} \approx (2.3\,\text{TeV})^2$.

As can be seen, the unitarity bounds found here raise doubts about effects near or beyond few TeVs, which have been already described as probably less valid.

To avoid possible problems introduced by unitarity violation at higher energies, form factors are used in the calculations in the next section.

9.9 Effects at 100 TeV

9.9.1 Motivation

The Future Circular Collider (FCC) at CERN is planned as successor of the LHC. It is designed for $\sqrt{s} = 100\,\text{TeV}$ which provides the collision energy used in this chapter. The FCC opens a wide window for BSM searches and SM precision tests [338].

Going to higher collision energies, not only the available phase space increases, but also effects from the gluon-gluon initial channel are further enhanced at low Bjorken-x values.

Experimental difficulties arise such as increased pile-up, higher probability of additional jets, or, especially important for this analysis, decaying W-bosons that are hard to distinguish from other jets.

As the production rate of multiple-gauge-bosons events is high enough, the analysis can also be extended to e.g. $W^+W^-W^+W^-$ production (with a SM cross section of $\sigma_{\mathrm{NLO}} \approx 41\,\mathrm{fb}$ at 100 TeV [339]).

A full study at 100 TeV would need to include further effects like the radiation of electroweak bosons that can be neglected at lower energies.

9.9.2 Setup

In this calculation, the setup is, however, extended to $\sqrt{s} = 100\,\mathrm{TeV}$ only in a simple manner. For more stable and faster calculation, the analysis cuts are directly applied at generation level. Other adaptions to future colliders are not included. For example, four (massless) quark flavours in the initial state are still assumed instead of switching to a six-flavour scheme.

9.9.3 Form Factor

To tame the dimension-8 operators at high energies, at which they would generate unphysical results and dominate most observables, and to preserve unitarity, the following dipole form factor[11] is applied:

$$\mathcal{F} = \left(\frac{\Lambda_{FF}^2}{\Lambda_{FF}^2 + m_{WW}^2} \right)^{n_{FF}} = \frac{1}{\left(1 + \frac{m_{WW}^2}{\Lambda_{FF}^2} \right)^{n_{FF}}} \qquad (9.20)$$

Figure 9.19: The form factor $\mathcal{F}$ with $\Lambda_{FF} = 1\,\mathrm{TeV}$ and $n_{FF} = 4$.

with m_{WW} from Eq. (9.12), p. 87, $\Lambda_{FF} = 1\,\mathrm{TeV}$ and $n_{FF} = 4$. This is plotted in Fig. 9.19. The form factor is

---

[11]In this context, the term *form factor* is used differently than in the context of one-loop reduction formulae like in Chapter 7, p. 63.

comparable to a soft cut-off of the influence of the higher-dimensional operators at higher energy scales.

A similar form factor is used in VBFNLO [164], where it is suggested for anomalous quartic gauge couplings. It is also applied in the case of extra dimensions [340].

Whilst using a form factor bypasses the unitarity problem, its definition introduces some arbitrariness. This is avoided in the calculation of the previous sections performed at LHC energies. Since at the higher collision energy used in this section, most observables would be clearly dominated by the high-energy tail of the eight-dimensional operators, the arbitrariness is accepted in favour of at least qualitatively interpretable results.

9.9.4 Results

The results are shown in Fig. 9.20 for the gluon-gluon channel. In comparison to the previous plots at 13 TeV, it can be seen that the form factor reduces the BSM contributions drastically at high energies, such that other differential observables would no longer be dominated by the high energy tail of the anomalous couplings.

Due to the form factor, the invariant mass of 650 GeV, where the contributions of the higher-dimension squared contributions (`gg_Eff2`) have the same magnitude as the loop-induced SM contributions (`gg_SM`), is slightly shifted by about 150 GeV towards higher energies compared with the plots at 13 TeV.

Another interesting feature is that scale-variation uncertainties appear only at the $\mathcal{O}(15\,\%)$ level at low energies (in comparison to $\mathcal{O}(30\,\%)$ at 13 TeV). At higher energies, uncertainties from the scale-variation are practically irrelevant (neglecting fluctuations at very high energies due to low statistic).

The combined analysis is shown in Fig. 9.21. Similarly, the part in which BSM contributions dominate is shifted slightly towards higher energies. Compared with the results at 13 TeV, the 100 TeV results show again a reduced dependency on the factorization and renormalization scale.

Showered results are shown in Figs. 9.22 to 9.23, p. 112. The shower effects are similar as at 13 TeV. Comparing the ΔR_{WW} plots (Fig. 9.21b and Fig. 9.22a, p. 112), it can be seen that the shower reduces the BSM effects in the $\Delta R \geq \pi$ since the additional radiation allows $\Delta R < \pi$ kinematic.
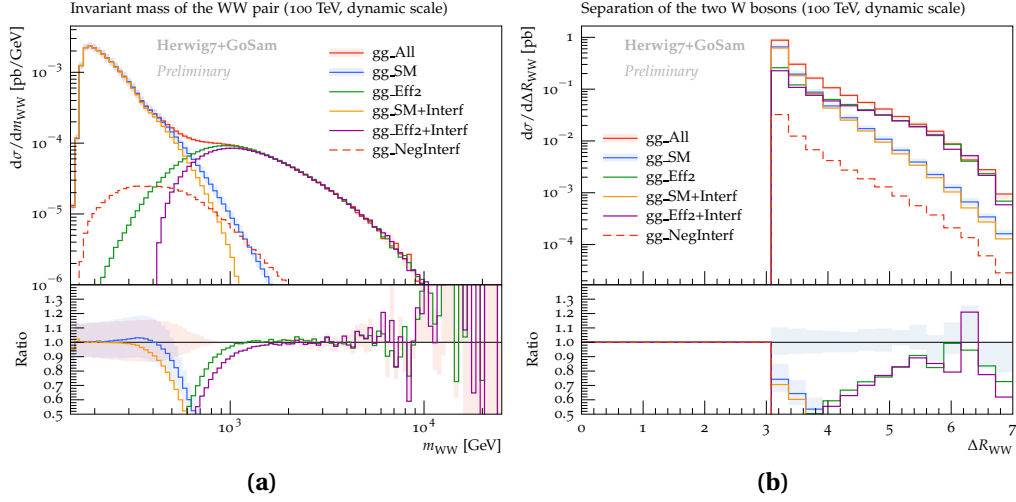
Figure 9.20: Different contributions to the gluon-gluon channel in the (a) invariant mass and (b) ΔR-separation of the reconstructed W-boson pair at $\sqrt{s} = 100$ TeV.
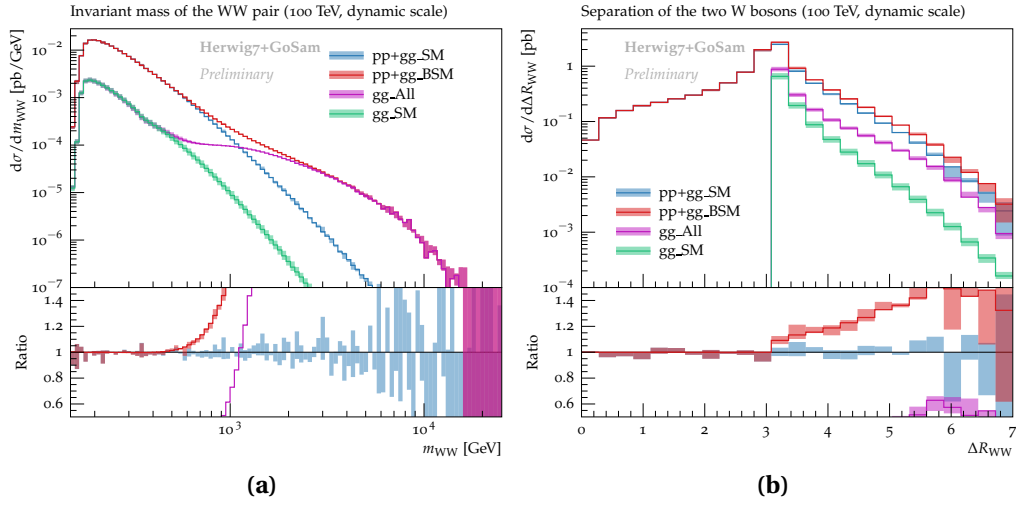
Figure 9.21: (a) Invariant mass and (b) ΔR-separation of the reconstructed W-boson pair at $\sqrt{s} = 100$ TeV. All contributing channels are shown.

(a) **(b)**
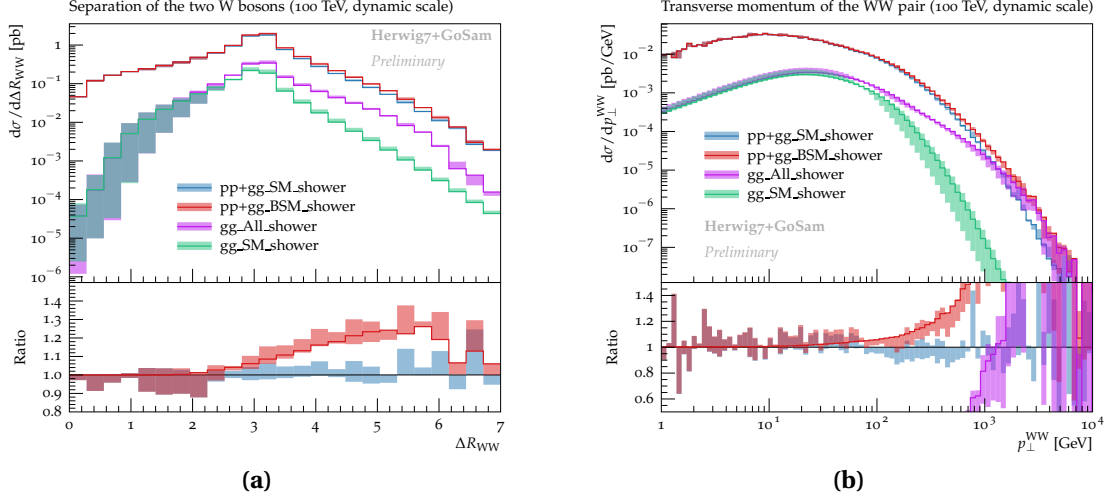
Figure 9.22: (a) ΔR and (b) $p_\perp$ distributions of the reconstructed W-boson pair with parton shower effects for the sum of all partonic channels (pp+gg_) and only in the gluon-gluon-channel (gg_) including μ_Q variations and optionally BSM effects from the dimension-8 operators at $\sqrt{s} = 100\,\text{TeV}$.

(a) **(b)**
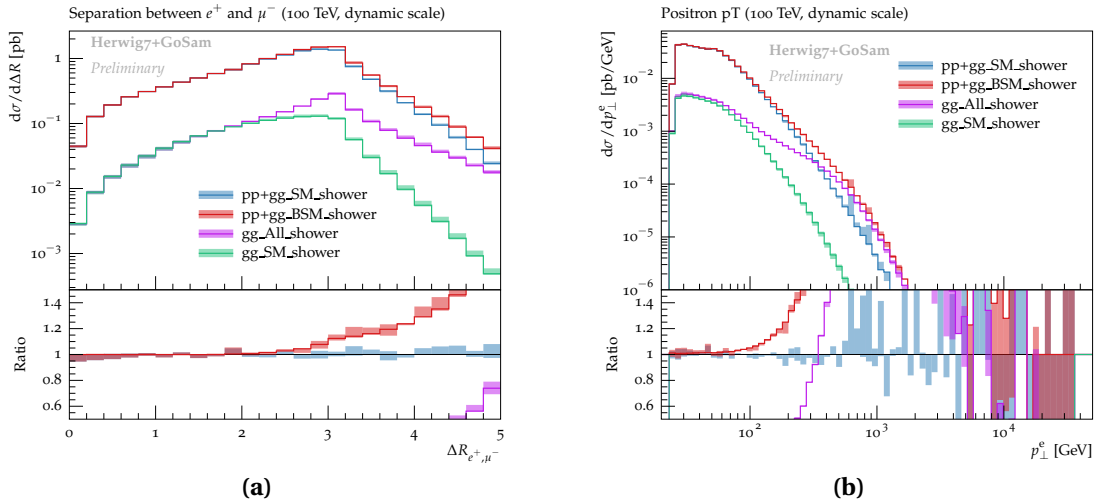
Figure 9.23: (a) $\Delta R_{e^+\mu^-}$ and (b) $p_\perp^e$ distributions with parton shower effects for $\sqrt{s} = 100\,\text{TeV}$.

Part IV

Summary and Outlook

10 Summary and Outlook

The calculation of high energy amplitudes for multi-particle processes at the LHC with (at least) one-loop precision is of basic importance for the current and future research in particle physics.

In this thesis, recent developments in GoSam, a framework for calculating one-loop amplitudes in an automated way, and the tensor integral library Golem95C have been presented.

The developments in GoSam have been used to calculate the process of W-pair production in proton-proton collisions including the subsequent decays of the W-bosons ($pp/gg (\to W^+W^-) \to e^+\nu_e \mu^- \bar{\nu}_\mu$) at NLO QCD. Effects from the gluon-gluon channel have been considered, which are technically NNLO contributions, since they are loop-induced, but greatly enhanced due to the large gluon luminosity at LHC and future proton-proton colliders. In particular, anomalous couplings from dimension-eight operators have been studied, which introduce a tree-level coupling between gluons and electroweak bosons.

As this process is an important background for Higgs boson measurements and allows to study the electroweak sector, precise predictions are needed. The anomalous couplings employed describe contributions from unknown Physics Beyond the Standard Model (BSM) in a generic way. Effects, such as destructive interferences, are analyzed, which make it more difficult to give strong limits on the strength of the applied BSM operators. The setup used can be easily extended to other decay channels, and similar processes, such as $ZZ/Z\gamma$ production that would also be affected by dimension-eight operators, which result from the same effective Lagrangian.

The extensions developed and the new features in GoSam, which were released in its 2.0 version and subsequent point releases, allow multiple future applications within the Standard Model (SM) and, especially, beyond. With all the various improvements discussed, a faster and more reliable calculation with GoSam is possible. The improved and simplified user interface broadens its application possibilities.

One of the main new features of GoSam 2.0 is the support of the Binoth Les Houches Accord 2 (BLHA2) [8], which has been integrated and helps to bundle or integrate

GoSam in other programs, especially Monte-Carlo event generators. Via the BLHA2 interface, GoSam can now provide matrix elements for all parts of an NLO calculation and even in extended applications like multi-jet merging calculations or mixed QCD-electroweak-calculations in an automated way. The interface allows various parameters to be set at runtime. A simplification is the automatic choice of the electroweak scheme if the built-in SM model files are used.

The extension of the tensor integral library Golem95C to higher ranks, mainly rank-6 five-point integrals (pentagons) and rank-7 six-point integrals (hexagons), broadens its applicability to loop calculations with effective field theories or spin-2 particles.

These developments discussed in this thesis can help to calculate theoretical predictions in the future of high energy physics. With the upgrade of the LHC to higher luminosity, called HL-LHC, in the coming years (cf. Fig. 10.1), the goal will be to reach $3000\,\mathrm{fb}^{-1}$ integrated luminosity. With this high luminosity, processes, which are currently inaccessible due to large statistical uncertainties, will become accessible. In addition, it provides multiple opportunities for achieving signatures of new physics.
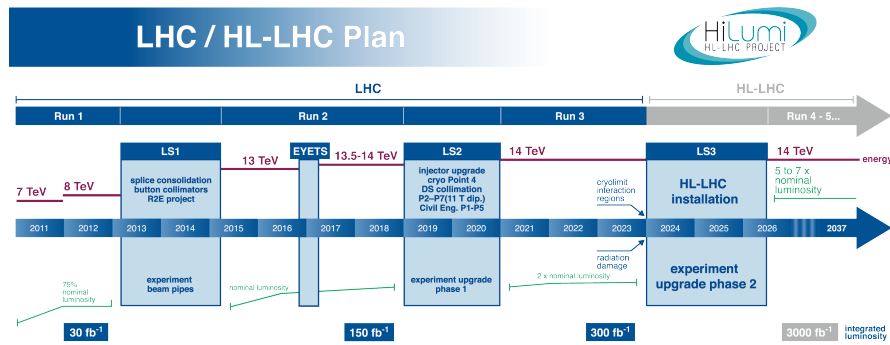
Figure 10.1: Plans for the higher luminosity upgrade plans of the LHC towards HL-LHC [341].

Beside the HL-LHC upgrade, there are several other plans and ideas for future colliders:

The Future Circular Collider (FCC) at CERN is a study for a new circular hadron collider and is destinated for a center-of-mass energy of $\sqrt{s} = 100\,\mathrm{TeV}$. In this thesis, the calculation of $pp/gg\,(\rightarrow W^+W^-) \rightarrow e^+\nu_e\,\mu^-\bar{\nu}_\mu$ has been extended to this high center-of-mass energy. A form factor has been applied that reduces the growth of the dimension-8 operators at high energies, which circumvents unitarity problems.

China's Circular Electron-Positron Collider (CEPC) is planned to be a circular lepton-collider and will, if it could be realized, therefore be a successor of the Large Electron-Positron Collider (LEP). Due to synchrotron radiation and the associated energy loss on circular colliders, the maximum achievable collision energy is limited for such circular lepton-colliders. The CEPC is, however, intended to be retrofitted subsequently to a hadron collider.

The future International Linear Collider (ILC) or Compact Linear Collider (CLIC) for electron-positron collisions avoid the synchrotron radiation problem. These colliders would be especially helpful for precision studies due to their clean signal and possibility for threshold scans of, e.g., top quark pair production to measure the top mass.

For hadron-lepton colliders, there are also plans to combine the circular and linear approach as in $ep/\mu p$-FCC studies.

These possible further colliders will allow further precision measurements on the Higgs boson discovered recently and possibly even on new, as yet unknown, physics Beyond the Standard Model. In all cases, they will either find new physics or push further the exclusion limits for various possible BSM models.

Regarding the automation of higher order corrections, a continuous development effort will be needed to keep up with precision measurements by the experiments. Whereas computing power will increase further, this in itself will not be sufficient to satisfy all needs. Already tested approaches, such as massive parallelization, GPU-computing, etc., might play a more important role.

In particular, future hadron colliders will be accompanied by an increased demand for prediction with higher multiplicity, i.e. more jets in the final state. Electro-weak corrections and corrections beyond NLO will also be more important, in particular if higher precision is needed. These requirements for future calculations imply not only a large rise in combinatorial effects, for example in the involved Feynman diagrams, which result in bigger code sizes and longer runtimes, but bring also conceptual challenges, for example how the different contributions can be combined correctly.

The request for general, fully automated, user-friendly tools, which can be used by non-experts, is in tension with the further specialization required to solve the different up-coming challenges.

These problems may be solved by creating even larger collaborations and networks, or by defining and improving interfaces between the various libraries and tools involved, such as the BLHA2 interface discussed in this thesis that results in modular design concepts.

Appendices

A Analytic reduction formulae for rank-6 pentagons

The reduction formula for rank-6 pentagon (Eq. (7.31), p. 70) can be transformed into form factors (cf. Eq. (7.8), p. 65). They can be written for $D = 4 - 2\epsilon$ dimensions as follows:

$$
\begin{aligned}
A^{5,6}_{a_1,\ldots,a_6}(S) = (-1 - D) \cdot \Big(& \\
& f_{A56}(a_3, a_4, a_5, a_6, a_1, a_2) + f_{A56}(a_2, a_4, a_5, a_6, a_1, a_3) + f_{A56}(a_2, a_3, a_5, a_6, a_1, a_4) \\
& f_{A56}(a_2, a_3, a_4, a_6, a_1, a_5) + f_{A56}(a_2, a_3, a_4, a_5, a_1, a_6) + f_{A56}(a_1, a_4, a_5, a_6, a_2, a_3) \\
& f_{A56}(a_1, a_3, a_5, a_6, a_2, a_4) + f_{A56}(a_1, a_3, a_4, a_6, a_2, a_5) + f_{A56}(a_1, a_3, a_4, a_5, a_2, a_6) \\
& f_{A56}(a_1, a_2, a_5, a_6, a_3, a_4) + f_{A56}(a_1, a_2, a_4, a_6, a_3, a_5) + f_{A56}(a_1, a_2, a_4, a_5, a_3, a_6) \\
& f_{A56}(a_1, a_2, a_3, a_6, a_4, a_5) + f_{A56}(a_1, a_2, a_3, a_5, a_4, a_6) + f_{A56}(a_1, a_2, a_3, a_4, a_5, a_6)\Big) \\
+ \frac{1}{6}\Big(& g_{A56}(a_2, a_3, a_4, a_5, a_6, a_1) + g_{A56}(a_1, a_3, a_4, a_5, a_6, a_2) \\
& + g_{A56}(a_1, a_2, a_4, a_5, a_6, a_3) + g_{A56}(a_1, a_2, a_3, a_5, a_6, a_4) \\
& + g_{A56}(a_1, a_2, a_3, a_4, a_6, a_5) + g_{A56}(a_1, a_2, a_3, a_4, a_5, a_6)\Big)
\end{aligned}
\tag{A.1}
$$

with

$$
f_{A56}(a_1, \ldots, a_6) = \frac{1}{15} \sum_{j \in S} \left(b_j \mathcal{S}^{-1}_{a_5 a_6} - \frac{1}{2} b_{a_5} \mathcal{S}^{-1}_{a_6 j} - \frac{1}{2} b_{a_6} \mathcal{S}^{-1}_{a_5 j} \right) I^{D+2,4}_4(a_1, \ldots, a_4; S \setminus \{j\})
\tag{A.2}
$$

$$
g_{A56}(a_1, \ldots, a_6) = \sum_{j \in S} \mathcal{S}^{-1}_{j a_6} I^{D,5}_4(a_1, \ldots, a_5; S \setminus \{j\}).
\tag{A.3}
$$

The modified Cayley matrix S is defined in Eq. (7.5), p. 64, $b_i(S) = \sum_{k \in S} \mathcal{S}^{-1}_{ki}$. It is assumed here that the four-point integrals $I^{D+2,4}_4$ and $I^{D,5}_4$ are already fully symmetrized, therefore in Eq. (A.1), f_{A56} needs only be symmetrized over its last two parameters

and g_{A56} over its last parameter [1].

The form factor $B^{5,4}$ for the rank-6 pentagon belonging to one power of $g^{\mu\nu}$ is

$$
\begin{aligned}
B^{5,4}_{a_1,\dots,a_4}(S) =&(-1-D)\cdot\Big(\big(\sum_{j\in S}\frac{1}{30}b_j I_4^{D,4}(a_1,\dots,a_4;S\setminus\{j\})\big)\\
&+f_{B54}(a_3,a_4,a_1,a_2)+f_{B54}(a_2,a_4,a_1,a_3)+f_{B54}(a_2,a_3,a_1,a_4)\\
&+f_{B54}(a_1,a_4,a_2,a_3)+f_{B54}(a_1,a_3,a_2,a_4)+f_{B54}(a_1,a_2,a_3,a_4)\big)\\
&+\frac{1}{6}\big(g_{B54}(a_2,a_3,a_4,a_1)+g_{B54}(a_1,a_3,a_4,a_2)\\
&+g_{B54}(a_1,a_2,a_4,a_3)+g_{B54}(a_1,a_2,a_3,a_4)\big)\\
&-\frac{1}{60B}\big(h_{B54}(a_3,a_4,a_1,a_2)+h_{B54}(a_2,a_4,a_1,a_3)+h_{B54}(a_2,a_3,a_1,a_4)\\
&+h_{B54}(a_1,a_4,a_2,a_3)+h_{B54}(a_1,a_3,a_2,a_4)+h_{B54}(a_1,a_2,a_3,a_4)\big)
\end{aligned}
$$

$$(A.4)$$

with

$$
f_{B54}(a_1,\dots,a_4) = \sum_{j\in S}-\frac{1}{30}\Big(b_j\mathcal{S}^{-1}_{a_3 a_4}+b_{a_3}\mathcal{S}^{-1}_{a_4 j}+b_{a_4}\mathcal{S}^{-1}_{a_3 j}\Big)I_4^{D+4}(a_1,a_2;S\setminus\{j\}) \quad (A.5)
$$

$$
g_{B54}(a_1,\dots,a_4) = -\frac{1}{2}\sum_{j\in S}\mathcal{S}^{-1}_{a_4 j}I_4^{D+2,3}(a_1,a_2,a_3;S\setminus\{j\}) \tag{A.6}
$$

$$
\begin{aligned}
h_{B54}(a_1,\dots,a_4) = \sum_{j\in S}&\Big(b_j\mathcal{S}^{-1}_{a_1 a_2}b_{a_4}-\frac{1}{2}b_{a_1}\mathcal{S}^{-1}_{j a_2}b_{a_4}-\frac{1}{2}b_{a_2}\mathcal{S}^{-1}_{j a_1}b_{a_4}\Big)I_4^{D+4,1}(a_3;S\setminus\{j\})\\
&+\Big(b_j\mathcal{S}^{-1}_{a_1 a_2}b_{a_3}-\frac{1}{2}b_{a_1}\mathcal{S}^{-1}_{j a_2}b_{a_3}-\frac{1}{2}b_{a_2}\mathcal{S}^{-1}_{j a_1}b_{a_3}\Big)I_4^{D+4,1}(a_4;S\setminus\{j\}).
\end{aligned}
$$

$$(A.7)$$

---

[1] The order of the first four or five parameters respectively is therefore arbitrary.

The form factor belonging to two powers of $g^{\mu\nu}$ can be written as

$$
\begin{aligned}
C^{5,2}_{a_1, a_2}(S) =(-1-D)\Bigg(& \sum_{j \in S} -\frac{1}{30} b_j I_4^{D+4,2}(a_1, a_2; S \setminus \{j\}) \\
& + \frac{1}{60}\left(b_j S^{-1}_{a_1 a_2} - \frac{1}{2} b_{a_1} S^{-1}_{a_2 j} - \frac{1}{2} b_{a_2} S^{-1}_{a_1 j}\right) I_4^{D+6}(S \setminus \{j\})\Bigg) \\
& - \frac{1}{24} \sum_{j \in S}\left(S^{-1}_{j a_1} I_4^{D+4,1}(a_2, S \setminus \{j\}) + S^{-1}_{j a_2} I_4^{D+4,1}(a_1, S \setminus \{j\})\right) \\
& - \frac{1}{120} \sum_{j \in S}\left(b_j b_{a_1} I_4^{D+4,1}(a_2, S \setminus \{j\}) + b_j b_{a_2} I_4^{D+4,1}(a_1, S \setminus \{j\})\right)
\end{aligned}
\tag{A.8}
$$

and finally for three powers of $g^{\mu\nu}$,

$$
D^{5,0}(S) = \frac{(-1-D)}{40} \sum_{j \in S} b_j I_4^{D+6}(S \setminus \{j\}).
\tag{A.9}
$$

B Feynman rules for the effective $ggWW$ vertices

The dimensional-8 operators described in Eqs. (9.1) to (9.3) of Section 9.2, p. 84 introduce new vertices mediating between gluons and electroweak vector bosons. For the new $ggWW$ vertices, which are analyzed in Chapter 9, p. 81, the Feynman rules are listed below where all momenta are assumed to be incoming.
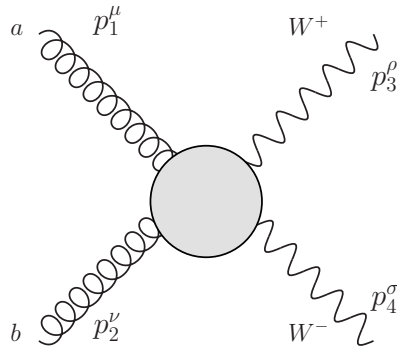
$$O_1: \quad 16\mathrm{i}\frac{c_1}{\Lambda^4}\delta^{a,b}\left(p_1^\nu p_2^\mu - g^{\mu\nu}p_1\cdot p_2\right)\left(p_3^\sigma p_4^\rho - g^{\rho\sigma}p_3\cdot p_4\right)$$

$$O_2: \quad 16\mathrm{i}\frac{c_2}{\Lambda^4}\delta^{a,b}\epsilon^{\mu\nu p_1 p_2}\left(p_4^\rho p_3^\sigma - g^{\rho\sigma}p_3\cdot p_4\right)$$

$$O_3: \quad 16\mathrm{i}\frac{c_3}{\Lambda^4}\delta^{a,b}\epsilon^{\rho\sigma p_3 p_4}\left(p_1^\nu p_2^\mu - g^{\mu\nu}p_1\cdot p_2\right)$$

C Feynman diagrams

The Feynman diagrams for the process $pp/gg\ (\to W^+W^-) \to e^+\nu_e\,\mu^-\bar{\nu}_\mu$, which is calculated in Chapter 9, p. 81, are listed in this chapter.

C.1 Gluon-gluon loop-induced diagrams
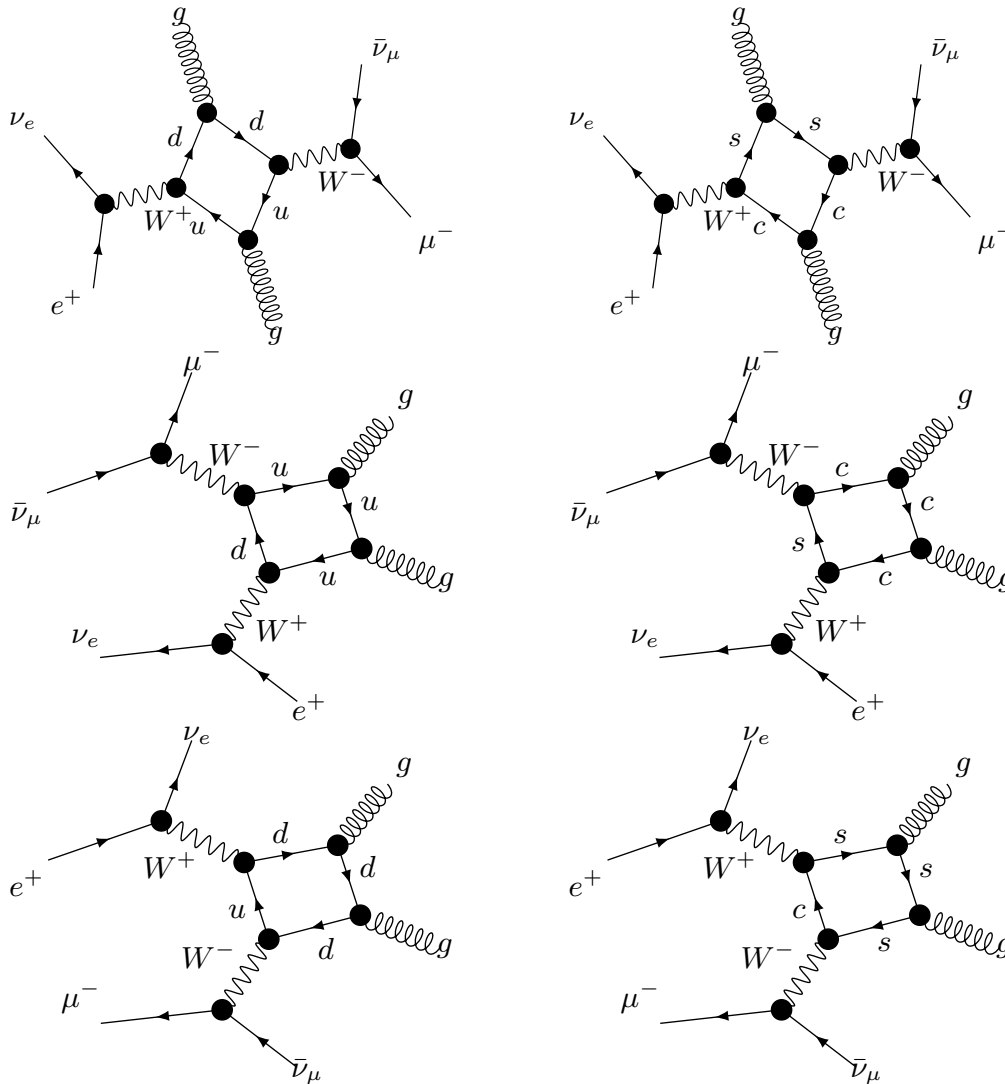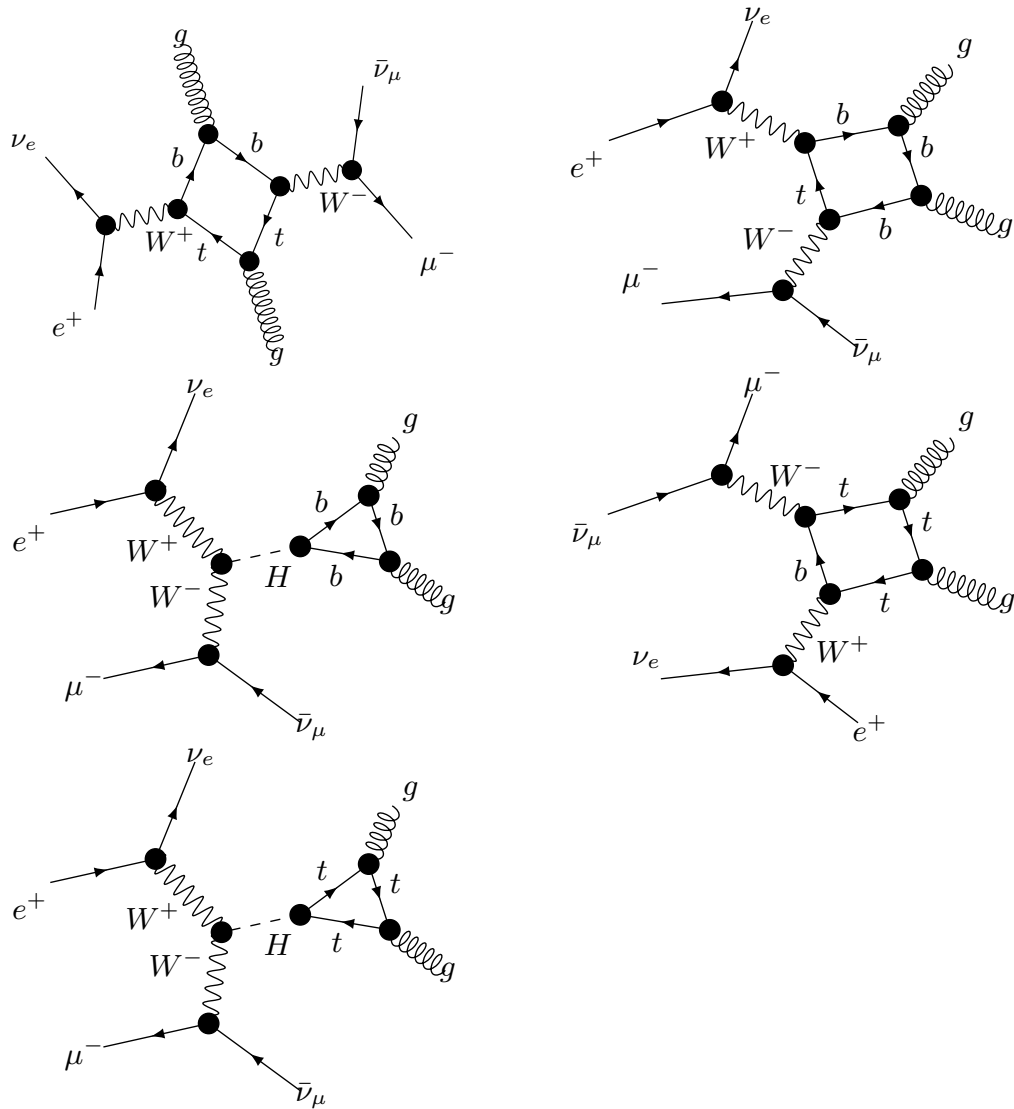
C.2 Quark–antiquark channel

For reasons of brevity, only the Feynman diagrams of the $u\bar{u}$ initial state are listed in the following. Diagrams for the other considered quark-antiquark initial states ($d\bar{d}$, $s\bar{s}$, $c\bar{c}$ and crossings) are analogue. Real-emission diagrams are not shown.

C.2.1 Leading order (Born level) diagrams
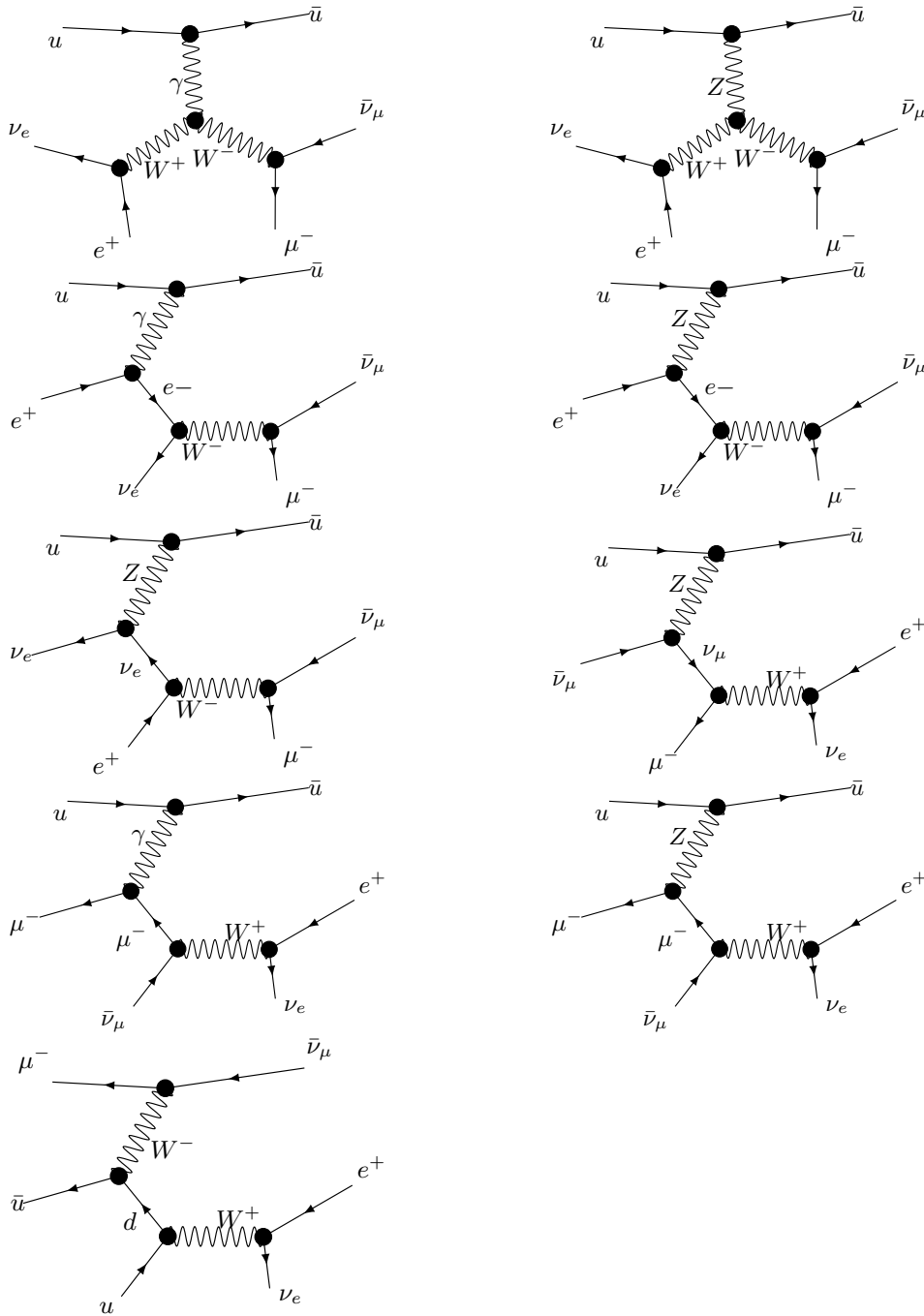
C.2.2 Next-to-leading order diagrams with virtual contributions
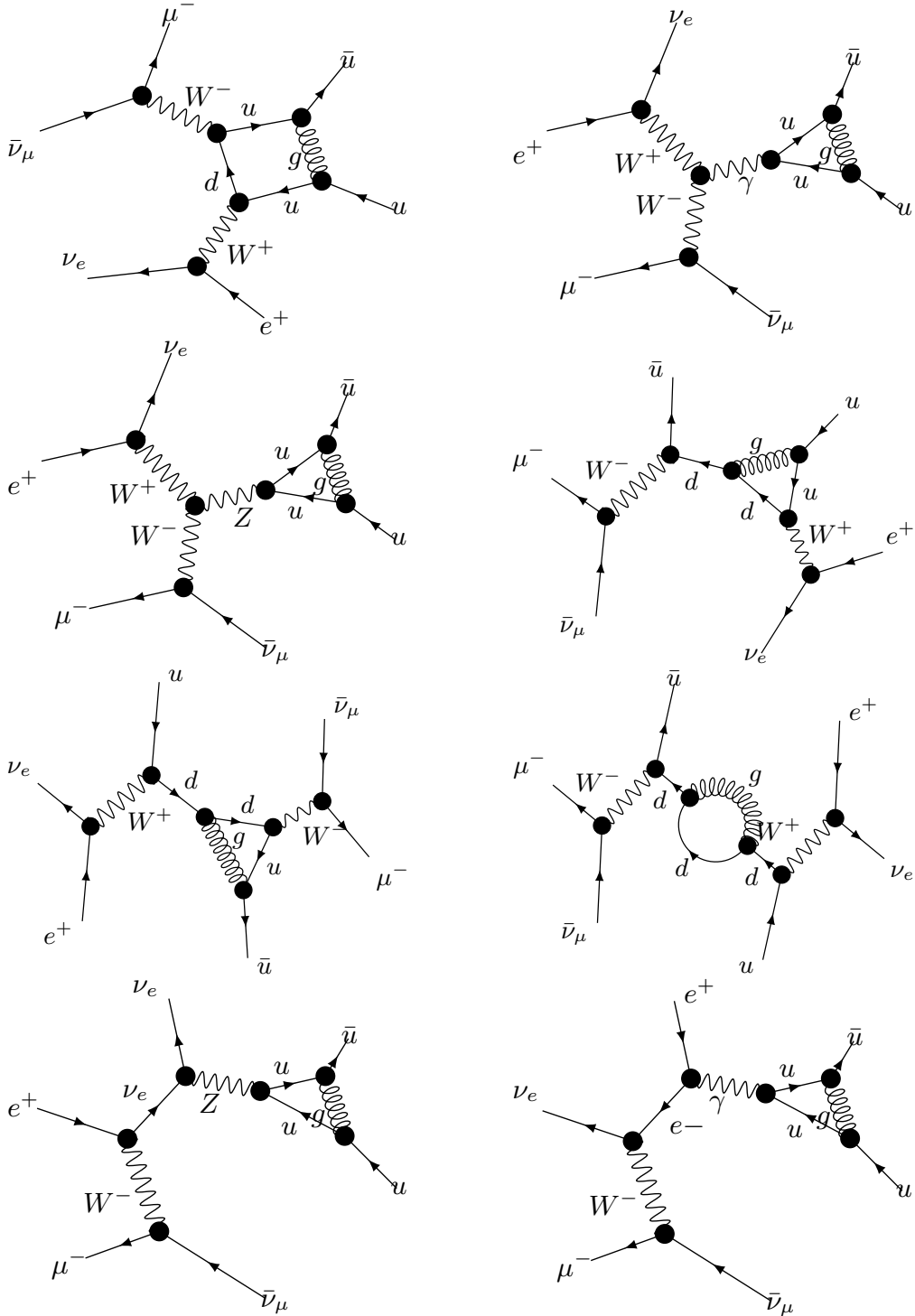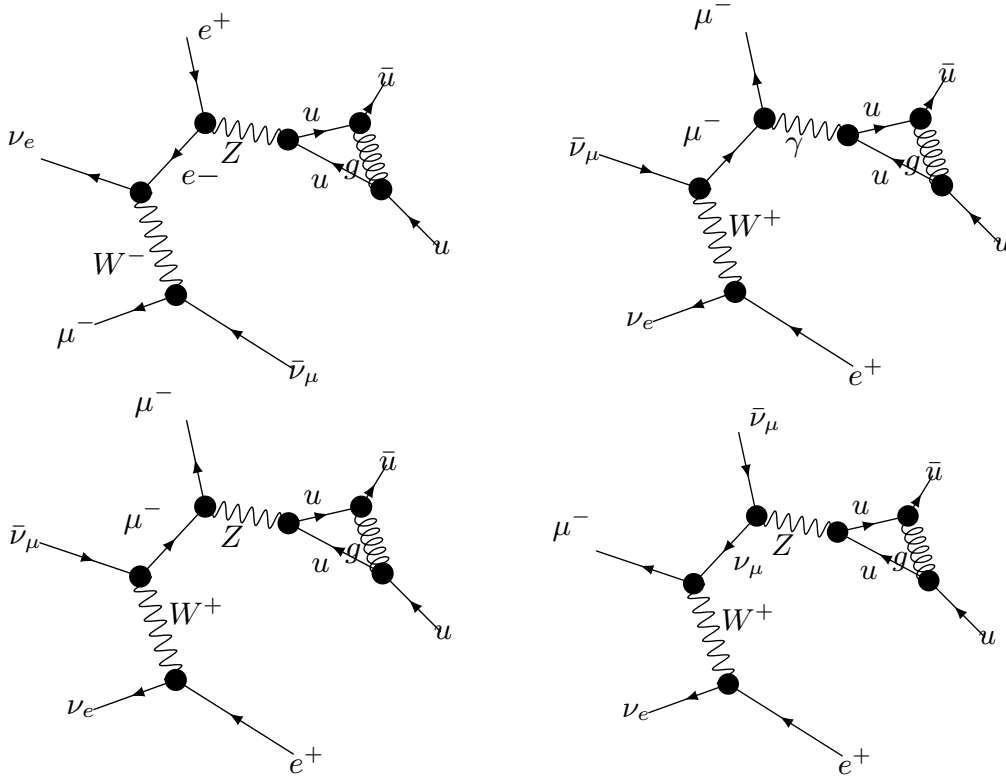
D Input files

In this appendix chapter, input files for the process $gg \to e^+ \nu_e \, \mu^- \bar{\nu}_\mu$ of the calculation in Chapter 9, p. 81 are listed.

Listing D.1: BLHA2 order file for the *gg* calculation including the dim-8 term and interference terms.

```
# OLP order file created by Herwig++/Matchbox for GoSam.


InterfaceVersion BLHA2
MatrixElementSquareType CHsummed
CorrectionType QCD
IRregularisation CDR
MassiveParticles 5 6


AlphasPower 0
AmplitudeType LoopInduced
21 21 -> -14 -11 12 13


AlphasPower 0
AmplitudeType LIEffInterference
21 21 -> -14 -11 12 13


AlphasPower 0
AmplitudeType Tree
21 21 -> -14 -11 12 13
```

Listing D.2: condensed GoSam input file for the *gg* calculation

```
model=FeynRules,./SM_Eff8_UFO/
model.options=c1:0.1,c2:0.1,c3:0.1
qgraf.verbatim=true=bridge[anti11,part11,part13,anti13,\n\
 part15,anti15,part12,anti12,part14,anti14,part16,anti16,\n\
 part22,part23,0,0];
qgraf.verbatim.nlo=true=vsum[NP,0,0];
extensions=autotools
```

```
filter.nlo=lambda d: not (d.loopsize()==3 and d.chord([part1,part2,
    part3,part4,anti1,anti2,anti3,anti4])==3)
symmetries=family,generation
```

E Further plots

In this appendix chapter, complementary distributions of the calculation to pp/gg $(\rightarrow W^+W^-) \rightarrow e^+\nu_e\,\mu^-\bar{\nu}_\mu$ in Chapter 9, p. 81 are shown. The plots are referenced at the relevant positions in Section 9.6, p. 90 and Section 9.7, p. 104.

(a) (b)
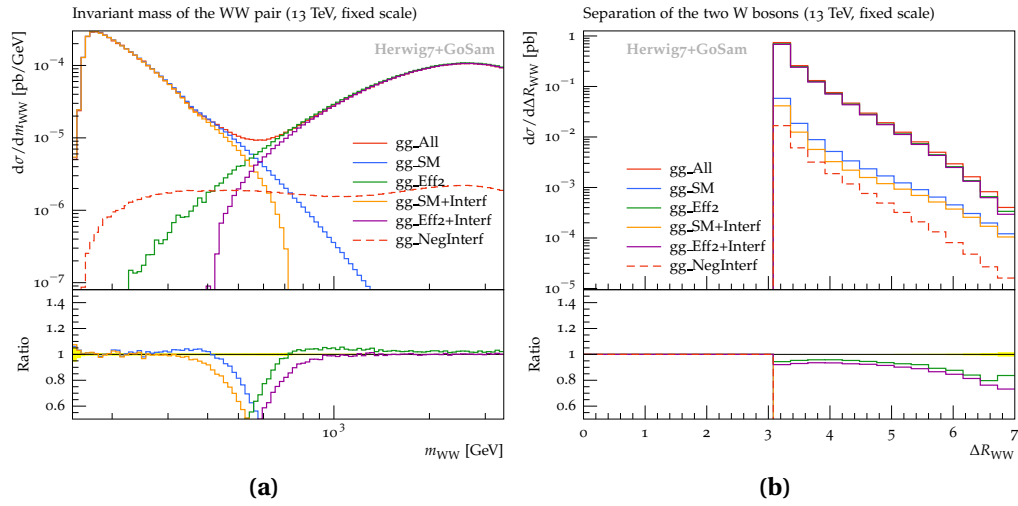
Figure E.1: (a) Invariant mass distribution of the W-boson pair and (b) ΔR_{WW} distribution of gg-initiated SM/BSM contributions at $\sqrt{s} = 13\,\text{TeV}$ (*fixed scale*).
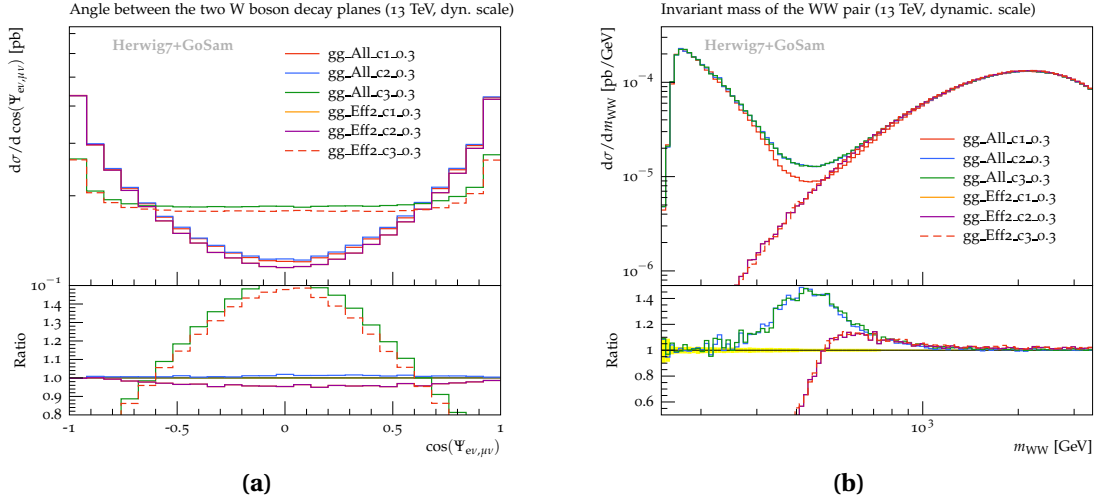
Figure E.2: For the operators O_1, O_2, O_3, the distribution of (a) the angle between the W-boson decay planes and (b) the invariant mass of the W-boson pair are shown for the *dynamic* scale at $\sqrt{s} = 13$ TeV. The ratio plots are with respect to gg_All_c1_0.3 ($c_1 = 0.3$, $c_2 = c_3 = 0$).
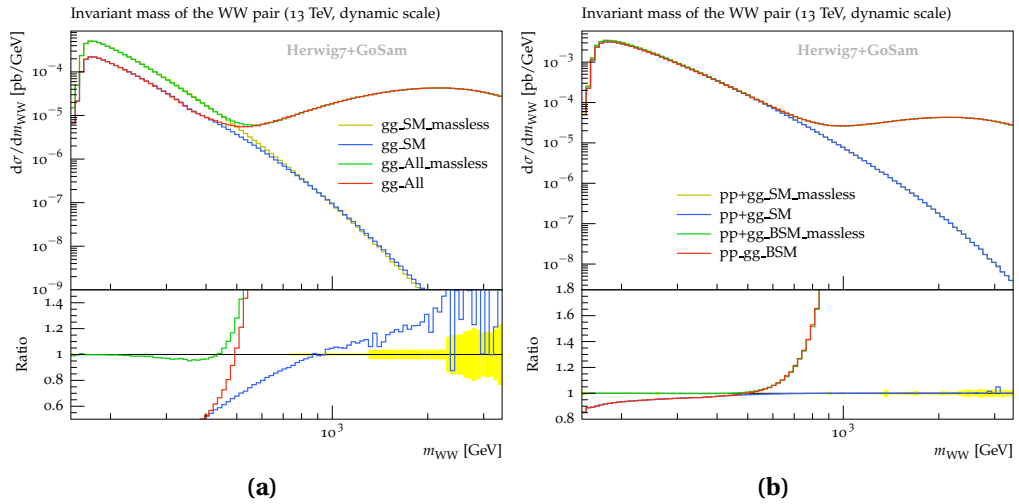
Figure E.3: Effects of assuming the third quark-generation to be massless in the (a) gluon-gluon and (b) combined channel.
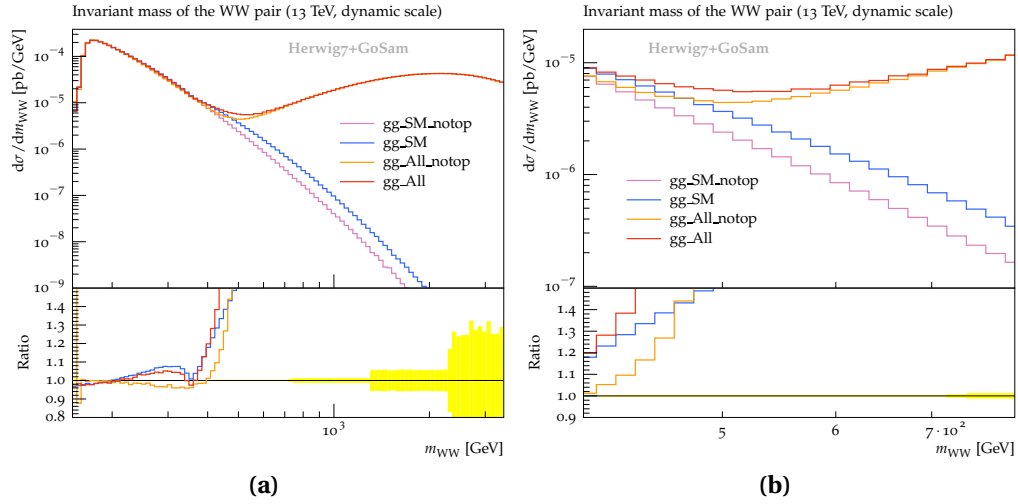
Figure E.4: Effects of assuming the third quark-generation as massless in the m_{WW} distribution; the interesting region of (a) is shown in (b).
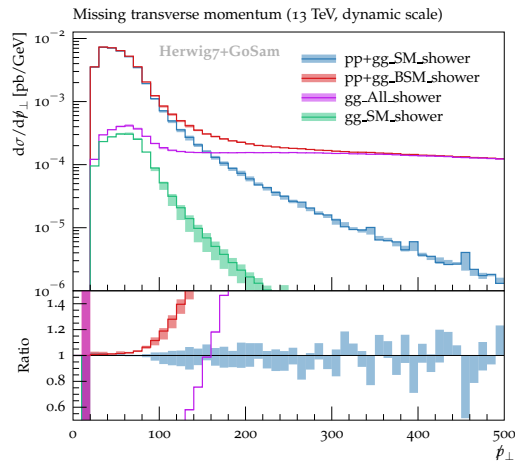
Figure E.5: Missing momentum distribution in the final state for low momentum. The bands show variation of the shower scale μ_Q by factor two.

Acronyms and abbreviations

BLHA Binoth Les Houches Accord (pp. 55, 56)

BLHA1 original version of the Binoth Les Houches Accord (pp. 55, 56, 58)

BLHA2 Binoth Les Houches Accord 2 (pp. 16, 46, 55–58, 60, 81, 87, 115–117, 133, 141)

BSM Physics Beyond the Standard Model (pp. 15–17, 26, 27, 30, 46, 55, 61, 94, 98, 106, 108, 115, 117)

CDR conventional dimensional regularization (pp. 37, 38)

CEPC Circular Electron-Positron Collider (p. 117)

χPT Chiral Pertubation Theory (pp. 30, 31)

CLIC Compact Linear Collider (p. 117)

d.o.f. degree of freedom (pp. 25, 38)

DRED dimensional reduction (p. 38)

EFT Effective field theory (pp. 29–31, 63, 81, 90, 91, 107)

EW electroweak (p. 116)

FCC Future Circular Collider (pp. 108, 116, 117)

GUT Grand Unified Theory (p. 28)

HQET Heavy Quark Effective Theory (p. 29)

ILC International Linear Collider (p. 117)

IR infrared, low energy (pp. 29, 36, 37, 47, 67)

LEP Large Electron-Positron Collider (p. 117)

LHA Les Houches Accord (p. 56)

LHC Large Hadron Collider (pp. 15, 17, 27, 82, 98, 108, 110, 115, 116, 143)

LHEF Les Houches Event File (p. 56)

LO leading-order (pp. 35, 40, 92, 106)

MC Monte Carlo program (pp. 40, 43, 44, 55–58, 90, 96, 97, 106, 142)

MSSM Minimal Supersymmetric Standard Model (p. 46)

NLO next-to-leading-order (pp. 16, 17, 32, 35, 82, 83, 89, 98, 115–117)

NNLO next-to-next-to-leading-order (pp. 35, 58, 78, 83, 84, 115)

NRQCD non-relativistic Quantum Chromodynamics (p. 29)

OLP One-Loop provider (pp. 44, 55–58)

PDF parton distribution function (pp. 33–35, 37)

QCD Quantum Chromodynamics (pp. 15, 21, 28, 32, 47, 84, 87, 104, 115, 116)

QED Quantum Electrodynamics (pp. 21, 22, 24)

SCET soft-collinear effective theory (p. 29)

SM Standard Model (pp. 15–17, 19–22, 26–28, 30, 43, 46, 59, 61, 63, 83, 85–87, 89, 90, 94, 95, 98, 99, 101, 106, 108, 109, 115, 116, 141, 145)

SUSY Supersymmetry (p. 27)

't HV 't Hooft-Veltmann scheme (pp. 37, 38)

UFO Universal FeynRules Output (pp. 46, 60)

UV ultraviolet, high energy (pp. 29, 31, 34–37, 67)

VEV vacuum expectation value (pp. 23, 25)

w.l.o.g. without loss of generality (p. 71)

List of Figures

List of Tables

Bibliography

[1] J. Bellm et al. 'Anomalous coupling, top-mass and parton-shower effects in W^+W^- production'. *JHEP* 2016.5 (2016), pp. 1–29. ISSN: 1029-8479. DOI: 10. 1007/JHEP05(2016)106. arXiv: 1602.05141 [hep-ph] (cit. on pp. 3, 43, 81, 86, 107).

[2] G. Cullen et al. 'GoSam-2.0: a tool for automated one-loop calculations within the Standard Model and beyond'. *EPJC* 74.8, 3001 (2014). DOI: 10.1140/epjc/ s10052-014-3001-5. arXiv: 1404.7096 (cit. on pp. 3, 16, 39, 43, 59).

[3] J. P. Guillet, G. Heinrich, J. F. von Soden-Fraunhofen. 'Tools for NLO automation: extension of the golem95C integral library'. *Comput.Phys.Commun.* 185.6 (Dec. 2014), pp. 1828–1834. ISSN: 0010-4655. DOI: 10.1016/j.cpc.2014.03.009. arXiv: 1312.3887 (cit. on pp. 3, 17, 38, 45, 66, 71).

[4] N. Greiner et al. 'NLO QCD corrections to diphoton plus jet production through graviton exchange'. *JHEP* 1311 (Aug. 2013), p. 028. DOI: 10.1007/ JHEP11(2013)028. arXiv: 1308.2194 (cit. on pp. 3, 17, 43, 81).

[5] H. van Deurzen et al. 'NLO QCD corrections to the production of Higgs plus two jets at the LHC'. *Phys.Lett.* B721 (Jan. 2013), pp. 74–81. DOI: 10.1016/j. physletb.2013.02.051. arXiv: 1301.0493 (cit. on pp. 3, 4, 17, 43).

[6] J. Bellm et al. 'GoSam plus Herwig++/Matchbox'. In: *Les Houches 2013: Physics at TeV Colliders Standard Model Working Group Report*. 2014. arXiv: 1405.1067 (cit. on pp. 3, 44, 56).

[7] J. F. von Soden-Fraunhofen. 'GoSam 2.0: a tool for automated one-loop calculations'. *J. Phys. Conf. Ser.* 608.1 (2015), p. 012061. DOI: 10.1088/1742-6596/ 608/1/012061. arXiv: 1409.8526 [hep-ph] (cit. on p. 3).

[8] S. Alioli et al. 'Update of the Binoth Les Houches Accord for a standard interface between Monte Carlo tools and one-loop programs'. *Comput.Phys.Commun.* 185 (2014), pp. 560–571. DOI: 10.1016/j.cpc.2013.10. 020. arXiv: 1308.3462 [hep-ph] (cit. on pp. 3, 16, 46, 55, 57, 115).

[9]   G. Cullen et al. 'GoSam applications for automated NLO calculations'. *J. Phys. Conf. Ser.* 523 (2014), p. 012056. DOI: 10.1088/1742-6596/523/1/012056. arXiv: 1309.3741 [hep-ph] (cit. on pp. 3, 4).

[10] G. Cullen et al. 'NLO QCD Production of Higgs plus jets with GoSam'. *PoS* EPS-HEP2013 (2013), p. 446. arXiv: 1311.5191 [hep-ph] (cit. on pp. 3, 4).

[11] G. Cullen et al. 'GoSam @ LHC: algorithms and applications to Higgs production'. *PoS* RADCOR2013 (2013), p. 029. arXiv: 1312.1761 [hep-ph] (cit. on pp. 3, 4).

[12] J. R. Andersen et al. 'Handbook of LHC Higgs Cross Sections: 3. Higgs Properties' (2013). Ed. by S. Heinemeyer et al. DOI: 10.5170/CERN-2013-004. arXiv: 1307.1347 [hep-ph] (cit. on pp. 3, 4).

[13] L. Evans, P. Bryant. 'LHC Machine'. *JINST* 3 (2008), S08001. DOI: 10.1088/1748-0221/3/08/S08001 (cit. on p. 15).

[14] ATLAS Collaboration. 'The ATLAS Experiment at the CERN Large Hadron Collider'. *JINST* 3 (2008), S08003. DOI: 10.1088/1748-0221/3/08/S08003 (cit. on p. 15).

[15] S. Chatrchyan et al. 'The CMS experiment at the CERN LHC'. *JINST* 3 (2008), S08004. DOI: 10.1088/1748-0221/3/08/S08004 (cit. on p. 15).

[16] ATLAS Collaboration. 'Observation of a new particle in the search for the Standard Model Higgs boson with the ATLAS detector at the LHC'. *Phys.Lett.* B716 (July 2012), pp. 1–29. DOI: 10.1016/j.physletb.2012.08.020. arXiv: 1207.7214 (cit. on pp. 15, 24).

[17] CMS Collaboration. 'Observation of a new boson at a mass of 125 GeV with the CMS experiment at the LHC'. *Phys. Lett. B* 716 (July 2012), p. 30. arXiv: 1207.7235 (cit. on pp. 15, 24).

[18] S. Chatrchyan et al. 'Observation of a new boson with mass near 125 GeV in pp collisions at $\sqrt{s}$ = 7 and 8 TeV'. *JHEP* 06 (2013), p. 081. DOI: 10.1007/JHEP06(2013)081. arXiv: 1303.4571 [hep-ex] (cit. on p. 15).

[19] ATLAS Collaboration. 'Measurement of the Higgs boson mass from the $H \rightarrow \gamma\gamma$ and $H \rightarrow ZZ^* \rightarrow 4\ell$ channels with the ATLAS detector using 25 fb^{-1} of pp collision data'. *Phys. Rev.* D90.5 (2014), p. 052004. DOI: 10.1103/PhysRevD.90.052004. arXiv: 1406.3827 [hep-ex] (cit. on p. 15).

[20]   V. Khachatryan et al. 'Precise determination of the mass of the Higgs boson and tests of compatibility of its couplings with the standard model predictions using proton collisions at 7 and 8 TeV'. *Eur. Phys. J.* C75.5 (2015), p. 212. DOI: `10.1140/epjc/s10052-015-3351-7`. arXiv: `1412.8662 [hep-ex]` (cit. on p. 15).

[21]   ATLAS collaboration. 'Study of the spin properties of the Higgs-like particle in the $H \rightarrow WW^{(*)} \rightarrow e\nu\mu\nu$ channel with 21 fb^{-1} of $\sqrt{s}$ = 8 TeV data collected with the ATLAS detector.' ATLAS-CONF-2013-031 (2013) (cit. on p. 15).

[22]   S. Chatrchyan et al. 'Measurement of the properties of a Higgs boson in the four-lepton final state'. *Phys. Rev.* D89.9 (2014), p. 092007. DOI: `10.1103/PhysRevD.89.092007`. arXiv: `1312.5353 [hep-ex]` (cit. on p. 15).

[23]   M. Gell-Mann. 'A Schematic Model of Baryons and Mesons'. *Phys. Lett.* 8 (1964), pp. 214–215. DOI: `10.1016/S0031-9163(64)92001-3` (cit. on p. 15).

[24]   G. Zweig. 'An SU(3) model for strong interaction symmetry and its breaking. Version 2'. In: *DEVELOPMENTS IN THE QUARK THEORY OF HADRONS. VOL. 1. 1964 - 1978.* Ed. by D. Lichtenberg, S. P. Rosen. 1964, pp. 22–101. `http://inspirehep.net/record/4674/files/cern-th-412.pdf` (cit. on p. 15).

[25]   H. Fritzsch, M. Gell-Mann, H. Leutwyler. 'Advantages of the Color Octet Gluon Picture'. *Phys. Lett.* B47 (1973), pp. 365–368. DOI: `10.1016/0370-2693(73)90625-4` (cit. on p. 15).

[26]   D. J. Gross, F. Wilczek. 'Ultraviolet Behavior of Nonabelian Gauge Theories'. *Phys. Rev. Lett.* 30 (1973), pp. 1343–1346. DOI: `10.1103/PhysRevLett.30.1343` (cit. on pp. 15, 22).

[27]   H. D. Politzer. 'Reliable Perturbative Results for Strong Interactions?' *Phys. Rev. Lett.* 30 (1973), pp. 1346–1349. DOI: `10.1103/PhysRevLett.30.1346` (cit. on pp. 15, 22).

[28]   S. L. Glashow. 'Partial Symmetries of Weak Interactions'. *Nucl. Phys.* 22 (1961), pp. 579–588. DOI: `10.1016/0029-5582(61)90469-2` (cit. on p. 15).

[29]   S. Weinberg. 'A Model of Leptons'. *Phys. Rev. Lett.* 19 (1967), pp. 1264–1266. DOI: `10.1103/PhysRevLett.19.1264` (cit. on p. 15).

[30]   A. Salam. 'Weak and Electromagnetic Interactions'. *Conf. Proc.* C680519 (1968), pp. 367–377 (cit. on p. 15).

[31]   S. L. Glashow, J. Iliopoulos, L. Maiani. 'Weak Interactions with Lepton-Hadron Symmetry'. *Phys. Rev.* D2 (1970), pp. 1285–1292. DOI: `10.1103/PhysRevD.2.1285` (cit. on p. 15).

[32]   F. Englert, R. Brout. 'Broken Symmetry and the Mass of Gauge Vector Mesons'. *Phys. Rev. Lett.* 13 (1964), pp. 321–323. DOI: 10.1103/PhysRevLett.13.321 (cit. on p. 15).

[33]   P. W. Higgs. 'Broken symmetries, massless particles and gauge fields'. *Phys. Lett.* 12 (1964), pp. 132–133. DOI: 10.1016/0031-9163(64)91136-9 (cit. on p. 15).

[34]   P. W. Higgs. 'Broken Symmetries and the Masses of Gauge Bosons'. *Phys. Rev. Lett.* 13 (1964), pp. 508–509. DOI: 10.1103/PhysRevLett.13.508 (cit. on p. 15).

[35]   G. S. Guralnik, C. R. Hagen, T. W. B. Kibble. 'Global Conservation Laws and Massless Particles'. *Phys. Rev. Lett.* 13 (1964), pp. 585–587. DOI: 10.1103/PhysRevLett.13.585 (cit. on p. 15).

[36]   P. W. Higgs. 'Spontaneous Symmetry Breakdown without Massless Bosons'. *Phys. Rev.* 145 (1966), pp. 1156–1163. DOI: 10.1103/PhysRev.145.1156 (cit. on p. 15).

[37]   T. W. B. Kibble. 'Symmetry breaking in nonAbelian gauge theories'. *Phys. Rev.* 155 (1967), pp. 1554–1561. DOI: 10.1103/PhysRev.155.1554 (cit. on p. 15).

[38]   G. Arnison et al. 'Experimental Observation of Isolated Large Transverse Energy Electrons with Associated Missing Energy at s**(1/2) = 540-GeV'. *Phys. Lett.* B122 (1983). [,611(1983)], pp. 103–116. DOI: 10.1016/0370-2693(83)91177-2 (cit. on p. 15).

[39]   M. Banner et al. 'Observation of Single Isolated Electrons of High Transverse Momentum in Events with Missing Transverse Energy at the CERN anti-p p Collider'. *Phys. Lett.* B122 (1983), pp. 476–485. DOI: 10.1016/0370-2693(83)91605-2 (cit. on p. 15).

[40]   G. Arnison et al. 'Experimental Observation of Lepton Pairs of Invariant Mass Around 95-GeV/c**2 at the CERN SPS Collider'. *Phys. Lett.* B126 (1983), pp. 398–410. DOI: 10.1016/0370-2693(83)90188-0 (cit. on p. 15).

[41]   P. Bagnaia et al. 'Evidence for Z0 —> e+ e- at the CERN anti-p p Collider'. *Phys. Lett.* B129 (1983), pp. 130–140. DOI: 10.1016/0370-2693(83)90744-X (cit. on p. 15).

[42]   F. Abe et al. 'Observation of top quark production in $\bar{p}p$ collisions'. *Phys. Rev. Lett.* 74 (1995), pp. 2626–2631. DOI: 10.1103/PhysRevLett.74.2626. arXiv: hep-ex/9503002 [hep-ex] (cit. on p. 15).

[43]   S. Abachi et al. 'Observation of the top quark'. *Phys. Rev. Lett.* 74 (1995), pp. 2632–2637. DOI: 10.1103/PhysRevLett.74.2632. arXiv: hep-ex/9503003 [hep-ex] (cit. on p. 15).

[44]   F. Zwicky. 'Die Rotverschiebung von extragalaktischen Nebeln'. *Helv. Phys. Acta* 6 (1933), pp. 110–127 (cit. on pp. 15, 27).

[45]   V. C. Rubin, W. K. Ford Jr. 'Rotation of the Andromeda Nebula from a Spectroscopic Survey of Emission Regions'. *Astrophys. J.* 159 (1970), pp. 379–403. DOI: 10.1086/150317 (cit. on pp. 15, 27).

[46]   J. P. Dietrich et al. 'A filament of dark matter between two clusters of galaxies'. *Nature* (2012). DOI: 10.1038/nature11224. arXiv: 1207.0809 [astro-ph.CO] (cit. on pp. 15, 27).

[47]   H. G. Fargnoli et al. 'Two-loop corrections to $(g-2)_\mu$ in the SM and the MSSM'. In: *Proceedings, 12th DESY Workshop on Elementary Particle Physics: Loops and Legs in Quantum Field Theory (LL2014)*. 2014. arXiv: 1407.1501 [hep-ph] (cit. on pp. 15, 27).

[48]   P. Athron et al. 'GM2Calc: Precise MSSM prediction for $(g-2)$ of the muon' (2015). arXiv: 1510.08071 [hep-ph] (cit. on pp. 15, 27).

[49]   T. Reiter. 'Automated Evaluation of One-Loop Six-Point Processes for the LHC'. PhD thesis. University of Edinburgh, 15th Sept. 2008, p. 232. arXiv: 0903.0947 (cit. on pp. 16, 39, 43, 63, 68).

[50]   G. Cullen et al. 'Automated One-Loop Calculations with GoSam'. *Eur.Phys.J* C72 (2012), p. 1889. DOI: 10.1140/epjc/s10052-012-1889-1. arXiv: 1111.2034 (cit. on pp. 16, 38, 39, 43, 87).

[51]   T. Binoth et al. 'Golem95: a numerical program to calculate one-loop tensor integrals with up to six external legs'. *Comput.Phys.Commun.* 180 (2009), pp. 2317–2330. DOI: 10.1016/j.cpc.2009.06.024. arXiv: 0810.0992 (cit. on pp. 17, 38, 45, 63, 66).

[52]   G. Cullen et al. 'Golem95C: A library for one-loop integrals with complex masses'. *Comput.Phys.Commun.* 182 (Jan. 2011), pp. 2276–2284. DOI: 10.1016/j.cpc.2011.05.015. arXiv: 1101.5595 (cit. on pp. 17, 38, 45, 66).

[53]   P. Mastrolia et al. 'Scattering AMplitudes from Unitarity-based Reduction Algorithm at the Integrand-level'. *JHEP* 1008 (June 2010), p. 080. DOI: 10.1007/JHEP08(2010)080. arXiv: 1006.0710 (cit. on pp. 17, 45, 63, 72).

[54]   H. van Deurzen. 'Associated Higgs Production at NLO with GoSam'. *Acta Phys.Polon.* B44.11 (2013), pp. 2223–2230. DOI: 10.5506/APhysPolB.44.2223 (cit. on pp. 17, 45, 63, 72).

[55]   T. Peraro. 'Ninja: Automated Integrand Reduction via Laurent Expansion for One-Loop Amplitudes' (Mar. 2014). arXiv: 1403.1229 (cit. on pp. 17, 45, 47, 63, 72).

[56] H. van Deurzen et al. 'Multi-leg One-loop Massive Amplitudes from Integrand Reduction via Laurent Expansion' (Dec. 2013). arXiv: 1312.6678 (cit. on pp. 17, 45, 47, 48, 63).

[57] N. Arkani-Hamed, S. Dimopoulos, G. Dvali. 'The Hierarchy Problem and New Dimensions at a Millimeter'. *Phys.Lett.B* 429.3–4 (1998), pp. 263–272. DOI: 10.1016/S0370-2693(98)00466-3. arXiv: hep-ph/9803315 (cit. on pp. 17, 84).

[58] J. Ohnemus. 'An Order α^-s calculation of hadronic W^-W^+ production'. *Phys. Rev.* D44 (1991), pp. 1403–1414. DOI: 10.1103/PhysRevD.44.1403 (cit. on pp. 17, 83).

[59] J. Ohnemus. 'Hadronic ZZ, W^-W^+, and $W^\pm Z$ production with QCD corrections and leptonic decays'. *Phys. Rev.* D50 (1994), pp. 1931–1945. DOI: 10.1103/PhysRevD.50.1931. arXiv: hep-ph/9403331 [hep-ph] (cit. on pp. 17, 83).

[60] S. Frixione. 'A Next-to-leading order calculation of the cross-section for the production of W+ W- pairs in hadronic collisions'. *Nucl. Phys.* B410 (1993), pp. 280–324. DOI: 10.1016/0550-3213(93)90435-R (cit. on pp. 17, 83).

[61] L. J. Dixon, Z. Kunszt, A. Signer. 'Helicity amplitudes for O(alpha-s) production of W^+W^-, $W^\pm Z$, ZZ, $W^\pm\gamma$, or $Z\gamma$ pairs at hadron colliders'. *Nucl. Phys.* B531 (1998), pp. 3–23. DOI: 10.1016/S0550-3213(98)00421-0. arXiv: hep-ph/9803250 [hep-ph] (cit. on pp. 17, 83).

[62] L. J. Dixon, Z. Kunszt, A. Signer. 'Vector boson pair production in hadronic collisions at order α_s : Lepton correlations and anomalous couplings'. *Phys. Rev.* D60 (1999), p. 114037. DOI: 10.1103/PhysRevD.60.114037. arXiv: hep-ph/9907305 [hep-ph] (cit. on pp. 17, 83).

[63] V. Hirschi et al. 'Automated event generation for loop-induced processes'. *JHEP* 10 (July 2015), p. 146. DOI: 10.1007/JHEP10(2015)146. arXiv: 1507.00020 [hep-ph] (cit. on pp. 17, 83).

[64] D. A. Dicus, C. Kao, W. W. Repko. 'Gluon Production of Gauge Bosons'. *Phys. Rev.* D36 (1987), p. 1570. DOI: 10.1103/PhysRevD.36.1570 (cit. on pp. 17, 83).

[65] E. W. N. Glover, J. J. van der Bij. 'VECTOR BOSON PAIR PRODUCTION VIA GLUON FUSION'. *Phys. Lett.* B219 (1989), p. 488. DOI: 10.1016/0370-2693(89)91099-X (cit. on pp. 17, 83).

[66] C. Kao, D. A. Dicus. 'Production of W+ W- from gluon fusion'. *Phys. Rev.* D43 (1991), pp. 1555–1559. DOI: 10.1103/PhysRevD.43.1555 (cit. on pp. 17, 83, 86).

[67] T. Binoth et al. 'Gluon-induced WW background to Higgs boson searches at the LHC'. *JHEP* 03 (2005), p. 065. DOI: 10.1088/1126-6708/2005/03/065. arXiv: hep-ph/0503094 [hep-ph] (cit. on pp. 17, 83).

[68]   T. Binoth et al. 'Gluon-induced W-boson pair production at the LHC'. *JHEP* 12 (2006), p. 046. DOI: 10 . 1088 / 1126 – 6708 / 2006 / 12 / 046. arXiv: hep-ph/0611170 [hep-ph] (cit. on pp. 17, 83).

[69]   F. Cascioli et al. 'Precise Higgs-background predictions: merging NLO QCD and squared quark-loop corrections to four-lepton + 0,1 jet production'. *JHEP* 01 (2014), p. 046. DOI: 10.1007/JHEP01(2014)046. arXiv: 1309.0500 [hep-ph] (cit. on pp. 17, 83).

[70]   J. M. Campbell, R. K. Ellis. 'An Update on vector boson pair production at hadron colliders'. *Phys. Rev.* D60 (1999), p. 113006. DOI: 10.1103/PhysRevD. 60.113006. arXiv: hep-ph/9905386 [hep-ph] (cit. on pp. 17, 83).

[71]   J. M. Campbell, R. K. Ellis, C. Williams. 'Vector boson pair production at the LHC'. *JHEP* 1107:018,2011 (May 2011). arXiv: 1105.0020 (cit. on pp. 17, 83, 90, 103).

[72]   J. M. Campbell, R. K. Ellis, C. Williams. 'Gluon-Gluon Contributions to W+ W- Production and Higgs Interference Effects'. *JHEP* 10 (2011), p. 005. DOI: 10.1007/JHEP10(2011)005. arXiv: 1107.5569 [hep-ph] (cit. on pp. 17, 39, 83, 90, 99).

[73]   T. Gehrmann et al. 'W^+W^- Production at Hadron Colliders in Next to Next to Leading Order QCD'. *Phys. Rev. Lett.* 113.21 (2014), p. 212001. DOI: 10.1103/ PhysRevLett.113.212001. arXiv: 1408.5243 [hep-ph] (cit. on pp. 17, 83).

[74]   F. Caola et al. 'QCD Corrections to W^+W^- Production through Gluon Fusion'. *Physics Letters B* 754 (2016), pp. 275–280. ISSN: 0370-2693. DOI: 10 . 1016 / j . physletb.2016.01.046. arXiv: 1511.08617 [hep-ph] (cit. on pp. 17, 83).

[75]   P. Meade, H. Ramani, M. Zeng. 'Transverse momentum resummation effects in W^+W^- measurements'. *Phys. Rev.* D90.11 (2014), p. 114006. DOI: 10.1103/ PhysRevD.90.114006. arXiv: 1407.4481 [hep-ph] (cit. on pp. 17, 83).

[76]   I. Moult, I. W. Stewart. 'Jet Vetoes interfering with $H \rightarrow WW$'. *JHEP* 09 (2014), p. 129. DOI: 10.1007/JHEP09(2014)129. arXiv: 1405.5534 [hep-ph] (cit. on pp. 17, 83).

[77]   P. Jaiswal, T. Okui. 'Explanation of the WW excess at the LHC by jet-veto resummation'. *Phys. Rev.* D90.7 (2014), p. 073009. DOI: 10.1103/PhysRevD.90. 073009. arXiv: 1407.4537 [hep-ph] (cit. on pp. 17, 83).

[78]   P. F. Monni, G. Zanderighi. 'On the excess in the inclusive $W^+W^- \rightarrow l^+l^-\nu\bar{\nu}$ cross section'. *JHEP* 05 (2015), p. 013. DOI: 10.1007/JHEP05(2015)013. arXiv: 1410.4745 [hep-ph] (cit. on pp. 17, 83).

[79] P. Jaiswal, P. Meade, H. Ramani. 'Precision diboson measurements and the interplay of pT and jet-veto resummations' (2015). arXiv: `1509.07118` [`hep-ph`] (cit. on pp. 17, 83).

[80] M. Billoni et al. 'Next-to-leading order electroweak corrections to pp -> W+W- -> 4 leptons at the LHC in double-pole approximation'. *JHEP* 12 (2013), p. 043. DOI: `10.1007/JHEP12(2013)043`. arXiv: `1310.1564` [`hep-ph`] (cit. on pp. 17, 84).

[81] A. Bierweiler. 'Elektroschwache Korrekturen zur Eichboson-Paarproduktion am LHC'. PhD thesis. KIT, Karlsruhe, 2014. `http://nbn-resolving.org/urn:nbn:de:swb:90-411600` (cit. on pp. 17, 84).

[82] A. Falkowski et al. 'Triple Gauge Couplings at LEP revisited'. In: *Les Houches 2013: Physics at TeV Colliders: New Physics Working Group Report*. 2014. arXiv: `1405.1617` [`hep-ph`] (cit. on pp. 17, 84).

[83] J. Ellis, V. Sanz, T. You. 'The Effective Standard Model after LHC Run I'. *JHEP* 03 (2015), p. 157. DOI: `10.1007/JHEP03(2015)157`. arXiv: `1410.7703` [`hep-ph`] (cit. on pp. 17, 84).

[84] A. Falkowski. 'Effective field theory approach to LHC Higgs data' (2015). arXiv: `1505.00046` [`hep-ph`] (cit. on pp. 17, 84).

[85] V. Khachatryan et al. 'Measurements of the Z Z production cross sections in the 2l2ν channel in proton–proton collisions at $\sqrt{s}$ = 7 and 8 TeV and combined constraints on triple gauge couplings'. *Eur. Phys. J.* C75.10 (2015), p. 511. DOI: `10.1140/epjc/s10052-015-3706-0`. arXiv: `1503.05467` [`hep-ex`] (cit. on pp. 17, 84).

[86] ATLAS Collaboration. 'Measurement of the $WW + WZ$ cross section and limits on anomalous triple gauge couplings using final states with one lepton, missing transverse momentum, and two jets with the ATLAS detector at $\sqrt{s}$ = 7 TeV'. *JHEP* 01 (2015), p. 049. DOI: `10.1007/JHEP01(2015)049`. arXiv: `1410.7238` [`hep-ex`] (cit. on pp. 17, 82, 84).

[87] V. Khachatryan et al. 'Measurement of the W^+W^- cross section in pp collisions at $\sqrt{s}$ = 8 TeV and limits on anomalous gauge couplings' (2015). arXiv: `1507.03268` [`hep-ex`] (cit. on pp. 17, 84).

[88] V. Khachatryan et al. 'Combined search for anomalous pseudoscalar HVV couplings in VH production and H to VV decay'. *Submitted to: Phys. Lett. B* (2016). arXiv: `1602.04305` [`hep-ex`] (cit. on pp. 17, 84).

[89] J. C. Romao, J. P. Silva. 'A resource for signs and Feynman diagrams of the Standard Model'. *Int. J. Mod. Phys.* A27 (2012), p. 1230025. DOI: `10.1142/S0217751X12300256`. arXiv: `1209.6213` [`hep-ph`] (cit. on p. 20).

[90] K. Kisamori et al. 'Candidate Resonant Tetraneutron State Populated by the He4(He8,Be8) Reaction'. *Phys. Rev. Lett.* 116.5 (2016), p. 052501. DOI: 10.1103/PhysRevLett.116.052501 (cit. on p. 22).

[91] LHCb Collaboration et al. 'Observation of J/Ψp Resonances Consistent with Pentaquark States in $\Lambda_b^0 \to$ J/ΨK$^-$p Decays'. *Phys. Rev. Lett.* 115 (2015), p. 072001. DOI: 10.1103/PhysRevLett.115.072001. arXiv: 1507.03414 [hep-ex] (cit. on p. 22).

[92] ATLAS Collaboration, CMS Collaboration. 'Combined Measurement of the Higgs Boson Mass in pp Collisions at $\sqrt{s}$ = 7 and 8 TeV with the ATLAS and CMS Experiments'. *Phys. Rev. Lett.* 114 (2015), p. 191803. DOI: 10.1103/PhysRevLett.114.191803. arXiv: 1503.07589 [hep-ex] (cit. on p. 24).

[93] M. Kobayashi, T. Maskawa. 'CP Violation in the Renormalizable Theory of Weak Interaction'. *Prog. Theor. Phys.* 49 (1973), pp. 652–657. DOI: 10.1143/PTP.49.652 (cit. on p. 25).

[94] B. Pontecorvo. 'Mesonium and anti-mesonium'. *Sov. Phys. JETP* 6 (1957). [Zh. Eksp. Teor. Fiz.33,549(1957)], p. 429 (cit. on p. 27).

[95] B. Pontecorvo. 'Neutrino Experiments and the Problem of Conservation of Leptonic Charge'. *Sov. Phys. JETP* 26 (1968). [Zh. Eksp. Teor. Fiz.53,1717(1967)], pp. 984–988 (cit. on p. 27).

[96] M. C. Gonzalez-Garcia, M. Maltoni. 'Phenomenology with Massive Neutrinos'. *Phys. Rept.* 460 (2008), pp. 1–129. DOI: 10.1016/j.physrep.2007.12.004. arXiv: 0704.1800 [hep-ph] (cit. on p. 27).

[97] M. C. Gonzalez-Garcia, M. Maltoni, T. Schwetz. 'Global Analyses of Neutrino Oscillation Experiments' (2015). arXiv: 1512.06856 [hep-ph] (cit. on p. 27).

[98] J. A. Aguilar-Saavedra et al. 'Asymmetries in top quark pair production at hadron colliders'. *Rev. Mod. Phys.* 87 (2015), pp. 421–455. DOI: 10.1103/RevModPhys.87.421. arXiv: 1406.1798 [hep-ph] (cit. on p. 27).

[99] C. W. Murphy. 'Bottom-Quark Forward-Backward and Charge Asymmetries at Hadron Colliders'. *Phys. Rev.* D92.5 (2015), p. 054003. DOI: 10.1103/PhysRevD.92.054003. arXiv: 1504.02493 [hep-ph] (cit. on p. 27).

[100] ATLAS Collaboration. *Search for resonances decaying to photon pairs in 3.2 fb^{-1} of pp collisions at $\sqrt{s}$ = 13 TeV with the ATLAS detector.* Tech. rep. ATLAS-CONF-2015-081. CERN, 2015. http://cds.cern.ch/record/2114853 (cit. on p. 27).

[101] C. Collaboration. 'Search for new physics in high mass diphoton events in proton-proton collisions at 13TeV' (2015) (cit. on p. 27).

[102]   A. D. Sakharov. 'Violation of CP Invariance, c Asymmetry, and Baryon Asymmetry of the Universe'. *Pisma Zh. Eksp. Teor. Fiz.* 5 (1967). [Usp. Fiz. Nauk161,61(1991)], pp. 32–35. DOI: 10.1070/PU1991v034n05ABEH002497 (cit. on p. 27).

[103]   R. D. Peccei, H. R. Quinn. 'CP Conservation in the Presence of Pseudoparticles'. *Phys. Rev. Lett.* 38 (1977), pp. 1440–1443. DOI: 10.1103/PhysRevLett.38.1440 (cit. on p. 28).

[104]   R. D. Peccei, H. R. Quinn. 'Constraints imposed by CP conservation in the presence of pseudoparticles'. *Phys. Rev.* D16 (1977), pp. 1791–1797. DOI: 10.1103/PhysRevD.16.1791 (cit. on p. 28).

[105]   J. E. Kim, G. Carosi. 'Axions and the Strong CP Problem'. *Rev. Mod. Phys.* 82 (2010), pp. 557–602. DOI: 10.1103/RevModPhys.82.557. arXiv: 0807.3125 [hep-ph] (cit. on p. 28).

[106]   W. Skiba. 'TASI Lectures on Effective Field Theory and Precision Electroweak Measurements' (June 2010). arXiv: 1006.2142 [hep-ph] (cit. on p. 29).

[107]   I. Z. Rothstein. 'TASI Lectures on Effective Field Theories' (2003). arXiv: hep-ph/0308266 (cit. on p. 29).

[108]   C. W. Bauer, S. Fleming, M. E. Luke. 'Summing Sudakov logarithms in B — > X(s gamma) in effective field theory'. *Phys.Rev.* D63 (2000), p. 014006. DOI: 10.1103/PhysRevD.63.014006. arXiv: hep-ph/0005275 [hep-ph] (cit. on p. 29).

[109]   C. W. Bauer et al. 'An Effective field theory for collinear and soft gluons: Heavy to light decays'. *Phys.Rev.* D63 (2001), p. 114020. DOI: 10.1103/PhysRevD.63.114020. arXiv: hep-ph/0011336 [hep-ph] (cit. on p. 29).

[110]   G. Buchalla, O. Catà, C. Krause. 'On the power counting in effective field theories'. *Phys. Lett.* B731 (2014), pp. 80–86. ISSN: 0370-2693. DOI: http://dx.doi.org/10.1016/j.physletb.2014.02.015. arXiv: 1312.5624. http://www.sciencedirect.com/science/article/pii/S0370269314001063 (cit. on p. 31).

[111]   E. Fermi. 'Versuch einer Theorie der β-Strahlen. I (An attempt of a theory of beta radiation. 1)'. German. *Z. Phys.* 88.3-4 (1934), pp. 161–177. ISSN: 0044-3328. DOI: 10.1007/BF01351864 (cit. on p. 31).

[112]   J. R. Ellis, M. K. Gaillard, D. V. Nanopoulos. 'A Phenomenological Profile of the Higgs Boson'. *Nucl. Phys.* B106 (1976), p. 292. DOI: 10.1016/0550-3213(76)90382-5 (cit. on p. 32).

[113]   M. A. Shifman et al. 'Low-Energy Theorems for Higgs Boson Couplings to Photons'. *Sov. J. Nucl. Phys.* 30 (1979). [Yad. Fiz.30,1368(1979)], pp. 711–716 (cit. on p. 32).

[114]   B. A. Kniehl, M. Spira. 'Low-energy theorems in Higgs physics'. *Z. Phys.* C69 (1995), pp. 77–88. DOI: 10.1007/s002880050007. arXiv: hep-ph/9505225 [hep-ph] (cit. on p. 32).

[115]   A. Djouadi, M. Spira, P. M. Zerwas. 'Production of Higgs bosons in proton colliders: QCD corrections'. *Phys. Lett.* B264 (1991), pp. 440–446. DOI: 10.1016/0370-2693(91)90375-Z (cit. on p. 32).

[116]   J. Grigo, J. Hoff, M. Steinhauser. 'Higgs boson pair production: top quark mass effects at NLO and NNLO'. *Nucl. Phys.* B900 (2015), pp. 412–430. DOI: 10.1016/j.nuclphysb.2015.09.012. arXiv: 1508.00909 [hep-ph] (cit. on p. 32).

[117]   S. Borowka et al. 'Higgs boson pair production in gluon fusion at NLO with full top-quark mass dependence' (2016). arXiv: 1604.06447 [hep-ph] (cit. on p. 32).

[118]   G. T. Bodwin. 'Factorization of the Drell-Yan Cross-Section in Perturbation Theory'. *Phys. Rev.* D31 (1985). [Erratum: Phys. Rev.D34,3932(1986)], p. 2616. DOI: 10.1103/PhysRevD.34.3932,10.1103/PhysRevD.31.2616 (cit. on p. 33).

[119]   J. C. Collins, D. E. Soper, G. F. Sterman. 'Factorization for Short Distance Hadron - Hadron Scattering'. *Nucl. Phys.* B261 (1985), p. 104. DOI: 10.1016/0550-3213(85)90565-6 (cit. on p. 33).

[120]   J. C. Collins, D. E. Soper, G. F. Sterman. 'Soft Gluons and Factorization'. *Nucl. Phys.* B308 (1988), p. 833. DOI: 10.1016/0550-3213(88)90130-7 (cit. on p. 33).

[121]   T. Kinoshita. 'Mass Singularities of Feynman Amplitudes'. *Journal of Mathematical Physics* 3 (July 1962), pp. 650–677. DOI: 10.1063/1.1724268 (cit. on p. 35).

[122]   T. D. Lee, M. Nauenberg. 'Degenerate Systems and Mass Singularities'. *Physical Review* 133 (Mar. 1964), p. 1549. DOI: 10.1103/PhysRev.133.B1549 (cit. on p. 35).

[123]   S. Catani, M. H. Seymour. 'A General Algorithm for Calculating Jet Cross Sections in NLO QCD'. *Nucl.Phys.* B485 (1997). Erratum-ibid.B510(1998)503-504, pp. 291–419. DOI: 10.1016/S0550-3213(96)00589-5. arXiv: hep-ph/9605323 (cit. on pp. 36, 58, 89).

[124]   S. Catani et al. 'The Dipole Formalism for Next-to-Leading Order QCD Calculations with Massive Partons'. *Nucl.Phys.B* 627 (2002), pp. 189–265. arXiv: `hep-ph/0201036` (cit. on p. 36).

[125]   S. Frixione, Z. Kunszt, A. Signer. 'Three-jet cross sections to next-to-leading order'. *Nucl.Phys. B* 467 (1996), pp. 399–442. arXiv: `hep-ph/9512328` (cit. on p. 36).

[126]   S. Frixione. 'A general approach to jet cross sections in QCD'. *Nucl.Phys. B* 507 (1997), pp. 295–314. arXiv: `hep-ph/9706545` (cit. on p. 36).

[127]   D. A. Kosower. 'Antenna Factorization in Strongly-Ordered Limits'. *Phys.Rev.* D71 (2005), p. 045016. DOI: `10.1103/PhysRevD.71.045016`. arXiv: `hep-ph/0311272` (cit. on p. 36).

[128]   A. Daleo, T. Gehrmann, D. Maitre. 'Antenna subtraction with hadronic initial states'. *JHEP* 0704 (2007), p. 016. DOI: `10.1088/1126-6708/2007/04/016`. arXiv: `hep-ph/0612257` (cit. on p. 36).

[129]   A. G.-D. Ridder, M. Ritzmann. 'NLO Antenna Subtraction with Massive Fermions'. *JHEP* 0907 (Apr. 2009), p. 041. DOI: `10.1088/1126-6708/2009/07/041`. arXiv: `0904.3297` (cit. on p. 36).

[130]   K. Fabricius et al. 'Higher Order Perturbative QCD Calculation of Jet Cross-Sections in e+ e- Annihilation'. *Z. Phys.* C11 (1981), p. 315. DOI: `10.1007/BF01578281` (cit. on p. 36).

[131]   G. Kramer, B. Lampe. 'Jet Cross-Sections in e+ e- Annihilation'. *Fortsch. Phys.* 37 (1989), p. 161 (cit. on p. 36).

[132]   W. T. Giele, E. W. N. Glover. 'Higher order corrections to jet cross-sections in e+ e- annihilation'. *Phys. Rev.* D46 (1992), pp. 1980–2010. DOI: `10.1103/PhysRevD.46.1980` (cit. on p. 36).

[133]   W. T. Giele, E. W. N. Glover, D. A. Kosower. 'Higher order corrections to jet cross-sections in hadron colliders'. *Nucl. Phys.* B403 (1993), pp. 633–670. DOI: `10.1016/0550-3213(93)90365-V`. arXiv: `hep-ph/9302225 [hep-ph]` (cit. on p. 36).

[134]   U. Baur, T. Han, J. Ohnemus. 'QCD corrections and nonstandard three vector boson couplings in W^+W^- production at hadron colliders'. *Phys. Rev.* D53 (1996), pp. 1098–1123. DOI: `10.1103/PhysRevD.53.1098`. arXiv: `hep-ph/9507336 [hep-ph]` (cit. on pp. 36, 84).

[135]   A. Gehrmann-De Ridder, E. W. N. Glover. 'A Complete O (alpha alpha-s) cal-
        culation of the photon + 1 jet rate in e+ e- annihilation'. *Nucl. Phys.* B517
        (1998), pp. 269–323. DOI: 10.1016/S0550-3213(97)00818-3. arXiv: hep-
        ph/9707224 [hep-ph] (cit. on p. 36).

[136]   B. W. Harris, J. F. Owens. 'The Two cutoff phase space slicing method'. *Phys.
        Rev.* D65 (2002), p. 094032. DOI: 10.1103/PhysRevD.65.094032. arXiv: hep-
        ph/0102128 [hep-ph] (cit. on p. 36).

[137]   C. G. Bollini, J. J. Giambiagi. 'Dimensional Renormalization: The Number of
        Dimensions as a Regularizing Parameter'. *Nuovo Cim.* B12 (1972), pp. 20–26.
        DOI: 10.1007/BF02895558 (cit. on p. 37).

[138]   G. 't Hooft, M. Veltman. 'Regularization and Renormalization of Gauge Fields'.
        Nucl.Phys. B44.1 (1972), pp. 189–213. ISSN: 0550-3213. DOI: 10.1016/0550-
        3213(72)90279-9 (cit. on p. 37).

[139]   G. M. Cicuta, E. Montaldi. 'Analytic renormalization via continuous space
        dimension'. *Lett. Nuovo Cim.* 4 (1972), pp. 329–332. DOI: 10.1007/BF02756527
        (cit. on p. 37).

[140]   J. F. Ashmore. 'A Method of Gauge Invariant Regularization'. *Lett. Nuovo Cim.*
        4 (1972), pp. 289–290. DOI: 10.1007/BF02824407 (cit. on p. 37).

[141]   G. Heinrich. 'Introduction to Loop Calculations'. Lecture script. Mar. 2010.
        http://www.ippp.dur.ac.uk/~gudrun/teaching/ILC.pdf (cit. on pp. 37,
        38).

[142]   M. E. Peskin, D. V. Schroeder. *An Introduction to Quantum Field Theory*. West-
        view Press, 1995. ISBN: 978-0-201-50397-5 (cit. on p. 37).

[143]   J. C. Collins. *Renormalization*. Cambridge Books Online. Cambridge Uni-
        versity Press, 1984. ISBN: 9780511622656. http://dx.doi.org/10.1017/
        CBO9780511622656 (cit. on p. 38).

[144]   W. Siegel. 'Supersymmetric Dimensional Regularization via Dimensional Re-
        duction'. *Phys. Lett.* B84 (1979), p. 193. DOI: 10.1016/0370-2693(79)90282-X
        (cit. on p. 38).

[145]   D. M. Capper, D. R. T. Jones, P. van Nieuwenhuizen. 'Regularization by Dimen-
        sional Reduction of Supersymmetric and Nonsupersymmetric Gauge Theo-
        ries'. *Nucl. Phys.* B167 (1980), p. 479. DOI: 10.1016/0550-3213(80)90244-8
        (cit. on p. 38).

[146]   W. B. Kilgore. 'Regularization Schemes and Higher Order Corrections'. *Phys.
        Rev.* D83 (2011), p. 114005. DOI: 10.1103/PhysRevD.83.114005. arXiv: 1102.
        5353 [hep-ph] (cit. on p. 38).

[147] T. Binoth et al. 'An algebraic/numerical formalism for one-loop multi-leg amplitudes'. *JHEP* 0510 (2005). arXiv v3 updated for rank-6-pentagons, p. 015. DOI: 10.1088/1126-6708/2005/10/015. arXiv: hep-ph/0504267 (cit. on pp. 38, 63, 65–70).

[148] G. Ossola, C. G. Papadopoulos, R. Pittau. 'Reducing full one-loop amplitudes to scalar integrals at the integrand level'. *Nucl.Phys.* B763 (2007), pp. 147–169. DOI: 10.1016/j.nuclphysb.2006.11.012. arXiv: hep-ph/0609007 (cit. on pp. 39, 45).

[149] Z. Bern et al. 'One-Loop n-Point Gauge Theory Amplitudes, Unitarity and Collinear Limits'. *Nucl.Phys.B* 425 (1994), pp. 217–260. arXiv: hep-ph/9403226 (cit. on pp. 39, 45).

[150] P. Mastrolia et al. 'Optimizing the Reduction of One-Loop Amplitudes'. *JHEP* 0806 (2008), p. 030. DOI: 10.1088/1126-6708/2008/06/030. arXiv: 0803.3964 [hep-ph] (cit. on p. 39).

[151] R. K. Ellis, W. T. Giele, Z. Kunszt. 'A Numerical Unitarity Formalism for Evaluating One-Loop Amplitudes'. *JHEP* 03 (2008), p. 003. DOI: 10.1088/1126-6708/2008/03/003. arXiv: 0708.2398 [hep-ph] (cit. on p. 39).

[152] W. T. Giele, Z. Kunszt, K. Melnikov. 'Full one-loop amplitudes from tree amplitudes'. *JHEP* 0804 (2008), p. 049. DOI: 10.1088/1126-6708/2008/04/049. arXiv: 0801.2237 [hep-ph] (cit. on p. 39).

[153] C. F. Berger et al. 'An Automated Implementation of On-Shell Methods for One-Loop Amplitudes'. *Phys. Rev.* D78 (2008), p. 036003. DOI: 10.1103/PhysRevD.78.036003. arXiv: 0803.4180 [hep-ph] (cit. on p. 39).

[154] T. Hahn. 'Generating Feynman diagrams and amplitudes with FeynArts 3'. *Comput. Phys. Commun.* 140 (2001), pp. 418–431. DOI: 10.1016/S0010-4655(01)00290-9. arXiv: hep-ph/0012260 [hep-ph] (cit. on p. 39).

[155] T. Hahn, M. Perez-Victoria. 'Automatized one loop calculations in four-dimensions and D-dimensions'. *Comput. Phys. Commun.* 118 (1999), pp. 153–165. DOI: 10.1016/S0010-4655(98)00173-8. arXiv: hep-ph/9807565 [hep-ph] (cit. on pp. 39, 46).

[156] C. Groß et al. 'New Developments in FormCalc 8.4'. *PoS LL2014* 035 (2014). arXiv: 1407.0235 [hep-ph] (cit. on p. 39).

[157] G. Belanger et al. 'Automatic calculations in high energy physics and Grace at one-loop'. *Phys. Rept.* 430 (2006), pp. 117–209. DOI: 10.1016/j.physrep.2006.02.001. arXiv: hep-ph/0308080 [hep-ph] (cit. on p. 39).

[158] G. Bevilacqua et al. 'HELAC-NLO'. *Comput. Phys. Commun.* 184 (2013), pp. 986–997. DOI: 10.1016/j.cpc.2012.10.033. arXiv: 1110.1499 [hep-ph] (cit. on p. 39).

[159] D. Lopez-Val et al. 'MadGolem: automating NLO calculations for New Physics'. *PoS LL2012* 048 (2012). arXiv: 1209.2797 [hep-ph] (cit. on p. 39).

[160] J. Alwall et al. 'The automated computation of tree-level and next-to-leading order differential cross sections, and their matching to parton shower simulations'. *JHEP* 07(2014)079 (May 2014), p. 07079. arXiv: 1405.0301 (cit. on pp. 39, 44).

[161] S. Badger et al. 'Numerical evaluation of virtual corrections to multi-jet production in massless QCD'. *Comput. Phys. Commun.* 184 (2013), pp. 1981–1998. DOI: 10.1016/j.cpc.2013.03.018. arXiv: 1209.0100 [hep-ph] (cit. on p. 39).

[162] F. Cascioli, P. Maierhofer, S. Pozzorini. 'Scattering Amplitudes with Open Loops'. *Phys. Rev. Lett.* 108 (2012), p. 111601. DOI: 10.1103/PhysRevLett.108.111601. arXiv: 1111.5206 [hep-ph] (cit. on p. 39).

[163] S. Actis et al. 'Recursive generation of one-loop amplitudes in the Standard Model'. *JHEP* 04 (2013), p. 037. DOI: 10.1007/JHEP04(2013)037. arXiv: 1211.6316 [hep-ph] (cit. on p. 39).

[164] K. Arnold et al. 'VBFNLO: A Parton Level Monte Carlo for Processes with Electroweak Bosons – Manual for Version 2.5.0' (2011). arXiv: 1107.4038 [hep-ph] (cit. on pp. 39, 110).

[165] S. Höche. 'Introduction to parton-shower event generators'. In: *Theoretical Advanced Study Institute in Elementary Particle Physics: Journeys Through the Precision Frontier: Amplitudes for Colliders (TASI 2014) Boulder, Colorado, June 2-27, 2014*. 2014. arXiv: 1411.4085 [hep-ph] (cit. on p. 40).

[166] S. Catani et al. 'QCD matrix elements + parton showers'. *JHEP* 11 (2001), p. 063. DOI: 10.1088/1126-6708/2001/11/063. arXiv: hep-ph/0109231 [hep-ph] (cit. on p. 40).

[167] F. Krauss. 'Matrix elements and parton showers in hadronic interactions'. *JHEP* 08 (2002), p. 015. DOI: 10.1088/1126-6708/2002/08/015. arXiv: hep-ph/0205283 [hep-ph] (cit. on p. 40).

[168] S. Catani et al. 'New clustering algorithm for multi - jet cross-sections in e+ e- annihilation'. *Phys. Lett.* B269 (1991), pp. 432–438. DOI: 10.1016/0370-2693(91)90196-W (cit. on p. 40).

[169] L. Lonnblad. 'Correcting the color dipole cascade model with fixed order matrix elements'. *JHEP* 05 (2002), p. 046. DOI: 10.1088/1126-6708/2002/05/046. arXiv: hep-ph/0112284 [hep-ph] (cit. on p. 40).

[170] M. L. Mangano et al. 'Matching matrix elements and shower evolution for top-quark production in hadronic collisions'. *JHEP* 01 (2007), p. 013. DOI: 10.1088/1126-6708/2007/01/013. arXiv: hep-ph/0611129 [hep-ph] (cit. on p. 40).

[171] S. Hoeche et al. 'Matching parton showers and matrix elements'. In: *HERA and the LHC: A Workshop on the implications of HERA for LHC physics: Proceedings Part A*. 2006. arXiv: hep-ph/0602031 [hep-ph] (cit. on p. 40).

[172] S. Frixione, B. R. Webber. 'Matching NLO QCD computations and parton shower simulations'. *JHEP* 06 (2002), p. 029. DOI: 10.1088/1126-6708/2002/06/029. arXiv: hep-ph/0204244 [hep-ph] (cit. on pp. 40, 83, 104).

[173] S. Frixione, P. Nason, B. R. Webber. 'Matching NLO QCD and parton showers in heavy flavor production'. *JHEP* 08 (2003), p. 007. DOI: 10.1088/1126-6708/2003/08/007. arXiv: hep-ph/0305252 [hep-ph] (cit. on p. 40).

[174] S. Frixione, B. R. Webber. 'The MC@NLO 2.0 event generator' (2003). arXiv: hep-ph/0307146 [hep-ph] (cit. on p. 40).

[175] P. Nason. 'A New method for combining NLO QCD with shower Monte Carlo algorithms'. *JHEP* 11 (2004), p. 040. DOI: 10.1088/1126-6708/2004/11/040. arXiv: hep-ph/0409146 [hep-ph] (cit. on p. 40).

[176] N. Lavesson, L. Lonnblad. 'Extending CKKW-merging to One-Loop Matrix Elements'. *JHEP* 12 (2008), p. 070. DOI: 10.1088/1126-6708/2008/12/070. arXiv: 0811.2912 [hep-ph] (cit. on p. 40).

[177] R. Frederix, S. Frixione. 'Merging meets matching in MC@NLO'. *JHEP* 12 (2012), p. 061. DOI: 10.1007/JHEP12(2012)061. arXiv: 1209.6215 [hep-ph] (cit. on p. 40).

[178] S. Hoeche et al. 'QCD matrix elements and truncated showers'. *JHEP* 05 (2009), p. 053. DOI: 10.1088/1126-6708/2009/05/053. arXiv: 0903.1219 [hep-ph] (cit. on p. 40).

[179] L. Lönnblad, S. Prestel. 'Merging Multi-leg NLO Matrix Elements with Parton Showers'. *JHEP* 03 (2013), p. 166. DOI: 10.1007/JHEP03(2013)166. arXiv: 1211.7278 [hep-ph] (cit. on p. 40).

[180] M. Bahr et al. 'Herwig++ Physics and Manual'. *Eur.Phys.J.* C58 (2008), pp. 639–707. DOI: 10.1140/epjc/s10052-008-0798-9. arXiv: 0803.0883 [hep-ph] (cit. on pp. 40, 44).

[181]   K. Arnold et al. 'Herwig++ 2.6 Release Note' (2012). arXiv: 1205.4902 [hep-ph] (cit. on pp. 40, 44).

[182]   J. Bellm et al. 'Herwig 7.0 / Herwig++ 3.0 Release Note' (2015). arXiv: 1512. 01178 [hep-ph] (cit. on pp. 40, 44, 56, 87).

[183]   T. Gleisberg et al. 'Event generation with SHERPA 1.1'. *JHEP* 0902 (Nov. 2009), p. 007. DOI: 10.1088/1126-6708/2009/02/007. arXiv: 0811.4622 (cit. on pp. 40, 43).

[184]   T. Sjostrand, S. Mrenna, P. Z. Skands. 'PYTHIA 6.4 Physics and Manual'. *JHEP* 05 (2006), p. 026. DOI: 10.1088/1126-6708/2006/05/026. arXiv: hep-ph/0603175 [hep-ph] (cit. on p. 40).

[185]   T. Sjostrand, S. Mrenna, P. Z. Skands. 'A Brief Introduction to PYTHIA 8.1'. *Comput. Phys. Commun.* 178 (2008), pp. 852–867. DOI: 10.1016/j.cpc.2008. 01.036. arXiv: 0710.3820 [hep-ph] (cit. on p. 40).

[186]   W. T. Giele, D. A. Kosower, P. Z. Skands. 'Higher-Order Corrections to Timelike Jets'. *Phys. Rev.* D84 (2011), p. 054003. DOI: 10.1103/PhysRevD.84.054003. arXiv: 1102.2126 [hep-ph] (cit. on p. 40).

[187]   M. Ritzmann, D. A. Kosower, P. Skands. 'Antenna Showers with Hadronic Initial States'. *Phys. Lett.* B718 (2013), pp. 1345–1350. DOI: 10.1016/j.physletb.2012. 12.003. arXiv: 1210.6345 [hep-ph] (cit. on p. 40).

[188]   L. Hartgring, E. Laenen, P. Skands. 'Antenna Showers with One-Loop Matrix Elements'. *JHEP* 10 (2013), p. 127. DOI: 10.1007/JHEP10(2013)127. arXiv: 1303.4974 [hep-ph] (cit. on p. 40).

[189]   A. J. Larkoski, J. J. Lopez-Villarejo, P. Skands. 'Helicity-Dependent Showers and Matching with VINCIA'. *Phys. Rev.* D87.5 (2013), p. 054033. DOI: 10.1103/ PhysRevD.87.054033. arXiv: 1301.0933 [hep-ph] (cit. on p. 40).

[190]   L. Lonnblad. 'ARIADNE version 4: A Program for simulation of QCD cascades implementing the color dipole model'. *Comput. Phys. Commun.* 71 (1992), pp. 15–31. DOI: 10.1016/0010-4655(92)90068-A (cit. on p. 40).

[191]   S. Alioli et al. 'Combining Higher-Order Resummation with Multiple NLO Calculations and Parton Showers in GENEVA'. *JHEP* 09 (2013), p. 120. DOI: 10.1007/JHEP09(2013)120. arXiv: 1211.7049 [hep-ph] (cit. on p. 40).

[192]   J. F. von Soden-Fraunhofen. 'Diphoton plus jet production through graviton exchange at NLO'. Diplomarbeit (diploma thesis). Max-Planck-Institut für Physik, Technische Universität München, 2012 (cit. on pp. 43, 63).

[193] N. Greiner et al. 'NLO QCD corrections to the production of two bottom-antibottom pairs at the LHC'. *Phys.Rev.Lett.* 107 (May 2011), p. 102002. DOI: 10.1103/PhysRevLett.107.102002. arXiv: 1105.3624 (cit. on p. 43).

[194] N. Greiner et al. 'NLO QCD corrections to the production of W+ W- plus two jets at the LHC'. *Phys.Lett.* B713 (Feb. 2012), pp. 277–283. DOI: 10.1016/j.physletb.2012.06.027. arXiv: 1202.6004 (cit. on p. 43).

[195] G. Cullen, N. Greiner, G. Heinrich. 'Susy-QCD corrections to neutralino pair production in association with a jet'. *Eur.Phys.J.* C73 (Dec. 2013), p. 2388. DOI: 10.1140/epjc/s10052-013-2388-8. arXiv: 1212.5154 (cit. on p. 43).

[196] T. Gehrmann, N. Greiner, G. Heinrich. 'Photon isolation effects at NLO in gamma gamma + jet final states in hadronic collisions'. *JHEP* 1306 (Mar. 2013), p. 058. DOI: 10.1007/JHEP06(2013)058. arXiv: 1303.0824 (cit. on p. 43).

[197] T. Gehrmann, N. Greiner, G. Heinrich. 'Precise QCD predictions for the production of a photon pair in association with two jets'. *Phys.Rev.Lett.* 111 (Aug. 2013), p. 222002. DOI: 10.1103/PhysRevLett.111.222002. arXiv: 1308.3660 (cit. on p. 43).

[198] M. J. Dolan et al. 'Further on up the road: $hhjj$ production at the LHC' (Oct. 2013). arXiv: 1310.1084 (cit. on p. 43).

[199] G. Cullen et al. 'Next-to-Leading-Order QCD Corrections to Higgs Boson Production Plus Three Jets in Gluon Fusion'. *Phys. Rev. Lett.* 111.13 (July 2013), p. 131801. DOI: 10.1103/PhysRevLett.111.131801. arXiv: 1307.4737 (cit. on p. 43).

[200] G. Heinrich et al. 'NLO QCD corrections to WWbb production with leptonic decays in the light of top quark mass and asymmetry measurements' (Dec. 2013). arXiv: 1312.6659 (cit. on p. 43).

[201] S. Hoeche et al. 'Zero and one jet combined NLO analysis of the top quark forward-backward asymmetry'. *Phys.Rev.* D88 (June 2013), p. 014040. DOI: 10.1103/PhysRevD.88.014040. arXiv: 1306.2703 (cit. on p. 43).

[202] H. van Deurzen et al. 'NLO QCD corrections to Higgs boson production in association with a top quark pair and a jet'. *Phys.Rev.Lett.* 111 (July 2013), p. 171801. DOI: 10.1103/PhysRevLett.111.171801. arXiv: 1307.8437 (cit. on p. 43).

[203] G. Luisoni et al. 'HW/HZ + 0 and 1 jet at NLO with the POWHEG BOX interfaced to GoSam and their merging within MiNLO'. *JHEP* 1310 (June 2013), p. 083. DOI: 10.1007/JHEP10(2013)083. arXiv: 1306.2542 (cit. on p. 43).

[204] N. Greiner et al. 'Model-Independent Production of a Top-Philic Resonance at the LHC'. *JHEP* 04 (2015), p. 029. DOI: 10.1007/JHEP04(2015)029. arXiv: 1410.6099 [hep-ph] (cit. on p. 43).

[205] G. Luisoni, C. Oleari, F. Tramontano. 'Wbbj production at NLO with POWHEG+MiNLO'. *JHEP* 1504 (Feb. 2015), p. 161. DOI: 10.1007/JHEP04(2015)161. arXiv: 1502.01213 (cit. on p. 43).

[206] H. van Deurzen et al. 'Spin Polarisation of $t\bar{t}\gamma\gamma$ production at NLO+PS with GoSam interfaced to MadGraph5_aMC@NLO' (Sept. 2015). arXiv: 1509.02077 (cit. on pp. 43, 44).

[207] N. Greiner, S. Liebler, G. Weiglein. 'Interference contributions to gluon initiated heavy Higgs production in the Two-Higgs-Doublet Model'. *Eur. Phys. J.* C76.3 (2016), p. 118. DOI: 10.1140/epjc/s10052-016-3965-4. arXiv: 1512.07232 [hep-ph] (cit. on p. 43).

[208] T. Stelzer, W. F. Long. 'Automatic Generation of Tree Level Helicity Amplitudes'. *Comput.Phys.Commun.* 81 (1994), pp. 357–371. arXiv: hep-ph/9401258 (cit. on p. 44).

[209] R. Frederix, T. Gehrmann, N. Greiner. 'Automation of the Dipole Subtraction Method in MadGraph/MadEvent'. *JHEP* 0809 (Aug. 2008), p. 122. DOI: 10.1088/1126-6708/2008/09/122. arXiv: 0808.2128 (cit. on p. 44).

[210] R. Frederix, T. Gehrmann, N. Greiner. 'Integrated dipoles with MadDipole in the MadGraph framework'. *JHEP* 1006 (Apr. 2010), p. 086. DOI: 10.1007/JHEP06(2010)086. arXiv: 1004.2905 (cit. on p. 44).

[211] F. Maltoni, T. Stelzer. 'MadEvent: Automatic Event Generation with MadGraph'. *JHEP* 0302 (2003), p. 027. arXiv: hep-ph/0208156 (cit. on p. 44).

[212] J. Bellm et al. 'Herwig++ 2.7 Release Note' (Oct. 2013). arXiv: 1310.6877 (cit. on p. 44).

[213] S. Frixione, P. Nason, C. Oleari. 'Matching NLO QCD computations with Parton Shower simulations: the POWHEG method'. *JHEP* 0711 (Sept. 2007), p. 070. DOI: 10.1088/1126-6708/2007/11/070. arXiv: 0709.2092 (cit. on p. 44).

[214] S. Alioli et al. 'A general framework for implementing NLO calculations in shower Monte Carlo programs: the POWHEG BOX'. *JHEP* 1006 (Feb. 2010), p. 043. DOI: 10.1007/JHEP06(2010)043. arXiv: 1002.2581 (cit. on p. 44).

[215] W. Kilian, T. Ohl, J. Reuter. 'WHIZARD: Simulating Multi-Particle Processes at LHC and ILC'. *Eur. Phys. J.* C71 (2011), p. 1742. DOI: 10.1140/epjc/s10052-011-1742-y. arXiv: 0708.4233 [hep-ph] (cit. on p. 44).

[216] C. Weiss et al. 'Automated NLO QCD Corrections with WHIZARD'. *PoS* EPS-HEP2015 (2015), p. 466. arXiv: 1510.02666 [hep-ph] (cit. on p. 44).

[217] B. C. Nejad et al. 'Matching NLO QCD Corrections in WHIZARD with the POWHEG scheme'. *PoS* EPS-HEP2015 (2015), p. 317. arXiv: 1510.02739 [hep-ph] (cit. on p. 44).

[218] M. Chiesa et al. 'Electroweak Sudakov Corrections to New Physics Searches at the CERN LHC'. *Phys.Rev.Lett.* 111 (May 2013), p. 121801. DOI: 10.1103/PhysRevLett.111.121801. arXiv: 1305.6837 (cit. on p. 44).

[219] M. Chiesa, N. Greiner, F. Tramontano. 'Automation of electroweak corrections for LHC processes'. *J. Phys.* G43.1 (2016), p. 013002. DOI: 10.1088/0954-3899/43/1/013002. arXiv: 1507.08579 [hep-ph] (cit. on p. 44).

[220] P. Nogueira. 'Automatic Feynman Graph Generation'. *Journal of Computational Physics* 105.2 (Apr. 1993), pp. 279–289. DOI: 10.1006/jcph.1993.1074 (cit. on p. 44).

[221] J. A. M. Vermaseren. 'New features of FORM' (2000). arXiv: math-ph/0010025 (cit. on p. 44).

[222] J. Kuipers et al. 'FORM version 4.0'. *Comput.Phys.Commun.* 184 (Mar. 2013), pp. 1453–1467. DOI: 10.1016/j.cpc.2012.12.028. arXiv: 1203.6543 (cit. on p. 44).

[223] J. Kuipers, T. Ueda, J. A. M. Vermaseren. 'Code Optimization in FORM' (Oct. 2013). arXiv: 1310.7007 (cit. on pp. 44, 47).

[224] G. Cullen, M. Koch-Janusz, T. Reiter. 'spinney: A Form Library for Helicity Spinors'. *Comput.Phys.Commun.* 182.11 (Aug. 2011), pp. 2368–2387. DOI: 10.1016/j.cpc.2011.06.007. arXiv: 1008.0803 (cit. on p. 44).

[225] T. Reiter. 'Optimising Code Generation with haggies' (July 2009). arXiv: 0907.3714 (cit. on p. 44).

[226] P. Mastrolia, E. Mirabella, T. Peraro. 'Integrand reduction of one-loop scattering amplitudes through Laurent series expansion'. *JHEP* 1206 (Mar. 2012). [Erratum: JHEP11,128(2012)], p. 095. DOI: 10.1007/JHEP11(2012)128, 10.1007/JHEP06(2012)095. arXiv: 1203.0291 (cit. on p. 45).

[227] G. Heinrich et al. 'Tensorial Reconstruction at the Integrand Level'. *JHEP* 1010:105,2010 (Aug. 2010). arXiv: 1008.2441 (cit. on pp. 46, 72, 78).

[228] R. K. Ellis, G. Zanderighi. 'Scalar one-loop integrals for QCD'. *JHEP* 02 (2008), p. 002. DOI: 10.1088/1126-6708/2008/02/002. arXiv: 0712.1851 [hep-ph] (cit. on pp. 46, 75).

[229] S. Carrazza, R. K. Ellis, G. Zanderighi. 'QCDLoop: a comprehensive framework for one-loop scalar integrals' (2016). arXiv: 1605.03181 [hep-ph] (cit. on p. 46).

[230] A. van Hameren. 'OneLOop: for the evaluation of one-loop scalar functions'. *Comput.Phys.Commun.* 182:2427-2438,2011 (July 2010). DOI: 10.1016/j.cpc.2011.06.011. arXiv: 1007.4716 (cit. on p. 46).

[231] G. J. van Oldenborgh. 'FF - a package to evaluate one-loop Feynman diagrams'. *Comput.Phys.Commun.* 66 (July 1991), pp. 1–15. DOI: 10.1016/0010-4655(91)90002-3 (cit. on p. 46).

[232] C. Degrande et al. 'UFO - The Universal FeynRules Output'. *Comput.Phys.Commun.* 183 (Aug. 2012), pp. 1201–1214. DOI: 10.1016/j.cpc.2012.01.022. arXiv: 1108.2040 (cit. on p. 46).

[233] N. D. Christensen, C. Duhr. 'FeynRules - Feynman rules made easy'. *Comput.Phys.Commun.* 180 (June 2009), pp. 1614–1641. arXiv: 0806.4194 (cit. on p. 46).

[234] A. Alloul et al. 'FEYNRULES 2.0 - A complete toolbox for tree-level phenomenology'. *Comput.Phys.Commun.* 185 (Aug. 2014), pp. 2250–2300. DOI: 10.1016/j.cpc.2014.04.012. arXiv: 1310.1921 [hep-ph] (cit. on p. 46).

[235] F. Staub. 'SARAH 4: A tool for (not only SUSY) model builders'. *Comput.Phys.Commun.* 185 (Sept. 2014), pp.1773–1790. DOI: 10.1016/j.cpc.2014.02.018. arXiv: 1309.7223 (cit. on p. 46).

[236] V. Yundin. *PJFry - one loop tensor integral library*. 2011. https://github.com/Vayu/PJFry (cit. on p. 46).

[237] J. Fleischer, T. Riemann. 'A complete algebraic reduction of one-loop tensor Feynman integrals'. *Phys.Rev.D* 83 (Sept. 2011), p. 073004. arXiv: 1009.4436 (cit. on p. 46).

[238] J. Fleischer, T. Riemann, V. Yundin. 'New developments in PJFry'. *PoS LL2012* 020 (2012). arXiv: 1210.4095 [hep-ph] (cit. on p. 46).

[239] S. Badger, B. Biedermann, P. Uwer. 'NGluon: A Package to Calculate One-loop Multi-gluon Amplitudes'. *Comput. Phys. Commun.* 182 (2011), pp. 1674–1692. DOI: 10.1016/j.cpc.2011.04.008. arXiv: 1011.2900 [hep-ph] (cit. on p. 48).

[240] T. Binoth et al. 'A Proposal for a standard interface between Monte Carlo tools and one-loop programs'. *Comput.Phys.Commun.* 181 (2010), pp. 1612–1622. DOI: 10.1016/j.cpc.2010.05.016. arXiv: 1001.1307 [hep-ph] (cit. on p. 55).

[241] S. Plätzer. 'A draft runtime interface to combine parton shower and next-to-leading order QCD programs'. In: *The Tools and Monte Carlo Working Group Summary Report*. Les Houches 2009. 2010. arXiv: `1003.1643` (cit. on p. 56).

[242] E. Boos et al. 'Generic user process interface for event generators'. In: *Physics at TeV colliders. Proceedings, Euro Summer School, Les Houches, France, May 21-June 1, 2001*. 2001. arXiv: `hep-ph/0109068 [hep-ph]`. `http://lss.fnal.gov/archive/preprint/fermilab-conf-01-496-t.shtml` (cit. on p. 56).

[243] J. Alwall et al. 'A Standard format for Les Houches event files'. *Comput. Phys. Commun.* 176 (2007), pp. 300–304. DOI: `10.1016/j.cpc.2006.11.010`. arXiv: `hep-ph/0609017 [hep-ph]` (cit. on p. 56).

[244] J. M. Butterworth et al. 'THE TOOLS AND MONTE CARLO WORKING GROUP Summary Report from the Les Houches 2009 Workshop on TeV Colliders'. In: *Physics at TeV colliders. Proceedings, 6th Workshop, dedicated to Thomas Binoth, Les Houches, France, June 8-26, 2009*. 2010. arXiv: `1003.1643 [hep-ph]` (cit. on p. 56).

[245] J. R. Andersen et al. 'Les Houches 2013: Physics at TeV Colliders: Standard Model Working Group Report' (2014). arXiv: `1405.1067 [hep-ph]` (cit. on pp. 56, 60).

[246] A. Buckley et al. 'Rivet user manual'. *Comput. Phys. Commun.* 184 (2013), pp. 2803–2819. DOI: `10.1016/j.cpc.2013.05.021`. arXiv: `1003.0694 [hep-ph]` (cit. on pp. 56, 89).

[247] J. Beringer et al. 'Review of Particle Physics (RPP)'. *Phys.Rev.* D86 (2012), p. 010001. DOI: `10.1103/PhysRevD.86.010001` (cit. on p. 59).

[248] M. Rodgers. 'Automation of one-loop corrections for multi-particle processes'. PhD thesis. Durham University, July 2012. `http://etheses.dur.ac.uk/4460/` (cit. on pp. 63, 75).

[249] T. Binoth, J. P. Guillet, G. Heinrich. 'Reduction formalism for dimensionally regulated one-loop N-point integrals'. *Nucl.Phys.B* 572:361-386,2000 (2000). DOI: `10.1016/S0550-3213(00)00040-7`. arXiv: `hep-ph/9911342` (cit. on pp. 64, 66).

[250] A. I. Davydychev. 'A simple formula for reducing Feynman diagrams to scalar integrals'. *Physics Letters B* 263 (July 1991), pp. 107–111. DOI: `10.1016/0370-2693(91)91715-8` (cit. on pp. 64, 65).

[251] G. Passarino, M. Veltman. 'One-loop corrections for e^+e^- annihilation into $\mu^+\mu^-$ in the Weinberg model'. *Nuclear Physics B* 160 (1 Nov. 1979), pp. 151–207. DOI: `10.1016/0550-3213(79)90234-7` (cit. on p. 65).

[252]   A. Denner, S. Dittmaier. 'Reduction schemes for one-loop tensor integrals'. *Nucl.Phys.B* 734 (2006), pp. 62–115. DOI: `10.1016/j.nuclphysb.2005.11.007`. arXiv: `hep-ph/0509141` (cit. on p. 65).

[253]   R. G. Stuart. 'Algebraic reduction of one-loop Feynman diagrams to scalar integrals'. *Computer Physics Communications* 48 (Mar. 1988), pp. 367–389. DOI: `10.1016/0010-4655(88)90202-0` (cit. on p. 65).

[254]   G. van Oldenborgh, J. Vermaseren. 'New Algorithms for One Loop Integrals'. *Z.Phys.* C46 (1990), pp. 425–438. DOI: `10.1007/BF01621031` (cit. on p. 65).

[255]   Y. Ezawa et al. 'Brown-Feynman reduction of one loop Feynman diagrams to scalar integrals with orthonormal basis tensors'. *Comput.Phys.Commun.* 69 (1992), pp. 15–45. DOI: `10.1016/0010-4655(92)90125-I` (cit. on p. 65).

[256]   A. Denner. 'Techniques for the Calculation of Electroweak Radiative Corrections at the One-Loop Level and Results for W-physics at LEP 200'. *Fortsch.Phys.* 41.4 (1993), pp. 307–420. ISSN: 1521-3979. DOI: `10.1002/prop.2190410402`. arXiv: `0709.1075` (cit. on p. 65).

[257]   G. Devaraj, R. G. Stuart. 'Reduction of one loop tensor form-factors to scalar integrals: A General scheme'. *Nucl.Phys.* B519 (1998), pp. 483–513. DOI: `10.1016/S0550-3213(98)00035-2`. arXiv: `hep-ph/9704308 [hep-ph]` (cit. on p. 65).

[258]   F. del Aguila, R. Pittau. 'Recursive numerical calculus of one-loop tensor integrals'. *JHEP* 0407 (2004), p. 017. DOI: `10.1088/1126-6708/2004/07/017`. arXiv: `hep-ph/0404120` (cit. on p. 65).

[259]   A. van Hameren, J. Vollinga, S. Weinzierl. 'Automated computation of one-loop integrals in massless theories'. *Eur.Phys.J.* C41 (2005), pp. 361–375. DOI: `10.1140/epjc/s2005-02229-6`. arXiv: `hep-ph/0502165` (cit. on p. 65).

[260]   A. Denner, S. Dittmaier, L. Hofer. 'Collier: a fortran-based Complex One-Loop LIbrary in Extended Regularizations' (2016). arXiv: `1604.06792 [hep-ph]` (cit. on p. 65).

[261]   Z. Bern, L. Dixon, D. A. Kosower. 'Dimensionally Regulated One-Loop Integrals'. *Phys.Lett.* B302 (1993), pp. 299–308. DOI: `10.1016/0370-2693(93)90400-C`. arXiv: `hep-ph/9212308` (cit. on p. 65).

[262]   O. V. Tarasov. 'Connection between Feynman integrals having different values of the space-time dimension'. *Phys.Rev.* D54 (1996), pp. 6479–6490. DOI: `10.1103/PhysRevD.54.6479`. arXiv: `hep-th/9606018` (cit. on p. 65).

[263] J. Fleischer, M. Y. Kalmykov. 'Single mass scale diagrams: construction of a basis for the ϵ-expansion'. *Phys.Lett.* B470 (1999), pp. 168–176. DOI: 10.1016/S0370-2693(99)01321-0. arXiv: hep-ph/9910223 (cit. on p. 65).

[264] J. Fleischer, F. Jegerlehner, O. V. Tarasov. 'Algebraic reduction of one-loop Feynman graph amplitudes'. *Nucl.Phys.* B566 (2000), pp. 423–440. DOI: 10.1016/S0550-3213(99)00678-1. arXiv: hep-ph/9907327 (cit. on p. 65).

[265] G. Duplancic, B. Nizic. 'Reduction method for dimensionally regulated one-loop N-point Feynman integrals'. *Eur.Phys.J.* C 35 (2004), pp. 105–118. arXiv: hep-ph/0303184 (cit. on p. 65).

[266] W. Giele, E. W. N. Glover, G. Zanderighi. 'Numerical Evaluation of One-Loop Diagrams Near Exceptional Momentum Configurations'. *Nucl.Phys.Proc.Suppl.* 135 (2004), pp. 275–279. DOI: 10.1016/j.nuclphysbps.2004.09.028. arXiv: hep-ph/0407016 (cit. on p. 65).

[267] J. M. Campbell, E. W. N. Glover, D. J. Miller. 'One-Loop Tensor Integrals in Dimensional Regularisation'. *Nucl.Phys.* B498 (1997), pp. 397–442. DOI: 10.1016/S0550-3213(97)00268-X. arXiv: hep-ph/9612413 (cit. on p. 65).

[268] J. P. Guillet et al. 'Stable One-Dimensional Integral Representations of One-Loop N-Point Functions in the General Massive Case: I - Three Point Functions'. *JHEP* 1311 (Oct. 2013), p. 154. DOI: 10.1007/JHEP11(2013)154. arXiv: 1310.4397 (cit. on pp. 66, 75).

[269] V. Hirschi, T. Peraro. 'Tensor integrand reduction via Laurent expansion' (2016). arXiv: 1604.01363 [hep-ph] (cit. on p. 72).

[270] S. Borowka, J. Carter, G. Heinrich. 'Numerical Evaluation of Multi-Loop Integrals for Arbitrary Kinematics with SecDec 2.0'. *Comput. Phys. Commun.* 184 (2013), pp. 396–408. DOI: 10.1016/j.cpc.2012.09.020. arXiv: 1204.4152 [hep-ph] (cit. on p. 75).

[271] S. Borowka, G. Heinrich. 'Massive non-planar two-loop four-point integrals with SecDec 2.1'. *Comput. Phys. Commun.* 184 (2013), pp. 2552–2561. DOI: 10.1016/j.cpc.2013.05.022. arXiv: 1303.1157 [hep-ph] (cit. on p. 75).

[272] S. C. Borowka. 'Evaluation of multi-loop multi-scale integrals and phenomenological two-loop applications'. PhD thesis. Munich, Tech. U., 2014. arXiv: 1410.7939 [hep-ph] (cit. on p. 75).

[273] S. Borowka et al. 'SecDec-3.0: numerical evaluation of multi-scale integrals beyond one loop'. *Comput. Phys. Commun.* 196 (2015), pp. 470–491. DOI: 10.1016/j.cpc.2015.05.022. arXiv: 1502.06595 [hep-ph] (cit. on p. 75).

[274] T. Hahn. 'CUBA: A Library for multidimensional numerical integration'. *Comput. Phys. Commun.* 168 (2005), pp. 78–95. DOI: 10.1016/j.cpc.2005.01.010. arXiv: hep-ph/0404043 [hep-ph] (cit. on p. 76).

[275] A. Denner, S. Dittmaier. 'Tensor one-loop integrals in exceptional phase-space regions'. In: *The NLO multileg working group: Summary report.* Physics at TeV colliders, La physique du TeV aux collisionneurs, Les Houches 2007. Bern, Z. et al., 2008. Chap. 10, pp. 54–60. arXiv: 0803.0494 [hep-ph]. http://www-public.slac.stanford.edu/sciDoc/docMeta.aspx?slacPubNumber=slac-pub-13206 (cit. on p. 76).

[276] ATLAS Collaboration. 'Search for high-mass diboson resonances with boson-tagged jets in proton-proton collisions at $\sqrt{s}$ = 8 TeV with the ATLAS detector'. *JHEP* 12 (June 2015), p. 055. DOI: 10.1007/JHEP12(2015)055. arXiv: 1506.00962 [hep-ex] (cit. on p. 81).

[277] ATLAS Collaboration. 'Search for production of WW/WZ resonances decaying to a lepton, neutrino and jets in pp collisions at $\sqrt{s}$ = 8 TeV with the ATLAS detector'. *Eur. Phys. J.* C75.5 (2015). [Erratum: Eur. Phys. J.C75,370(2015)], p. 209. DOI: 10.1140/epjc/s10052-015-3593-4,10.1140/epjc/s10052-015-3425-6. arXiv: 1503.04677 [hep-ex] (cit. on p. 81).

[278] CMS Collaboration. 'Search for massive resonances in dijet systems containing jets tagged as W or Z boson decays in pp collisions at sqrt(s) = 8 TeV'. *JHEP* 08 (May 2014), p. 173. arXiv: 1405.1994 (cit. on p. 81).

[279] CMS Collaboration. 'Search for massive resonances decaying into pairs of boosted bosons in semi-leptonic final states at sqrt(s) = 8 TeV'. *JHEP* 08 (May 2014), p. 174. arXiv: 1405.3447 (cit. on p. 81).

[280] J. Brehmer et al. 'The Diboson Excess: Experimental Situation and Classification of Explanations; A Les Houches Pre-Proceeding' (Dec. 2015). arXiv: 1512.04357 (cit. on p. 82).

[281] ATLAS Collaboration. 'Measurement of W^+W^- production in pp collisions at $\sqrt{s}$=7 TeV with the ATLAS detector and limits on anomalous WWZ and WWγ couplings'. *Phys. Rev.* D87.11 (2013). [Erratum: Phys. Rev.D88,no.7,079906(2013)], p. 112001. DOI: 10.1103/PhysRevD.87.112001,10.1103/PhysRevD.88.079906. arXiv: 1210.2979 [hep-ex] (cit. on p. 82).

[282] S. Chatrchyan et al. 'Measurement of the W^+W^- Cross section in pp Collisions at $\sqrt{s}$ = 7 TeV and Limits on Anomalous $WW\gamma$ and WWZ couplings'. *Eur. Phys. J.* C73.10 (2013), p. 2610. DOI: 10.1140/epjc/s10052-013-2610-8. arXiv: 1306.1126 [hep-ex] (cit. on p. 82).

[283]   ATLAS Collaboration. 'Measurement of the W^+W^- production cross section in proton-proton collisions at $\sqrt{s} = 8$ TeV with the ATLAS detector' (2014) (cit. on p. 82).

[284]   S. Chatrchyan et al. 'Measurement of W+W- and ZZ production cross sections in pp collisions at sqrt(s) = 8 TeV'. *Phys. Lett.* B721 (2013), pp. 190–211. DOI: 10.1016/j.physletb.2013.03.027. arXiv: 1301.4698 [hep-ex] (cit. on p. 82).

[285]   ATLAS Collaboration. 'Combination of searches for WW, WZ, and ZZ resonances in pp collisions at $\sqrt{s} = 8$ TeV with the ATLAS detector'. *Phys. Lett.* B755 (2016), pp. 285–305. DOI: 10.1016/j.physletb.2016.02.015. arXiv: 1512.05099 [hep-ex] (cit. on p. 82).

[286]   ATLAS Collaboration. *Search for diboson resonances in the llqq final state in pp collisions at $\sqrt{s}$ = 13 TeV with the ATLAS detector*. Tech. rep. ATLAS-CONF-2015-071. Geneva: CERN, Dec. 2015. http://cds.cern.ch/record/2114843 (cit. on p. 82).

[287]   ATLAS Collaboration. *Search for WW/WZ resonance production in the $\ell\nu qq$ final state at $\sqrt{s}$ = 13 TeV with the ATLAS detector at the LHC*. Tech. rep. ATLAS-CONF-2015-075. Geneva: CERN, Dec. 2015. http://cds.cern.ch/record/2114847 (cit. on p. 82).

[288]   CMS Collaboration. *Search for massive resonances decaying into pairs of boosted W and Z bosons at $\sqrt{s}$ = 13 TeV*. Tech. rep. CMS-PAS-EXO-15-002. Geneva: CERN, 2015. http://cds.cern.ch/record/2117062 (cit. on p. 82).

[289]   ATLAS Collaboration. 'Measurement of the ZZ Production Cross Section in pp Collisions at $\sqrt{s}$ = 13 TeV with the ATLAS Detector'. *Phys. Rev. Lett.* 116.10 (2016), p. 101801. DOI: 10.1103/PhysRevLett.116.101801. arXiv: 1512.05314 [hep-ex]. https://cds.cern.ch/record/2115496 (cit. on p. 82).

[290]   CMS Collaboration. 'Measurement of the ZZ production cross section in $\ell\ell\ell'\ell'$ decays in pp collisions at $\sqrt{s}$ = 13 TeV' (2015). https://cds.cern.ch/record/2114822 (cit. on p. 82).

[291]   ATLAS Collaboration. 'Determination of spin and parity of the Higgs boson in the $WW^* \rightarrow ev\mu\nu$ decay channel with the ATLAS detector'. *Eur. Phys. J.* C75.5 (2015), p. 231. DOI: 10.1140/epjc/s10052-015-3436-3. arXiv: 1503.03643 [hep-ex] (cit. on p. 82).

[292]   B. Abbott et al. 'Limits on $WW\gamma$ and WWZ couplings from W boson pair production'. *Phys. Rev.* D58 (1998), p. 051101. DOI: 10.1103/PhysRevD.58.051101. arXiv: hep-ex/9803004 [hep-ex] (cit. on p. 82).

[293] B. Abbott et al. 'Limits on anomalous $WW\gamma$ and WWZ couplings from $WW/WZ \rightarrow evjj$ production'. *Phys. Rev.* D62 (2000), p. 052005. DOI: 10.1103/PhysRevD.62.052005. arXiv: hep-ex/9912033 [hep-ex] (cit. on p. 82).

[294] R. Frederix et al. 'Four-lepton production at hadron colliders: aMC@NLO predictions with theoretical uncertainties'. *JHEP* 02 (2012), p. 099. DOI: 10.1007/JHEP02(2012)099. arXiv: 1110.4738 [hep-ph] (cit. on p. 83).

[295] J. M. Campbell, R. K. Ellis, C. Williams. 'Bounding the Higgs width at the LHC: Complementary results from $H \rightarrow WW$'. *Phys. Rev.* D89.5 (2014), p. 053011. DOI: 10.1103/PhysRevD.89.053011. arXiv: 1312.1628 [hep-ph] (cit. on p. 83).

[296] F. Caola, K. Melnikov. 'Constraining the Higgs boson width with ZZ production at the LHC'. *Phys. Rev.* D88 (2013), p. 054024. DOI: 10.1103/PhysRevD.88.054024. arXiv: 1307.4935 [hep-ph] (cit. on p. 83).

[297] N. Kauer, G. Passarino. 'Inadequacy of zero-width approximation for a light Higgs boson signal'. *JHEP* 08 (2012), p. 116. DOI: 10.1007/JHEP08(2012)116. arXiv: 1206.4803 [hep-ph] (cit. on p. 83).

[298] N. Kauer. 'Interference effects for H $\rightarrow$ WW/ZZ $\rightarrow \ell\bar{v}_\ell\bar{\ell}v_\ell$ searches in gluon fusion at the LHC'. *JHEP* 12 (2013), p. 082. DOI: 10.1007/JHEP12(2013)082. arXiv: 1310.7011 [hep-ph] (cit. on p. 83).

[299] N. Kauer, C. O'Brien, E. Vryonidou. 'Interference effects for $H \rightarrow W W \rightarrow \ell v q \bar{q}'$ and $H \rightarrow ZZ \rightarrow \ell\bar{\ell}q\bar{q}$ searches in gluon fusion at the LHC'. *JHEP* 10 (2015), p. 074. DOI: 10.1007/JHEP10(2015)074. arXiv: 1506.01694 [hep-ph] (cit. on p. 83).

[300] C. Englert, M. Spannowsky. 'Limitations and Opportunities of Off-Shell Coupling Measurements'. *Phys. Rev.* D90 (2014), p. 053003. DOI: 10.1103/PhysRevD.90.053003. arXiv: 1405.0285 [hep-ph] (cit. on p. 83).

[301] M. Buschmann et al. 'Mass Effects in the Higgs-Gluon Coupling: Boosted vs Off-Shell Production'. *JHEP* 02 (2015), p. 038. DOI: 10.1007/JHEP02(2015)038. arXiv: 1410.5806 [hep-ph] (cit. on p. 83).

[302] M. Bonvini et al. 'Signal-background interference effects for $ggHW^+W^-$ beyond leading order'. *Phys. Rev.* D88.3 (2013), p. 034032. DOI: 10.1103/PhysRevD.88.034032. arXiv: 1304.3053 [hep-ph] (cit. on p. 83).

[303] V. Khachatryan et al. 'Constraints on the Higgs boson width from off-shell production and decay to Z-boson pairs'. *Phys. Lett.* B736 (2014), pp. 64–85. DOI: 10.1016/j.physletb.2014.06.077. arXiv: 1405.3455 [hep-ex] (cit. on p. 83).

[304]   A. von Manteuffel, L. Tancredi. 'The two-loop helicity amplitudes for $gg \rightarrow V_1 V_2 \rightarrow 4$ leptons'. *JHEP* 06 (2015), p. 197. DOI: 10.1007/JHEP06(2015)197. arXiv: 1503.08835 [hep-ph] (cit. on p. 83).

[305]   T. Gehrmann, A. von Manteuffel, L. Tancredi. 'The two-loop helicity amplitudes for $q\overline{q}' \rightarrow V_1 V_2 \rightarrow 4$ leptons'. *JHEP* 09 (2015), p. 128. DOI: 10.1007/JHEP09(2015)128. arXiv: 1503.04812 [hep-ph] (cit. on p. 83).

[306]   P. Jaiswal. 'A New Perspective on Scale Uncertainties for Diboson Processes' (2014). arXiv: 1411.0677 [hep-ph] (cit. on p. 83).

[307]   M. Grazzini et al. 'Transverse-momentum resummation for vector-boson pair production at NNLL+NNLO'. *JHEP* 08 (2015), p. 154. DOI: 10.1007/JHEP08(2015)154. arXiv: 1507.02565 [hep-ph] (cit. on p. 84).

[308]   B. Biedermann et al. 'Next-to-leading-order electroweak corrections to $pp \rightarrow W^+W^- \rightarrow 4$ leptons at the LHC' (2016). arXiv: 1605.03419 [hep-ph] (cit. on p. 84).

[309]   M. Luszczak, A. Szczurek. 'Subleading processes in production of W^+W^- pairs in proton-proton collisions' (2013). arXiv: 1309.7201 [hep-ph] (cit. on p. 84).

[310]   S. Dittmaier, S. Kallweit, P. Uwer. 'NLO QCD corrections to WW+jet production at hadron colliders'. *Phys. Rev. Lett.* 100 (2008), p. 062003. DOI: 10.1103/PhysRevLett.100.062003. arXiv: 0710.1577 [hep-ph] (cit. on p. 84).

[311]   J. M. Campbell, R. K. Ellis, G. Zanderighi. 'Next-to-leading order predictions for $WW + 1$ jet distributions at the LHC'. *JHEP* 12 (2007), p. 056. DOI: 10.1088/1126-6708/2007/12/056. arXiv: 0710.1832 [hep-ph] (cit. on p. 84).

[312]   S. Dittmaier, S. Kallweit, P. Uwer. 'NLO QCD corrections to pp/ppbar –> WW+jet+X including leptonic W-boson decays'. *Nucl. Phys.* B826 (2010), pp. 18–70. DOI: 10.1016/j.nuclphysb.2009.09.029. arXiv: 0908.4124 [hep-ph] (cit. on p. 84).

[313]   W.-H. Li et al. 'NLO QCD and electroweak corrections to WW+jet production with leptonic W -boson decays at LHC'. *Phys. Rev.* D92.3 (2015), p. 033005. DOI: 10.1103/PhysRevD.92.033005. arXiv: 1507.07332 [hep-ph] (cit. on p. 84).

[314]   T. Melia et al. 'Gluon fusion contribution to W+W- + jet production'. *JHEP* 08 (2012), p. 115. DOI: 10.1007/JHEP08(2012)115. arXiv: 1205.6987 [hep-ph] (cit. on p. 84).

[315]   N. Agarwal et al. 'W^+W^- production in Large extra dimension model at next-to-leading order in QCD at the LHC'. *Phys. Rev.* D82 (2010), p. 036001. DOI: 10.1103/PhysRevD.82.036001. arXiv: 1003.5450 [hep-ph] (cit. on p. 84).

[316]   H. Potter, G. Valencia. 'Probing lepton gluonic couplings at the LHC'. *Phys. Lett.* B713 (2012), pp. 95–98. DOI: 10.1016/j.physletb.2012.05.052. arXiv: 1202.1780 [hep-ph] (cit. on p. 84).

[317]   W. Buchmuller, D. Wyler. 'Effective Lagrangian Analysis of New Interactions and Flavor Conservation'. *Nucl. Phys.* B268 (1986), pp. 621–653. DOI: 10.1016/0550-3213(86)90262-2 (cit. on p. 84).

[318]   B. Grzadkowski et al. 'Dimension-Six Terms in the Standard Model Lagrangian'. *JHEP* 10 (2010), p. 085. DOI: 10.1007/JHEP10(2010)085. arXiv: 1008.4884 [hep-ph] (cit. on p. 84).

[319]   R. Alonso et al. 'Renormalization Group Evolution of the Standard Model Dimension Six Operators III: Gauge Coupling Dependence and Phenomenology'. *JHEP* 04 (2014), p. 159. DOI: 10.1007/JHEP04(2014)159. arXiv: 1312.2014 [hep-ph] (cit. on p. 84).

[320]   L. Lehman. 'Extending the Standard Model Effective Field Theory with the Complete Set of Dimension-7 Operators'. *Phys. Rev.* D90.12 (2014), p. 125023. DOI: 10.1103/PhysRevD.90.125023. arXiv: 1410.4193 [hep-ph] (cit. on p. 84).

[321]   B. Henning et al. '2, 84, 30, 993, 560, 15456, 11962, 261485, ...: Higher dimension operators in the SM EFT' (2015). arXiv: 1512.03433 [hep-ph] (cit. on p. 84).

[322]   L. Lehman, A. Martin. 'Low-derivative operators of the Standard Model effective field theory via Hilbert series methods'. *JHEP* 02 (2016), p. 081. DOI: 10.1007/JHEP02(2016)081. arXiv: 1510.00372 [hep-ph] (cit. on p. 84).

[323]   C. Arzt, M. B. Einhorn, J. Wudka. 'Patterns of deviation from the standard model'. *Nucl. Phys.* B433 (1995), pp. 41–66. DOI: 10.1016/0550-3213(94)00336-D. arXiv: hep-ph/9405214 [hep-ph] (cit. on p. 84).

[324]   K. Hagiwara et al. 'Low-energy effects of new interactions in the electroweak boson sector'. *Phys. Rev.* D48 (1993), pp. 2182–2203. DOI: 10.1103/PhysRevD.48.2182 (cit. on p. 84).

[325]   W. H. Furry. 'A Symmetry Theorem in the Positron Theory'. *Phys. Rev.* 51 (1937), pp. 125–129. DOI: 10.1103/PhysRev.51.125 (cit. on p. 86).

[326]   L. A. Harland-Lang et al. 'Parton distributions in the LHC era: MMHT 2014 PDFs'. *Eur. Phys. J.* C75.5 (2015), p. 204. DOI: 10.1140/epjc/s10052-015-3397-6. arXiv: 1412.3989 [hep-ph] (cit. on p. 86).

[327]   A. Buckley et al. 'LHAPDF6: parton density access in the LHC precision era'. *Eur. Phys. J.* C75 (2015), p. 132. DOI: 10.1140/epjc/s10052-015-3318-8. arXiv: 1412.7420 [hep-ph] (cit. on p. 86).

[328] A. Denner, S. Dittmaier. 'The Complex-mass scheme for perturbative calculations with unstable particles'. *Nucl. Phys. Proc. Suppl.* 160 (2006), pp. 22–26. DOI: 10.1016/j.nuclphysbps.2006.09.025. arXiv: hep-ph/0605312 [hep-ph] (cit. on p. 89).

[329] ATLAS Collaboration. *A morphing technique for signal modelling in a multidimensional space of coupling parameters.* Tech. rep. ATL-PHYS-PUB-2015-047. Geneva: CERN, Nov. 2015. https://cds.cern.ch/record/2066980 (cit. on p. 98).

[330] S. Gieseke, P. Stephens, B. Webber. 'New formalism for QCD parton showers'. *JHEP* 12 (2003), p. 045. DOI: 10.1088/1126-6708/2003/12/045. arXiv: hep-ph/0310083 [hep-ph] (cit. on p. 104).

[331] G. Marchesini, B. R. Webber. 'Simulation of QCD Jets Including Soft Gluon Interference'. *Nucl. Phys.* B238 (1984), pp. 1–29. DOI: 10.1016/0550-3213(84)90463-2 (cit. on p. 104).

[332] G. Marchesini, B. R. Webber. 'Monte Carlo Simulation of General Hard Processes with Coherent QCD Radiation'. *Nucl. Phys.* B310 (1988), p. 461. DOI: 10.1016/0550-3213(88)90089-2 (cit. on p. 104).

[333] S. Plätzer, S. Gieseke. 'Dipole Showers and Automated NLO Matching in Herwig++'. *Eur.Phys.J.* C72 (2012), p. 2187. DOI: 10.1140/epjc/s10052-012-2187-7. arXiv: 1109.6256 [hep-ph] (cit. on p. 104).

[334] M. Cacciari, G. P. Salam, G. Soyez. 'FastJet User Manual'. *Eur. Phys. J.* C72 (2012), p. 1896. DOI: 10.1140/epjc/s10052-012-1896-2. arXiv: 1111.6097 [hep-ph] (cit. on p. 104).

[335] M. Cacciari, G. P. Salam. 'Dispelling the N^3 myth for the k_t jet-finder'. *Phys. Lett.* B641 (2006), pp. 57–61. DOI: 10.1016/j.physletb.2006.08.037. arXiv: hep-ph/0512210 [hep-ph] (cit. on p. 104).

[336] M. Cacciari, G. P. Salam, G. Soyez. 'The Anti-k(t) jet clustering algorithm'. *JHEP* 04 (2008), p. 063. DOI: 10.1088/1126-6708/2008/04/063. arXiv: 0802.1189 [hep-ph] (cit. on p. 104).

[337] C. Degrande et al. 'Effective Field Theory: A Modern Approach to Anomalous Couplings'. *Annals Phys.* 335 (May 2013), pp. 21–32. DOI: 10.1016/j.aop.2013.04.016. arXiv: 1205.4231 (cit. on p. 107).

[338] N. Arkani-Hamed et al. 'Physics Opportunities of a 100 TeV Proton-Proton Collider' (2015). arXiv: 1511.06495 [hep-ph] (cit. on p. 108).

[339] P. Torrielli. 'Rare Standard Model processes for present and future hadronic colliders' (2014). arXiv: 1407.1623 [hep-ph] (cit. on p. 109).

[340]   J. Frank. 'Spin-2 Resonances in Vector Boson Fusion Processes at the LHC'. Diploma-Thesis. Karlsruhe Institute of Technology, 2011. 115 pp. `http://www.itp.kit.edu/prep/diploma/PSFiles/Diplom_Frank.pdf` (cit. on p. 110).

[341]   S. Fartoukh, F. Zimmermann. 'The HL-LHC accelerator physics challenges'. *Adv. Ser. Dir. High Energy Phys.* 24 (2015), pp. 45–96. `https://cds.cern.ch/record/2132265` (cit. on p. 116).

Acknowledgement

I would like to extend my thanks to Rosita Jurgeleit, Monika Goldhammer and Annette Sturm, the (former and current) secretaries of the theory section, for their support and friendly help.

Special acknowledgements also to the computing support of the MPP, greatly maintained by Thomas Hahn, also a member of my PhD advisory panel, and for the computing support by the Rechenzentrum Garching (MPCDF).

I would like to express my cordial thanks to PD Dr. John Davis, who helped me to improve the English of this thesis.

Last but not least, I am indebted to my whole family, especially to Sophia Maria, my wife, for the endless support, encouragement and advice.